Petrogenesis of the peralkaline ignimbrites of Terceira, Azores

A. J. Jeffery[a*], R. Gertisser[a], S. Self[b] , A. Pimentel[c, d], B O'Driscoll[e], J. M. Pacheco[d]

a) *School of Geography, Geology and the Environment, Keele University, Keele, Staffordshire, ST5 5BG, United Kingdom*

b) *Department of Earth and Planetary Science, University of California, Berkeley, CA 94720, U.S.A.*

c) *Centro de Informação e Vigilância Sismovulcânica dos Açores, 9501-801 Ponta Delgada, Azores, Portugal*

d) *Instituto de Investigação em Vulcanologia e Avaliação de Riscos, University of the Azores, 9501-801 Ponta Delgada, Portugal*

e) *School of Earth, Atmospheric, and Environmental Sciences, The University of Manchester, Manchester, M13 9PL, United Kingdom*

* Corresponding author

Address: *School of Geography, Geology and the Environment, Keele University, Keele, Staffordshire, ST5 5BG, United Kingdom*

Tel: *+44 (0) 1782 733620*

e-mail: *a.j.jeffery@keele.ac.uk*

ABSTRACT

The recent (< 100 ka) volcanic stratigraphy of Terceira, Azores, includes at least seven peralkaline trachytic ignimbrite formations, attesting to a history of explosive eruptions. In this study, the petrogenesis and pre-eruptive storage conditions of the ignimbrite-forming magmas are investigated via whole-rock major and trace element geochemistry, melt inclusion and groundmass glass major element and volatile compositions, mineral chemistry, thermobarometrical models, and petrogenetic modelling. Our primary aims are to develop a model for the magmatic plumbing system from which the ignimbrite-forming trachytes of Terceira were produced by evaluating various petrogenetic processes and constraining pre-eruptive magma storage conditions. We also place the ignimbrite-forming magmas into the context of the Terceira suite and discuss the potential implications of pre-eruptive magma conditions for eruptive behaviour. Results indicate that ignimbrite-forming, comenditic trachytes are generated predominantly by extended fractional crystallisation of basaltic parental magmas at redox conditions around 1 log unit below the fayalite-magnetite-quartz buffer. This is achieved via a polybaric fractionation pathway, in which mantle-derived basalts stall and fractionate to hawaiitic compositions at lower crustal depths (~ 15 km), before ascending to a shallow crustal magma storage zone (~ 2 to 4 km) and fractionating towards comenditic trachytic compositions. The most evolved pantelleritic magmas of Terceira (not represented by the ignimbrites) are plausibly generated by continued fractionation from the comenditic trachytes. Syenite autoliths represent portions of peralkaline trachytic melt which crystallised *in situ* at the margins of a silicic reservoir. Trachytic enclaves hosted within syenitic autoliths provide direct evidence for a two-stage mingling process, in which ascending hawaiites are mixed with

trachytic magmas in the shallow crustal magma storage zone. The resulting hybridised trachytes then ascend further and mix with the more evolved peralkaline trachytes in the uppermost cap of the system, passing first through a syenitic crystal mush. The reduced viscosities of the peralkaline silicic magmas of this study in comparison to their metaluminous counterparts facilitate rapid crystal-melt segregation via crystal settling, generating compositionally zoned magma bodies and, in some instances, relatively crystal-poor erupted magmas. Reduced viscosity may also inhibit highly explosive activity (e.g. formation of a sustained eruption column), and limit the majority of explosive eruptions to low pyroclastic fountaining or 'boil-over' eruption styles. The formation of intermediate composition magmas within the system is considered to be limited to episodic mixing between mafic and silicic magmas.

Keywords: Terceira, ignimbrite, peralkaline, fractional crystallisation, zoned magma reservoir, magma mingling, thermobarometry, Daly Gap

INTRODUCTION

Terceira, one of the nine islands of the Azores archipelago, exhibits a number of petrological features which are atypical of oceanic island silicic centres. In contrast with the frequently alkali basalt-dominated volcanism of oceanic islands, a significant proportion (86 vol. %; Self, 1976) of recently (< 20-23 ka) erupted products on Terceira have been silicic and peralkaline, extending to pantelleritic compositions. Furthermore, in addition to abundant silicic lava domes and coulées, the volcanic stratigraphy of Terceira includes at least seven ignimbrite-bearing pyroclastic

formations, some of which exhibit variably welded units, basal pumice falls, and dilute pyroclastic density current (surge) deposits (Gertisser *et al*., 2010), attesting to a spasmodic history of explosive eruptions of silicic magmas (Self, 1974, 1976; Gertisser *et al*., 2010). Although ignimbrite-forming eruptions have occurred on other Azorean islands, such as Faial (Pacheco, 2001; Pimentel *et al*., 2015), São Miguel (Duncan *et al*., 1999; Gaspar *et al*., 2015), and Graciosa (Gaspar, 1996), they represent a relatively minor portion of each island's eruptive history. Such phenomena have also been reported at different locations in contrasting geodynamic settings worldwide (e.g. Pantelleria, Mahood & Hildreth, 1986; Gran Canaria, Araña *et al*., 1973; Ascension, Daly, 1925; Socorro, Bryan, 1966).

Studies of peralkaline magmatic systems have highlighted their complexity, revealing the interplay of petrogenetic processes such as fractional crystallisation, crustal assimilation, magma mixing, and remobilisation and, or, partial melting of cumulate material (e.g. Roux & Varet, 1975; Harris, 1983; Mahood, 1984; Davies & Macdonald, 1987; Macdonald, 1987; McBirney, 1993; Mungall & Martin, 1995; Black *et al*., 1997; Bohrson & Reid, 1997; Scaillet & Macdonald, 2001; Macdonald & Scaillet, 2006; Ren *et al*., 2006; White *et al.*, 2006; Macdonald *et al*., 2008; White *et al*., 2009; Markl *et al*., 2010; Hong *et al*., 2013; Shao *et al*., 2015; Jeffery *et al*., 2016a). Considering the further complexity introduced by P-T-fO_2 conditions and compositional variability, such systems are individually unique, to some extent (Macdonald, 2012). However, many peralkaline complexes are, in some respects, unified by the frequent occurrence of compositional zonation of their magma reservoirs (e.g. Civetta *et al*., 1984; Mahood 1984; Mahood & Hildreth, 1986; Macdonald *et al*., 1994; Troll & Schmincke, 2002; Peccerillo *et al*., 2003; Sumner & Wolff, 2003; Macdonald, 2012). Mungall & Martin (1995) proposed that the most

recently extruded (< 20-23 ka) peralkaline silicic magmas on Terceira could be generated via extended fractional crystallisation of an alkali basalt parental magma composition.

In this study, we apply whole-rock major and trace element geochemistry, melt inclusion and groundmass glass major and volatile element analyses, mineral chemistry, thermobarometry, and petrogenetic modelling to the ignimbrites of Terceira, erupted between ~ 86 and ~ 20-23 ka (Gertisser *et al*., 2010), and a suite of associated syenite autoliths, aiming to: (1) elucidate the petrogenesis of the peralkaline, ignimbrite-forming silicic magmas of Terceira; (2) constrain the pre-eruptive magma storage conditions; (3) place the ignimbrite-forming magmas of Terceira within the context of the identified magma series of Mungall & Martin (1995), as well as the overall magmatic trend of the island; (4) evaluate the effects of the pre-eruptive magma system on eruption dynamics.

GEOLOGICAL BACKGROUND

The Azores archipelago comprises nine islands in the North Atlantic Ocean (Lat. 37°N to 40°N, Long. 25°W to 32°W), ~ 1,300 km west of the Portuguese mainland. The islands themselves are divided into three geographic groups (western, central and eastern), and represent the subaerial expression of the Azores Plateau, a triangular-shaped bathymetric and gravity anomaly reflecting a morphologically complex area (~ 5.8×10^6 km^2) of elevated oceanic crust that formed between 20 and 7 Ma (Kaula, 1970; Searle, 1980; Lourenço *et al*., 1998 Gente *et al*., 2003). The unique geodynamic setting of the Azores results from the triple junction of the North American, Eurasian and African lithospheric plates. This area of the North Atlantic, is marked by three

major tectonic features; the Mid-Atlantic Ridge (MAR), the East Azores Fracture Zone (EAFZ) and the Terceira Rift (e.g. Krause & Watkins, 1970; Ridley *et al*., 1974; Vogt & Jung, 2004; Luis & Miranda, 2008; Madeira *et al*., 2015). The MAR delimits the Eurasian and African plates to the east from the North American plate to the west. The EAFZ, located to the south of the archipelago, corresponds to an abandoned fault system that probably represents the ancient boundary between the Eurasian and African plates, which extends eastward as the Azores-Gibraltar Fracture Zone (Ridley *et al*., 1974; Luis *et al.*, 1994; Silveira *et al*., 2006; Madeira *et al*., 2015). The Terceira Rift runs for ~ 600 km in an oblique direction between the MAR in the NW and the EAFZ in the SE. The rift corresponds to the westernmost segment of Eurasian-African plate boundary and is characterized by a complex alignment of alternating basins and volcanic edifices, including seamounts and the islands of Graciosa, Terceira, and São Miguel. It is considered one of the world's slowest spreading-centres, with a spreading rate of 2 to 4 mm/a (Ridley *et al*., 1974; Searle, 1980; Madeira & Brum da Silveira, 2003; Vogt & Jung, 2004; Fernandes *et al.*, 2006; Madeira *et al*., 2015). All of the Azorean islands are volcanic in origin and magmatism in the area is widely believed to result from the complex interaction between the MAR and a melting anomaly, often referred to as the Azores mantle plume, though the precise nature of the anomaly remains a matter of some debate (e.g. Schilling, 1991; Widom & Shirey, 1996; Courtillot *et al*., 2003; Beier *et al*., 2012; Métrich *et al*., 2014).

Terceira Island belongs to the central group of the Azores and is the third largest in the archipelago, with an area of approximately 400 km^2 (Fig. 1). The island comprises four central volcanoes (Cinco Picos, Guilherme Moniz, Pico Alto and Santa Bárbara) that sit astride a 2 km wide basaltic fissure zone that bisects the island from NW to SE (Self, 1974, 1976). The oldest volcanic centre, Cinco Picos (also

known as Serra do Cume-Ribeirinha; e.g. Pimentel *et al.*, 2016) (> 401 ka; Hildenbrand *et al.*, 2014), comprises a heavily eroded, 9 × 7 km caldera that dominates the SE sector of the island, with volcanism showing a compositional range that extends from basalt to peralkaline trachyte (Self, 1974; Self & Gunn, 1976). Guilherme Moniz volcano (> 270 ka in age; Calvert *et al*., 2006) is located slightly south of the centre of the island and, like Cinco Picos, comprises a 4 × 2 km caldera, with basaltic rocks in its floor and peralkaline trachytic rocks exposed in the caldera walls (e.g. Self, 1974; Self & Gunn, 1976).

Pico Alto (for which the oldest available age is 141 ka; see Gertisser *et al*., 2010) lies on the northern flank of Guilherme Moniz, and is considered by Calvert *et al*. (2006) to represent the younger portion of the same volcanic centre. Unlike the other volcanic centres, Pico Alto lacks a well-defined morphological structure, and comprises an assemblage of comenditic and pantelleritic lava domes and coulées partially filling and overflowing a caldera (Self, 1974; Pimentel, 2006; Gertisser *et al*., 2010). The eruptive history of Pico Alto shows evidence of explosive eruptions, recorded by major pyroclastic formations dominated by ignimbrites, erupted between ~ 86 and ~ 20-23 ka (Gertisser *et al*., 2010).

The youngest volcano, Santa Bárbara (> 65 ka; Hildenbrand *et al*., 2014), takes a distinctive conical shape, rising up to 1,021 m above sea level, truncated by two small nested calderas. Compositionally, this landform is made up of recent (< 20-23 ka) peralkaline silicic lava domes and coulées, and pumice falls, which overly mafic rocks including hawaiites and mugearites (Self, 1974, 1976; Self & Gunn, 1976).

The fissure zone (> 43 ka; Calvert *et al*., 2006) that bisects the island is defined by alignments of scoria cones, spatter cones, lava flows, and collapse pits (Self, 1976;

Mungall & Martin, 1995; Zanon & Pimentel, 2015). It shows a general progression towards younger ages from SE to NW, and traverses the extinct volcanic centres, Guilherme Moniz and Cinco Picos, covering the floor of both calderas with young basalts and hawaiitites. Three historical eruptions occurred along the fissure zone, in the centre of the island as well as off-shore (Zbyszewski, 1966; Gaspar *et al*., 2003; Pimentel *et al*., 2016). The fissure zone is considered to represent the surface expression of the Terceira Rift (Self, 1974).

IGNIMBRITE STRATIGRAPHY

Ignimbrite-forming eruptions on Terceira appear to have been limited to periodic, short-lived eruptive episodes that each led to multiple depositional units. These are interspersed with longer periods of quiescence or eruption of various pyroclastic deposits and lava flows. The stratigraphy and chronology of ignimbrites on Terceira was established by Gertisser *et al*. (2010) (Fig. 2), who identified seven distinct pyroclastic formations containing ignimbrites or composed of ignimbrites based upon field characteristics, stratigraphical relationships, ^{14}C and $^{40}Ar/^{39}Ar$ chronology, as well as major and trace element geochemistry. Each formation is bounded by unconformities and records an eruptive event or, more often, a sequence of eruptions closely spaced in time, and was named following the original scheme of Self (1974; 1976), where possible. The most likely source of the ignimbrites was identified by Gertisser *et al*. (2010) to be Pico Alto, and possibly Guilherme Moniz in the case of the older ignimbrite formations. The same authors also identified two further pyroclastic density current deposits (the Quatro Ribeiras pyroclastic flow deposit and

the Posto Santo spatter flow deposit), which are not considered further in this study due to their comparatively isolated occurrence.

The stratigraphy of the island has been studied in depth by Self (1974; 1976) and Gertisser *et al*., (2010), with a number of ages reported by the latter. The stratigraphy is divided into the Upper Terceira Group (UTG) and the Lower Terceira Group (LTG), each comprising basaltic to trachytic and rhyolitic lava flows, pumice and scoria falls, and ignimbrites (Fig. 2). The base of the UTG is marked by the youngest and most extensive pyroclastic formation, the Lajes-Angra Ignimbrite Formation (LAI). At least 116 separate eruptions of Santa Bárbara and Pico Alto, alongside fissure zone activity, are recorded by pumice falls, scoria falls and lava flows, lava domes and coulées of the UTG, overlying the LAI. The LAI itself comprises two distinct members; the Angra Ignimbrite (exposed on the southern coast) and the Lajes Ignimbrite (exposed on both the northern and southern coasts), and is dated between 20 and 23 ka (Gertisser *et al.*, 2010). The Lajes member (20,110 ±470 to 23,150 ±730 uncalibrated ^{14}C years BP) is a relatively thin ignimbrite (3.5 m on average) with a welded lower part and a non-welded upper ignimbrite unit, whilst the Angra member (21,220 ±120 to 22,310 ±800 uncalibrated ^{14}C years BP) is a thicker (up to 14 m) and remarkably monotonous, almost totally non-welded ignimbrite.

Stratigraphically below the LAI, interstratified pumice falls, lava flows and at least six other ignimbrite formations and two other pyroclastic density current deposits combine to form the Lower Terceira Group (LTG) (Gertisser *et al*., 2010). These include the Linhares-Matela Ignimbrite Formation (LMI), the Vila Nova-Fanal Ignimbrite Formation (VFI), the Calderia-Castelinho Ignimbrite Formation (CCI), the Pedras Negras Ignimbrite Formation (PNI), the Grota do Vale Ignimbrite Formation

(GVI) and the Ignimbrite-i Formation (Ign-i). The LMI is the uppermost ignimbrite formation in the LTG, comprising the Linhares and Matela members which appear to be limited to the south of the island. The LMI is separated from the overlying LAI by a lava flow and approximately 10 m of pyroclastic fall deposits, and is ^{14}C dated at 34,690 ±7500 to 37,320 ±4960 uncalibrated years BP (Gertisser *et al.*, 2010).

The VFI is made up of multiple pyroclastic density current units and associated pumice fall units, and is divided into two members; the Vila Nova member, exposed in the northern coast, and the Fanal member, exposed in the southern coast. They are $^{40}Ar/^{39}Ar$ dated at 50 ±10 ka and 58 ±20 ka, respectively (Gertisser *et al*., 2010). The CCI also comprises two members; the Caldeira member in the north and the Castelinho member in the south, both of which are stratigraphically below the VFI. Of all the ignimbrites on Terceira, it is the only one to exhibit a well-developed fall unit and overlying dilute pyroclastic density current deposit, featuring cross bedding of both fine- and coarse-grained pumice beds. Although small fine-grained syenitic clasts may be found in at least one of the other ignimbrite formations (LAI), the CCI is characterised by abundant coarse-grained, syenitic autoliths (termed cognate xenoliths by Gertisser *et al.,* 2010), which can reach sizes of 25 cm in diameter. Gertisser *et al*. (2010) provided two $^{40}Ar/^{39}Ar$ ages of 71 ±4 ka and 83 ±18 ka for the CCI, showing that the CCI is considerably older than the overlying VFI.

The PNI is found stratigraphically below the CCI and exposed exclusively on the northern coast, typically as dark-weathering, heavily-eroded remnants with a welded basal layer. Ignimbrite-i is found only as a small outcrop on the north coast, where it is welded and positioned stratigraphically below the CCI. Gertisser *et al*. (2010) reported a single $^{40}Ar/^{39}Ar$ age of 86 ±9 ka for Ignimbrite-i, although its relationship to the PNI, exposed further westward along the northern coast, remains

unclear. The GVI (Gertisser *et al*., 2010) is the lowest ignimbrite on the south coast and, due to the unusual occurrence of biotite, does not correlate with either of the lowest ignimbrite formations outcropping along the north coast (PNI and Ign-i). The exposure is only ~1.5 m thick, but the top is eroded, so the original thickness is unknown.

PETROGRAPHY

Ignimbrites

Juvenile clasts sampled from the ignimbrites of Terceira range from pumice to dense vitrophyres and exhibit similar mineral assemblages, characterised by the presence of alkali feldspar (anorthoclase), augite, Ti-magnetite, and apatite ± olivine and ilmenite (Self, 1974; Gertisser *et al*., 2010). The GVI is a notable exception to this, in that it also contains phenocrysts of biotite, a mineral that is not observed in any of the other ignimbrite formations (Gertisser *et al.,* 2010). Additionally, the LMI is distinguished by the occurrence of plagioclase phenocrysts in addition to alkali feldspar.

In all of the ignimbrites anorthoclase is the dominant phase, although it typically does not exceed ~ 10 vol. % on a vesicle-free basis. Anorthoclase phenocrysts are generally unzoned, tabular, and up to ~ 4 mm in length (Fig. 3a). However, crystal fragments and heavily resorbed and embayed examples are also common, the latter being especially abundant in the LMI (Fig. 3b). Augite is generally restricted to subhedral microphenocrysts up to 0.2 mm in length, though comparatively large, euhedral phenocrysts (up to ~ 3 mm) are occasionally found (Fig. 3c). Augite frequently displays a spatial association with Fe-Ti oxides; the latter are often partially or entirely included within augite crystals (Fig. 3d). Olivine is

generally found as equant phenocrysts that do not exceed 2 mm and are frequently resorbed and embayed (Fig. 3e). Biotite in the GVI occurs as small, euhedral phenocrysts that generally do not exceed ~ 1 mm, and often contain inclusions of apatite (Fig. 3f). Ti-magnetite and ilmenite exhibit equant, subhedral forms that rarely exceed 1 mm in size. Some examples display optically visible zonation patterns in reflected light, with prominent, irregular cores, and rims of highly variable thickness and brighter reflectance (Fig. 3g). Rare examples of Ti-magnetite exhibit regular exsolution lamellae of ilmenite. Apatite is present in trace amounts throughout, and is generally restricted to small, acicular inclusions within other phases.

Syenitic autoliths

The quartz-syenitic autoliths of the CCI exhibit a variety of macroscopic textures, including inter- and intra-autolith grain size variations (Fig. 4a), schlieren structures rich in mafic minerals (Fig. 4b), and contain fine-grained, trachytic enclaves, with rounded, lobate forms and chilled margins (Fig. 4c). Individual autoliths can contain up to ~ 10 vol. % unfilled intercumulus void space in the freshest samples. Schlieren may anastomose or bifurcate, and are characterised by an abundance of Na-clinopyroxene, Na-amphibole, and aenigmatite, which may be either intercumulus or megacrystic (up to ~ 1 cm). Schlieren typically form at the contacts between two texturally or mineralogically distinct varieties of syenite (Fig. 4b).

The autoliths are characterised by more complex mineral assemblages than those of the various Terceira ignimbrite formations, comprising alkali feldspar (anorthoclase, sanidine, albite), Na-clinopyroxene, Na-amphibole, aenigmatite, Ti-magnetite, ilmenite, quartz, olivine, apatite, and biotite, in approximate decreasing

order of abundance, with dalyite and eudialyte representing the most significant zirconosilicate accessory phases (Jeffery *et al*., 2016b). This mineral assemblage contains phases that are typical of both miaskitic and agpaitic rocks (cf. Marks *et al*., 2011), suggesting that the syenites should be considered transitional between the two. Alkali feldspar is the most abundant phase, constituting ~ 75 vol. % of each autolith (including void space), and forming a cumulus framework, regardless of grain size. Individual crystals range from large, tabular crystals (up to ~ 10 mm, Fig. 5a) to smaller laths (up to ~ 2 mm, Fig. 5b), and from fresh and unaltered, to heavily altered and perthitic. Alkali feldspar is also present as small, irregular crystals which, together with quartz, form granophyric patches.

Na-clinopyroxene, Na-amphibole, and aenigmatite represent the dominant intercumulus phases, with a cumulative volume of up to ~ 10 vol. %. All three phases are concentrated in schlieren, where their abundance may be as high as ~ 50 vol. %, but are also present in subordinate quantities throughout the syenite. Within schlieren structures, Na-clinopyroxene is present as patches of acicular crystals that partially replace large aenigmatite crystals, of which only relict crystals with ragged edges remain. This relationship between Na-clinopyroxene and aenigmatite is not limited to schlieren structures and may be found throughout the syenite autoliths.

Outside of the previously described schlieren, Na-clinopyroxene exists as intercumulus crystals that can reach sizes of up to ~ 3 mm, and often exhibits irregular or patchy zonation (Fig. 5c). Furthermore, Na-clinopyroxenes frequently show a spatial association with Na-amphiboles, appearing to have nucleated heterogeneously on, or to have replaced, pre-existing amphibole crystals (Figs 5c, d). Similarly, amphiboles reach sizes of ~ 4 mm and are frequently zoned, with a brownish amphibole generally making up the central portion of a given crystal, and blue

amphibole forming the crystal margins (Fig. 5d). The margins between individual zones are almost exclusively irregular and gradational. Na-clinopyroxene is also present as small acicular crystals which form radiating bundles, typically projecting into unfilled cavities.

Quartz is also limited to intercumulus pore spaces, where it occurs as aggregates of rounded crystals up to ~ 1 mm in size. Together with phases such as acicular Na-clinopyroxene, dalyite, or eudialyte, quartz aggregates may either partially or entirely fill pores. Fe-Ti oxides are present as small (< 100 μm) equant crystals that are frequently included within other phases and do not account for more than 1 vol. % of the rock. More rarely, Fe-Ti oxides reach sizes of up to ~ 400 μm and may represent an intercumulus phase rather than an inclusion.

Olivine is uncommon in the syenites and, when present, exists as anhedral relict crystals which exhibit a complex reaction texture. Reaction rims are typically characterised by an inner, anhydrous zone including Fe-Ti oxides and an outer hydrous rim of iddingsite and comparatively rare biotite.

Apatite is present in trace amounts, and is limited to small (< 100 μm) acicular inclusions within other phases. Biotite is uncommon and, where present, exists as small inclusions within alkali feldspars. Eudialyte is found as irregularly-shaped crystals (generally < 1 mm) which partially or entirely fill intercumulus spaces, and is frequently associated spatially with Na-clinopyroxene. Examples of irregular, patchy or oscillatory zoning are common. Dalyite is typically present as small (< 0.5 mm) sub- to anhedral crystals, though it can reach sizes of 1 to 1.5 mm. It is almost exclusively anhedral and confined to the interstices, either filling or partially filling

void spaces. It is often associated spatially with quartz, and in some cases can be found as inclusions within larger interstitial quartz crystals (Jeffery *et al*., 2016b).

Syenite-hosted enclaves

Dark enclaves found within individual syenite autoliths from the CCI are porphyritic, with large plagioclase, alkali feldspar, diopside, augite, and Mg-rich olivine phenocrysts up to ~ 8 mm in length set in a fine-grained (< 0.2 mm) microcrystalline groundmass (Fig. 5f). Groundmass mineral assemblages include alkali feldspar (anorthoclase and albite), amphibole, diopside to aegirine-augite, Fe-Ti oxides, apatite, eudialyte, dalyite, aenigmatite and titanite, in approximate order of decreasing abundance. As in all of the rocks in this study, alkali feldspar is the dominant phase, occurring as large phenocrysts and as small (< 0.2 mm), anhedral groundmass crystals. Phenocrystic alkali feldspar is characterised by rounded cores, which are mantled by sieve-textured rims of variable width (~ 50 to 750 μm) (Fig. 5g). In contrast to the interior (core-rim) boundary, which is frequently sharp, the exterior boundary between rim and groundmass is frequently diffuse and poorly defined. Phenocryst cores often exhibit patchy or, more rarely, oscillatory zoning patterns.

Na-Ca amphibole is present both as a minor population of microphenocrysts, typically up to ~ 500 μm in length, and as an abundant groundmass phase (< 150 μm). Augite and Na-clinopyroxene are found in abundance in the groundmass, but also exist as phenocrysts and microphenocrysts (~ 250 to 1000 μm) which frequently have thin (< 50 μm) rims of iddingsite and exhibit resorption textures. Larger examples may also have concentric, oscillatory zoning patterns. Fe-Ti oxides are present as small groundmass crystals that do not exceed 150 μm. Olivine is found exclusively as ragged phenocrysts up to ~ 3 mm in size, and surrounded by a distinctive double rim (Fig. 5h). Apatite is limited to small (< 100 μm), acicular crystals in the groundmass

and included within other mineral phases. Eudialyte and dalyite are both present in trace amounts and are limited to miarolitic cavities, where they range from anhedral to euhedral morphologies, and reach sizes of up to ~ 500 μm. Unlike in the host syenites, aenigmatite is rarely found in the enclaves and is restricted to miarolitic cavities, where it is predominantly occurs as small, irregular patches within clusters of acicular clinopyroxene. Plagioclase is uncommon, and can be found as crystals up to ~ 8 mm in size.

ANALYTICAL METHODS

Whole-rock geochemistry

Whole-rock major and trace element analyses were obtained at the Bureau Veritas Mineral Laboratories, Canada, using inductively coupled plasma atomic emission spectroscopy (ICP-AES) and inductively coupled plasma mass spectrometry ICP-MS, respectively. Additional analyses were made using a Bruker AXS S4 Pioneer X-ray fluoresence spectrometer (XRF) at the University of East Anglia, U.K. All samples were cleaned to remove altered surfaces and crushed in an agate mill prior to drying at 60 °C. LOI was reported as weight difference after ignition for two hours at 1,000 °C.

Samples analysed by ICP-AES and ICP-MS at Bureau Veritas Mineral Laboratories, Canada, were prepared with a $LiBO_2/Li_2B_4O_7$ flux and dilute nitric digestion. The instrument was calibrated using up to twelve international standards (AGV-1, BCR-2, BHVO-1, BHVO-2, BIR-1, RGM-1, WS-E, JB2, JB3, SO-18, DS9, OREAS45EA). The mean deviation from the accepted standard values was < 2 % for major elements and < 3 % for trace elements (Supplementary Data Appendix 3).

For XRF analyses, fused glass discs for major element analysis were prepared using 0.7 g of rock powder mixed with 3.5 g of lithium metaborate. Trace element concentrations were determined using PVC bound pressed powder pellets. For major elements, the instrument was calibrated using the following international standards: BCR-2, DTS-1, DTS-2, G2, GXR-1, GXR-2, GXR-3, BHVO-2, BCS-368, BCS-376, AC-E, BE-N, BX-N, GS-N, UB-N, LKSD-3, MRG-1, STSD-1,SARM-2. For trace elements, the Geoquant calibration of Bruker was applied. Data quality was evaluated using the following secondary standards: WS-E, OUG94, GSP-2, W2a, AC-E, BHVO-1, QLO-1, DNC-1, W-2, AGV-2, BCR-2, SDO-1, Mess-2, STSD-2. The mean deviation from the accepted standard values was < 5 % for major elements, and typically < 10 % for trace elements.

Mineral and glass analyses

Major element compositions of mineral phases and glass (both groundmass glass and melt inclusions) were analysed using a CAMECA SX 100 electron microprobe at The Open University, U.K., a JEOL JXA 8900 RL electron microprobe at the University of Göttingen, Germany, and a CAMECA SX 100 electron microprobe at the University of Manchester. For mineral phases, peak counting times per element were 10 to 30 seconds using a 5 to 10 μm defocused beam, an acceleration voltage of 20 kV and a beam current of 20–27 nA. Major elements and volatiles (Cl, F, S) in groundmass glass and melt inclusions were analysed using peak counting times ranging from 90 to 120 seconds for volatiles and 10 to 30 seconds for major elements, using a 10 to 20 μm defocused beam, an acceleration voltage of 15 to 20 kV, and a beam current of 10 to 15 nA. To minimise Na loss, Na was always analysed first, with a peak count time of 10 seconds. Detection limits for Cl and F were 60 and 220 ppm,

respectively. Detection limits for S were 300 ppm. The following natural minerals and synthetic materials (denoted as chemical formulae) were used as primary standards: olivine, albite, sanidine, TiO_2, haematite, anorthite, wollastonite, Cr_2O_3, rhodonite, celsian, $ZrSiO_4$ and $HfSiO_4$. Mineral and volcanic glass standards (BCR-2G, VG-2, KN-18 and KE-12) were routinely analysed as secondary standards. Repeat analyses of secondary standards indicate accuracy of < 4 %, and reproducibility of < 3 % (mean standard deviation). Additionally, EDS spectra were produced using a Hitachi TM-3000 scanning electron microscope (SEM) equipped with a Bruker Quantax 70 energy dispersive system (EDS) at Keele University, U.K.

Fourier transform infrared spectroscopy

The water content of alkali feldspar-hosted melt inclusions was determined using spectra collected with a Thermo Nicolet Nexus FTIR spectrometer coupled with a Continuμm IR microscope at The Open University, U.K. Operation conditions included standard EverGlo mid-infrared source optics, a Ge-on-KBr beamsplitter, and a liquid nitrogen-cooled MCT-A* detector (11,700 – 750 cm-1). In all of the analyses, CO_2 was below the detection limit (~ 100 ppm, cf. Gertisser *et al*., 2012). The concentration of dissolved water was determined using the height of the total water ($H_2O + OH^-$) peak at 3550 cm^{-1} and the Beer-Lambert law:

$$H_2O\ (wt\ \%) = 100 \times \left(\frac{MA}{\rho d \varepsilon}\right)$$

where M is the molecular weight of H_2O (18.02), A is the height of the absorption peak, ρ is the sample density (gL^{-1}), d is the thickness of the sample (cm), and ε is the

molar absorption coefficient (l $mol^{-1}cm^{-1}$). The thickness of each sample (± 3 μm) was determined using a Mitutoyo Digimatic Indicator. The density of the trachytic glass at 298 K and 0.1 MPa was estimated to be 2510 g L^{-1}, assuming a nonlinear temperature dependence of melt volume (e.g. Gottsmann & Dingwell, 2002). Due to the variability of the molar absorption coefficient as a function of ((Si/Al)/total cations) in glass (e.g. Mandeville *et al*., 2002), the approach given by Seaman *et al*. (2009) was used to calculate a molar absorption coefficient value of 73 for the 3550 cm^{-1} peak.

RESULTS

The entire dataset discussed in the following section is provided in two electronic appendices. Whole-rock, melt inclusion, and groundmass glass data are provided in full in Supplementary Data Electronic Appendix 1, whilst mineral chemical data are given in Electronic Appendix 2. Details of applied data quality tests are given in Electronic Appendix 3. Furthermore, a summary providing the major petrographical and geochemical features of the identified lithologies of this study is given in Table 1. To provide context for the geochemical data of this study, a number of additional published datasets are used for comparison, including: (1) whole-rock analyses derived from each of the volcanic centres of Terceira (Pico Alto, Santa Bárbara, Guilherme Moniz, and Cinco Picos) as well as the fissure zone (Self, 1974; Mungall, 1993; Madureira *et al*., 2011); (2) glass analyses from distal tephras of the youngest ignimbrite formations (LAI, LMI, VFI, and CCI; Tomlinson *et al*., 2015); (3) a suite of monzonitic and syenitic xenoliths from Santa Bárbara and Pico Alto, respectively (termed here S. Bárbara xenoliths and P. Alto xenoliths; Mungall, 1993); (4) a small number of whole-rock analyses of enclaves found within trachytic lava flows from

Pico Alto (termed here P. Alto enclaves; Mungall, 1993); (5) glass analyses for interstitial glass found within syenitic xenoliths from Pico Alto lavas (referred to here as P. Alto xenolith glass; Mungall, 1993). Collectively, these data define the overall geochemical trend of Terceira and facilitate a discussion on the overall position of the ignimbrite-forming magas within the context of their volcanic centre (Pico Alto/Guilherme Moniz), and also the island as a whole (see below).

Whole-rock major element geochemistry

Based on the Total Alkali-Silica scheme of Le Bas *et al.* (1986), the whole-rock juvenile samples of the ignimbrite formations are classified as trachyte (Fig. 6a) and exhibit little variation, with SiO_2 contents clustering around 65 wt %, Al_2O_3 contents of ~ 15 wt %, total alkali contents of ~ 12 wt %, and uniformly low MgO (< 0.5 wt %) (cf. Gertisser *et al.*, 2010). The samples are almost exclusively peralkaline (P.I. > 1), with calculated peralkalinity indices (P.I. = mol. ($Na_2O + K_2O$ / Al_2O_3)) that range from 0.98 to 1.43. Syenite autoliths have similar whole-rock compositions to the ignimbrites, with calculated P.I. between 1.08 and 1.14 (Jeffery *et al.*, 2016b). Enclaves within syenitic autoliths exhibit slightly different whole-rock compositions, with lower SiO_2 and total alkali contents of 61 to 62 wt % and ~ 11 wt %, respectively. Additionally, the enclaves lie on the boundary between metaluminous and peralkaline compositions, with P.I. of 0.97 to 1.01. On the basis of the Al_2O_3 versus FeO_t classification scheme of Macdonald (1974), all peralkaline samples of this study are comenditic trachyte, with the exception of a basal pumice fall within the VFI, and a single anorthoclase-hosted melt inclusion from the CCI, which are classified as pantelleritic trachyte and pantellerite, respectively (Fig. 6c).

In Fig. 7, the major element compositions of this study, alongside available literature data for Terceira, are plotted *versus* MgO. For clarity, and due to the

association of the ignimbrite formations with Pico Alto and Guilherme Moniz, compositions from Santa Bárbara and Cinco Picos are not shown. Initially, SiO_2 shows a uniform concentration of ~ 47 wt % until ~ 4 wt % MgO, and then increases steadily to 72 wt % SiO_2. TiO_2 and FeO_t both exhibit a downward kink at ~ 6 wt % MgO. The alkalis (Na_2O and K_2O) both increase with decreasing MgO, exhibiting curved profiles. Interstitial glass from syenitic enclaves from Pico Alto lavas analysed by Mungall (1993) indicate late stage (< 1 wt % MgO) enrichment in Na_2O, reaching concentrations of up to ~ 12.5 wt %, though this is likely to reflect evolution of intercumulus melt pockets in a manner analogous to post-entrapment crystallisation in melt inclusions In contrast, CaO exhibits a gently curved, concave-downwards trend. Al_2O_3 contents increase slowly until ~ 1 wt % MgO, at which point concentrations fall from ~ 18 to ~ 5 wt %. MnO shows uniform concentrations of ~ 0.2 wt. % until, at ~ 1 wt % MgO, concentrations increase to ~ 0.8 wt %. P.I. increases gradually until ~1 wt % MgO, when it sharply increases to values of up to 5, if intercumulus glasses are included.

Whole-rock trace element geochemistry

Selected trace elements are plotted against MgO in Fig. 7, together with previously published data (Self, 1974; Mungall, 1993; Madureira *et al.*, 2011). Overall, trace elements such as Zr, Nb, Rb, and Y behave incompatibly in the mafic and intermediate compositions (> 1 wt % MgO), with a steepening trend at trachytic compositions (< 1 wt % MgO). In contrast, Sr concentrations increase from ~ 500 to ~ 700 ppm in the mafic and intermediate portion of the trend, whilst the silicic portion of the trend is generally restricted to values below ~ 150 ppm. Unlike Sr, Ba shows no clear trend. Instead, considerable scatter is observed throughout the suite, with mafic

and intermediate compositions ranging from ~ 200 to 1000 ppm and silicic compositions ranging from < 20 to ~ 1550 ppm.

Chondrite-normalised REE patterns are shown in Figs 8a, b and indicate a relatively uniform enrichment of the LREE relative to the HREE, with a total range of La_N/Yb_N ratios between 8.3 and 12.4. All of the samples exhibit variable negative Eu anomalies, with Eu/Eu* = 0.31 to 0.83 in the ignimbrites, 0.41 to 0.52 in the syenites, and 0.76 to 0.86 in the enclaves. A single syenite sample deviates markedly from the other samples, with a significant depletion of MREE.

Primitive mantle-normalised multi-element diagrams are given in Figs 8c, d. The ignimbrites are characterised by pronounced depletions in Ba, Sr, Eu, P, and Ti. A notable exception to this observation is Ign-i, which exhibits a slight enrichment in Ba relative to the other ignimbrites. Syenitic autoliths and enclaves contained therein display a similar geochemical profile to those of the ignimbrites, with the same troughs for Ba, Sr, Eu, P, and Ti. However, in the syenites, these troughs are deeper than in the ignimbrites, and in the enclaves, they are shallower. As observed for Ign-i, the enclaves do not exhibit the same trough for Ba and instead indicate a slight enrichment.

Melt inclusions

Melt inclusions in the ignimbrites have broadly similar major element compositions to groundmass glass and whole-rock analyses (Figs 6, 7). All of the melt inclusions are classified as trachytic, with SiO_2 contents around 65 wt %, Al_2O_3 contents between 12 and 17 wt %, total alkali contents of ~ 12 wt %, and MgO below 0.5 wt %. The majority of samples are peralkaline (P.I. = 0.99 to 1.43). Chlorine concentrations show a total range of 1,510 to 6,960 ppm (average = 2,810, n = 114), and F contents

vary from 620 to 4,750 ppm (average = 1,644, *n* = 112). Sulphur concentrations are frequently below the detection limit (300 ppm). FTIR analyses of selected melt inclusions indicate water contents that range from 2.5 to 4.2 wt %, with an average of 3.5 wt %. In contrast, CO_2 was not detected in any of the inclusions and was therefore considered to be below the detection limit of FTIR spectroscopy (~ 100 ppm; cf. Gertisser *et al*., 2012).

Groundmass glass

Major element compositions of groundmass glass are similar to the whole-rock compositions, and are classified as trachyte (Fig. 6). SiO_2 contents cluster around 65 wt %, with Al_2O_3 contents of ~ 15 wt %, total alkali contents of ~ 12 wt % and MgO contents that rarely exceed 0.5 wt %. All of the groundmass glass analyses are peralkaline, with P.I. between 1.05 and 1.26, and are classified as comenditic trachyte. Volatile contents show significant variation; for example Cl concentrations show a total range of 1,460 to 3,370 ppm (average = 2,250 ppm, *n* = 23). Fluorine concentrations are similarly varied, ranging from < 220 to 2,610 ppm (average = 1,259 ppm, *n* = 21). In contrast, S concentrations are exclusively below detection (i.e. < 300 ppm).

Mineral chemistry

Mineral chemical data are provided for the major mineral phases found in the three lithologies of this study: feldspar, clinopyroxene, olivine, Fe-Ti oxides, biotite and amphibole.

Feldspar

Alkali feldspars in the ignimbrite formations generally range from oligoclase to sanidine in composition, with a range of Or_{10-39}, Ab_{60-81}, An_{0-11} (Fig. 9a). However, the LMI also contains some plagioclase feldspars, classified as oligoclase, andesine and labradorite (Or_{1-16}, Ab_{36-77}, An_{10-62}). Concentrations of BaO and SrO reach maxima of 1.25 and 0.19 wt %, respectively, with the highest concentrations generally being found in the least potassic feldspars. Feldspars within the syenite autoliths exhibit a similar range to the ignimbrites (Or_{17-40}, Ab_{60-83}, An_{0-4}), though the inclusion of perthitic feldspars extends this range towards the albite and orthoclase end-members. BaO and SrO concentrations are less than observed in the ignimbrites (up to 0.27 and 0.09 wt %, respectively). Groundmass feldspars in the syenite-hosted enclaves show a linear trend between anorthoclase and albite, with a compositional range of Or_{2-35}, Ab_{65-97}, An_{0-6}, and BaO and SrO contents of up to 0.38 and 0.05 wt %, respectively. In contrast, analyses of the large enclave feldspar crystals reveal a bimodal population, with the majority of analyses being classified as anorthoclase or sanidine (Or_{4-63}, Ab_{36-89}, An_{0-12}), and a smaller number of analyses indicating the presence of labradorite and bytownite (Or_{0-1}, Ab_{18-38}, An_{62-82}). The latter population contains SrO concentrations that are somewhat higher than those of the alkali feldspars (0.15 compared with 0.09 wt %).

Clinopyroxene

In the three-component (Wo-En-Fs) system of Morimoto *et al*. (1988) the clinopyroxene populations of the ignimbrites are dominantly classified as augite, with a compositional range of Wo_{39-46}, En_{21-41}, Fs_{16-36} (Fig. 9b). A small number of crystals from the PNI lie outside of this range, with Mg-rich compositions. In contrast, the syenite clinopyroxene is dominated by aegirine-augite to aegirine, with a total compositional range of Qd_{0-96}, Aeg_{4-99}, Jd_{0-7}. Groundmass clinopyroxene from the enclaves also reveal a trend from standard quadrilateral clinopyroxene to aegirine-augite, with a total compositional range of Qd_{43-97}, Aeg_{3-57}, Jd_{0-9}. The enclave phenocrysts exhibit a bimodal distribution of quadrilateral compositions; one comparable to the ignimbrite clinopyroxene (Wo_{42-43}, En_{31-35}, Fs_{22-26}), and another which is more Mg-rich (Wo_{44-48}, En_{40-46}, Fs_{8-15}). In the ternary Di-Hed-Aeg system (calculated using the 10 component scheme of Marks *et al*., 2008), all of the analyses define a single trend in which hedenbergite contents increase with little change in aegirine content until ~ Hed_{55}, at which point aegirine increases rapidly towards near end-member compositions.

Olivine

Olivine phenocrysts within the ignimbrites exhibit a compositional range from Fa_{59-82}. A single Mg-rich olivine was identified in Ign-i, with a contrasting composition of Fo_{75}. EDS spectra semi-quantitatively indicate that large olivine crystals in the syenite-hosted enclaves are Mg-rich in composition.

Fe-Ti oxides

Ti-magnetite is the most common Fe-Ti oxide present in the ignimbrites and exhibits a compositional range of Mt_{5-53}, Usp_{45-94}, Sp_{1-6}, with Al_2O_3 and MgO contents of up to 3.0 and 2.1 wt %, respectively (Fig. 9c). MnO contents are generally high, ranging

from 1.3 to 2.4 wt %. Ti-magnetite in the syenite autoliths shows a smaller compositional range of Mt_{32-57}, Usp_{35-68}, Sp_0, and significantly lower Al_2O_3 and MgO contents below 0.2 wt %. However, MnO concentrations are similarly high, reaching 2.45 wt %. Ilmenite is less common in the ignimbrites than Ti-magnetite, and exhibits a restricted compositional range of Ilm_{90-92}, Hem_{3-5}, Pyr_5. Al_2O_3 contents are exclusively below 0.1 wt % and MgO concentrations do not exceed 1.8 wt %. The Mn component is comparable to that of Ti-magnetite, with MnO contents up to 2.3 wt %. Ilmenite in the syenite autoliths also show a restricted range (Ilm_{90-94}, Hem_{1-4}, Pyr_{5-7}), low Al_2O_3 and MgO (< 0.1 and < 0.25 wt %, respectively), and high MnO contents (up to 3.6 wt %).

Biotite

Biotite phenocrysts found in the GVI are characterised by high TiO_2 contents (5.7 to 6.0 wt %), variable SiO_2 (36.6 to 39.3 wt %), Na_2O contents of up to 1.2 wt %, and Fe/Fe+Mg ratios of ~ 0.35 (Fig. 9d). The hydroxyl sites are characterised by variably high F contents (0.630 to 0.881 atoms per formula unit (apfu)) and low Cl contents (< 0.015 apfu)

Amphibole

Following the nomenclature of Leake *et al*. (1997), the amphiboles from the syenite autoliths belong to the sodic-calcic (Fig. 9e) and the sodic group (Fig. 9f), and are classified as katophorite to ferrorichterite, and ferroeckermannite and arfvedsonite, respectively. Fluorine concentrations range from 0.714 to 1.055 apfu, whereas Cl contents are exclusively < 0.015 apfu. Individual amphibole crystals are often zoned, with Na-Ca-amphibole in the core, and Na-amphibole rims. Amphiboles in the groundmass of syenite-hosted enclaves range from calcic to sodic-calcic, and can be classified as ferroedenite, and katophorite and ferrorichterite, respectively (Fig. 9 f, g).

Occupation of the hydroxyl site is characterised by a greater range than amphiboles from the syenites, with F ranging from 0.093 to 1.247 apfu, and Cl not exceeding 0.015 apfu.

DISCUSSION

In this section, the combined dataset presented above is used to provide insights into the pre-eruptive magmatic system which fed the ignimbrite-forming eruptions of Terceira. First, the pre-eruptive P-T-fO_2 conditions of the ignimbrite-forming magmas are explored, followed by a detailed examination of the relative roles of various petrogenetic processes. Second, a conceptual model is presented, considering the variability of magma rheology and chemical zonation, aiming to account for the petrological features observed within each of the ignimbrites. Third, the ignimbrites are considered within the context of the magmatic suite of Terceira. Finally, the pre-eruptive viscosity of the erupted magmas is considered in terms of its potential control on eruptive behaviour.

Pre-eruptive magma storage conditions

Temperature

Where both Ti-magnetite and ilmenite were present, pre-eruptive temperatures were calculated using the ILMAT program of Lepage (2003), applying the model of Andersen *et al*. (1993), and utilising the calculation scheme of Stormer (1983) to determine values for X_{hem}, X_{ilm}, X_{mag}, X_{ulv} (Supplementary Data Electronic Appendix 4). The application of alternative calculation schemes was shown to lead to variation of no more than 5 % in the calculated results. Equilibrium between mineral pairs was

evaluated using the Mn-Mg partitioning test of Bacon & Hirschmann (1988). Pre-eruptive magmatic temperatures were also estimated using the alkali feldspar-melt thermometer of Putirka (2008) (Supplementary Data Electronic Appendix 4). To minimize the error introduced by mineral-liquid disequilibrium, the Kd_{Ab-Or} equilibrium test proposed by Mollo *et al*. (2015) was applied, allowing a single suitable liquid composition to be selected for each case. Input pressure values were set at 0.1 GPa, and it was observed that a variation of 0.1 GPa led to a change in temperature of only 0.1 ºC, suggesting that the thermometer is not significantly influenced by pressure variations. The standard error of estimate (SEE) associated with the thermometer is ± 23 ºC. Due to the relative scarcity of ilmenite, estimates derived from two-oxide models were calculated only for the LAI juvenile clasts and the CCI syenite autoliths. Conversely, the abundance of alkali feldspar facilitated the calculation of magmatic temperatures for all of the ignimbrites and the syenite autoliths.

Two-oxide temperature estimates for the LAI range from 773 to 873 ºC (average = 830 ºC, *n* = 590, stdev = 21), whilst estimates for the syenite autoliths lie between 616 and 769 ºC (average = 687 ºC, *n* = 20, stdev = 40) (Fig. 10a). The alkali feldspar-melt temperatures for the LAI, VFI, CCI, PNI, and Ign-i lie between 857 to 912 ºC (average = 880 ºC, *n* = 304, stdev = 7) (Fig. 10b). Notably, the results for the LMI and the GVI deviate from this, with contrasting temperature ranges of 927 to 938 ºC (average = 932 ºC, *n* = 16, stdev = 3) and 819 to 824 ºC (average = 821 ºC, *n* = 42, stdev = 2), respectively. Temperature estimates for the CCI syenites are hotter than those predicted via two-oxide models, with a range of 864 to 880 ºC (average = 873 ºC, *n* = 31, stdev = 4). Alkali feldspar-based temperature estimates for the syenite-hosted enclaves range from 876 to 894 ºC (average = 884 ºC, *n* = 15, stdev = 6).

The temperatures determined via alkali feldspar-based models for the ignimbrite-forming magmas are notably greater than those derived from two-oxide models. Temperature estimates for the CCI syenites exhibit a similar disparity between models, with alkali feldspar thermometry producing a slightly higher range of temperatures. This may reflect the earlier crystallisation of the feldspars relative to the oxides, particularly in the syenite nodules. Alternatively, this may result from the rapid re-equilibration timescales of coexisting Fe-Ti oxides (e.g. Gardner *et al*., 1995; Venezky & Rutherford, 1999; Pimentel *et al*., 2015), meaning that the lower temperatures recorded by Fe-Ti oxide phases reflect the final pre-eruptive magma system and, or, syn-eruptive conditions within the plumbing system.

Oxygen fugacity

The pre-eruptive redox conditions of the magmatic system were determined via two-oxide models as described above (Supplementary Data Electronic Appendix 4). Estimates could only be determined for the LAI and the CCI syenites. Ti-magnetite and ilmenite pairs in the LAI indicate redox conditions close to 1 log unit below FMQ (Fig. 10a). The CCI syenites yield results that extend from 1 to 2 log units below FMQ.

Pre-eruptive volatile content

Pre-eruptive volatile contents were determined via FTIR and electron microprobe analysis of alkali feldspar-hosted melt inclusions and estimated via feldspar-melt hygrometry (Mollo *et al*., 2015). FTIR analyses of melt inclusions indicate H_2O contents that range from 2.5 to 4.2 wt % (average = 3.54 wt %; n = 8), and CO_2 contents below detection (< 100 ppm; cf. Gertisser *et al*., 2012). Similarly, pre-

eruptive concentrations of S are frequently below the detection limit (i.e. < 300 ppm), with only a small number of analyses from the CCI reaching concentrations of up to ~ 1,260 ppm. Melt inclusions from the LAI and VFI indicate average pre-eruptive concentrations of Cl and F of 2,550 ppm and 1,550 ppm, respectively. Melt inclusions from the CCI record higher and more variable volatile contents (average = ~ 3,550 ppm Cl and ~ 1,760 ppm F). Available melt inclusion analyses for the older ignimbrites suggest that the GVI and PNI are comparable to the CCI, whilst Ign-i exhibits the greatest degree of halogen enrichment, with ~ 6,960 ppm Cl and 4,750 ppm F. Excluding samples from the VFI, the total dataset for Cl and F forms a linear trend which correlates positively with calculated peralkalinity indices, suggesting that their concentrations are controlled primarily by fractionation, and indicating volatile undersaturated conditions with respect to Cl and F (Fig. 11). Notably, available analyses for Ign-i indicate a positive correlation between F and peralkalinity index, whilst Cl appears to plateau at ~ 7,000 ppm. This may indicate the exsolution of a Cl-rich aqueous fluid and would suggest that the magma from which Ign-i was derived was stored at pressures below ~ 180 MPa (Metrich & Rutherford, 1992).

For hygrometry, temperature estimates derived from alkali feldspar-melt thermometry were used as primary inputs, alongside feldspar and potential equilibrium liquid compositions. The SEE associated with these results is ± 0.53 wt %. When outliers are included, alkali feldspar-melt models applied to the ignimbrites, the CCI syenites, and the syenite-hosted enclaves predict a slightly larger range of pre-eruptive water contents than determined via FTIR, with an overall average of 4.7 wt. % (3.0 to 5.9 wt. %; n = 396, stdev = 0.6) (Fig. 10b). Within this range, the GVI and LMI deviate from this average value. The GVI yields a restricted but somewhat higher range of 5.2 to 5.9 wt % (average = 5.7 wt %, n = 42, stdev = 0.1), whilst the

LMI exhibits a lower than average range of water contents of 3.0 to 3.7 wt. % (average = 3.4 wt %, n = 14, stdev = 0.2).

Pressure

The depth of the magma storage system was estimated quantitatively using the H_2O solubility model of Di Matteo *et al.* (2004). If the maximum water content, determined via FTIR (4.2 wt %) is applied, and water saturated conditions assumed, then the minimum pressure associated with the magmatic system which generated the ignimbrite-forming eruptions is ~ 80 MPa. This value increases to ~ 135 MPa, if the maximum estimate of water content derived from alkali feldspar hygrometry is applied (6.0 wt %). Assuming a crustal density of 2,800 kg/m^3, this equates to depths between 2.2 and 3.7 km.

The crustal depths at which the Terceira ignimbrite-forming magmas evolved can also be investigated using the clinopyroxene population. The rocks of this study all contain clinopyroxene, ranging compositionally from diopside, augite, and aegirine-augite in the enclaves to augite in the ignimbrites, and finally to aegirine-augite and aegirine in the syenites. Due to the Na-rich nature of the syenite clinopyroxene population, they were considered unsuitable for thermobarometry. Furthermore, thorough testing for equilibrium between crystals and melts (following Putirka, 2008 and Mollo *et al*., 2013; see Jeffery, 2016) indicates a general lack of equilibrium between clinopyroxene and any of the silicic rocks of this study, precluding the application of clinopyroxene-based thermobarometrical models. It is notable that, when applied to the clinopyroxene population of the ignimbrite-forming trachytes, the equilibrium test of Mollo *et al*. (2013) indicated a positive correlation between the abundance of Al and Na (and therefore the aegirine end-member) and the 'proximity' to equilibrium, suggesting that the diopside and augite phenocrysts of the

ignimbrites belong to a less evolved melt composition. The aegirine-rich compositions of clinopyroxene within the syenite nodules is therefore more likely to reflect a composition in equilibrium with a peralkaline melt, but remains unsuitable for thermobarometry due to its somewhat extreme composition. It is also noteworthy that, if the diopside and augite compositions of the ignimbrite-forming trachytes are tested against a variety of more mafic compositions (basalt to benmoreite), only a small number of pairs indicate equilibrium at a time, indicating that no single melt composition is suitable. Instead, the clinopyroxene populations appear to originate from a range of melts which are generally mafic to intermediate in composition.

Some qualitative insights may however still be gained from clinopyroxene chemistry. The TiO_2 and Al_2O_3 contents of clinopyroxene throughout the suite show substantial variations (~ 0.2 to 8.2 wt % and ~ 0.1 to 6.6 wt %, respectively), and, if considered alongside enstatite (En) content, allow the distinction of two chemical trends (Fig. 12). The first trend is marked by a rapid increase in both TiO_2 and Al_2O_3 over a relatively small decrease in En content, and comprises predominantly diopside phenocrysts from the enclaves, with a lesser contribution from the ignimbrites and the syenites. In contrast, the second trend is marked by consistently low TiO_2 and Al_2O_3 contents (< 0.5 wt %) at En contents between 20 and 40 mol. %, and primarily consists of augite phenocrysts from the ignimbrites, with a small number of enclave phenocrysts. The groundmass clinopyroxene of the enclaves, and the aegirine from the syenites appear to continue this trend to extremely low En contents (< 5 mol. %), where Al_2O_3 remains low, but TiO_2 rapidly increases to ~ 8 wt %. We suggest that the two observed trends indicate two separate stages in the crystallisation history of the erupted magmas. The transition between the first and second stages occurred at ~ En_{40}, where a change in the surrounding conditions prompted the crystallisation of

low-Ti, low-Al clinopyroxene. Although undoubtedly dependent upon additional factors such as melt composition, the link between the Al content of clinopyroxene and crystallisation pressure (e.g. Thompson, 1974; Beier *et al*., 2006) suggests that this may reflect a change in depth (i.e. initial storage at greater depth (termed here the mafic stage), followed by ascent and storage at a shallower depth (termed here the felsic stage)). Such multi-stage models have been applied at other Azorean volcanoes (Sete Cidades, São Miguel, Beier *et al*., 2006; Caldeira, Faial, Zanon *et al*., 2013; Zanon & Frezzotti, 2013; Furnas, São Miguel, Jeffery *et al*., 2016a), and other North Atlantic oceanic islands (e.g. La Palma, Klügel *et al*., 2000; Madeira, Schwarz *et al*., 2004). The continuation of this trend towards En values below 10 mol. % and the observed enrichment of TiO_2, as defined by the enclave groundmass and the syenites (Fig. 12), are likely to reflect late stage processes associated with near complete solidification of trachytic melt under low pressure conditions. Overall, these observations can be accounted for by a two-stage differentiation history, in which primitive, mantle-derived melts stall at a given depth in the crust and differentiate to broadly hawaiitic compositions, before ascending further, where continued differentiation leads to the generation of the erupted peralkaline silicic magmas.

The distribution of the dataset across these two trends shows that the majority of clinopyroxenes from the ignimbrites, the syenites, and the groundmass of the enclaves adhere to the felsic trend. The majority of mafic stage clinopyroxenes are found as phenocrysts in the trachyte enclaves, where felsic stage phenocrysts are also present. It is therefore suggested that the enclaves provide direct evidence not only for the mingling between trachyte and syenitic mush under comparatively low pressure conditions (see above), but also for the mingling of trachytes stored in shallow crustal reservoirs with ascending mafic magmas from below. In fact, these enclaves are likely

to represent hybridised magmas with multiple populations of crystals, including heavily reacted Mg-rich olivine, diopside, augite, and plagioclase derived from the mafic stage, alkali feldspar derived from the felsic stage, and, more rarely, aegirine-rich clinopyroxenes which are representative of the final portion of the felsic stage, having been clearly included from the surrounding syenite.

The origin of the ignimbrite-forming peralkaline trachytes

The petrogenetic processes that generate peralkaline silicic magmas have been envisaged to include: (1) where no compositional gap (Daly Gap) exists between mafic and silicic compositions, extended fractional crystallisation of a mantle-derived alkali basalt parent magma is typically considered (e.g. Barberi *et al*., 1975; Civetta *et al*., 1998; Peccerillo *et al*., 2007), possibly including some assimilation of the crust (e.g. Peccerillo *et al*., 2003); (2) where a Daly Gap is present, either partial melting of alkali gabbro cumulates (e.g. Bohrson & Reid, 1997) or extended fractional crystallisation are generally suggested (e.g. White *et al.*, 2009; Neave *et al.*, 2012); in the former case, peralkaline silicic magmas are envisaged to be produced directly (e.g. Avanzinelli *et al*., 2004), and may evolve further via fractional crystallisation (e.g. Trua *et al*., 1999). In the following section, a number of petrogenetic processes are explored, aimed at identifying key processes that generate ignimbrite-forming magmas on Terceira.

Fractional crystallisation

The prominent role of fractional crystallisation in the generation of evolved magmas in peralkaline silicic systems is well established (e.g. Barberi *et al*., 1975; Peccerillo *et al*., 2003; Macdonald *et al*., 2008; Macdonald, 2012), and was demonstrated

quantitatively for the series of young (predominantly < 20-23 ka) lavas from Terceira by Mungall & Martin (1995). However, in terms of their eruptive character and temporal occurrence (~ 20-23 to ~ 86 ka; Gertisser *et al*., 2010), the ignimbrites of Terceira may represent a petrologically distinctive system, and should be considered separately. Thus, to validate the role of fractional crystallisation, a number of petrogenetic models are applied here. To act as a starting point for each model, a variety of potential compositions are available (Self & Gunn, 1976). Mungall & Martin (1995) recognised three distinctive basaltic compositions, which they termed the on-rift, off-rift, and primitive basalts. Of these, the latter correspond to the silica-undersaturated series of Self & Gunn (1976), whilst the on- and off-rift basalts form the silica-oversaturated trend, and were linked to Pico Alto and Santa Bárbara, respectively (Mungall & Martin, 1995). Gertisser *et al*. (2010) attributed the Terceira ignimbrites primarily to the Pico Alto central volcano and in some cases possibly to Guilherme Moniz. For this reason, the on-rift basalts are considered to be the most suitable starting composition for mass balance and trace element models.

To evaluate simple fractional crystallisation processes, two least squares mass balance models (after Bryan *et al*., 1969) were performed using the IgPet software package (Carr, 1995), aiming to recreate a basalt to pantellerite fractionation trend (e.g. Barberi *et al*., 1974; White *et al*., 1979). Model results were considered acceptable if $\sum r^2 = < 1$. Each model comprised five compositional steps: 1) alkali basalt to hawaiite; 2) hawaiite to mugearite; 3) mugearite to benmoreite; 4) benmoreite to least evolved trachyte; 5) least evolved trachyte to most evolved trachyte. Whole-rock and mineral chemical data for alkali basaltic, hawaiitic, mugearitic, benmoreitic, and pantelleritic rocks were taken from Mungall (1993), whilst data for comenditic trachytic compositions were taken from the ignimbrites of

this study (Table 2). Two on-rift basalts which plot close the the basalt-hawaiite boundary in the TAS diagram (samples 89-13 and 89-19 of Mungall, 1993) were selected as suitable parent magma compositions on the basis of having the highest Mg# (58 and 53, respectively; mol. $Mg/(Mg+Fe^{2+})*100$) and lowest Zr content (168 and 188 ppm, respectively), alongside no clear evidence for crystal accumulation. However, these compositions are not indicative of primary melts, and so the determined degrees of fractionation (i.e. percentage of solid removed as crystals) should be considered to be minima.

Both major element mass balance models are in broad agreement that the least evolved trachyte compositions can be reliably reproduced (average $\sum r^2 = 0.178$) by 84 to 85 % fractionation of an assemblage of plagioclase (46 to 50 %), clinopyroxene (26 %), olivine (10 to 11 %), Ti-magnetite (4 to 7 %), ilmenite (4 %), and apatite (2 to 3 %). The most evolved trachyte compositions can be produced by a further 14 to 19 % fractionation of the remaining residual liquid (87 % total from parent) of an assemblage that is dominated by alkali feldspar (89 to 92 %), olivine (4 to 5 %), clinopyroxene (0 to 2 %), Ti-magnetite (3 %), and apatite (1 %) (average $\sum r^2 = 0.329$) (Jeffery, 2016). In contrast to the formulations of Mungall & Martin (1995), the inclusion of amphibole at any stage of the models leads invariably to failure.

To investigate the role of fractional crystallisation under variable P-T-fO_2 conditions, ~ 200 fractional crystallisation models were run using the Rhyolite-MELTS software v. 1.2 (Ghiorso & Sack, 1995; Asimow & Ghiorso, 1998; Gualda *et al*., 2012). For each model, sample 89-19 (also used for the mass balance models above) of Mungall (1993) was considered to be the most suitable starting composition (Jeffery, 2016). Fractional crystallisation models were generated over three starting water contents (0.5, 1.5, and 2.5 wt %), four isobaric pressures (50, 150, 250, and 500

MPa, representative of the uppermost, upper, middle, and lower crust, respectively) and redox conditions ranging from FMQ +2 to FMQ -2 (Jeffery, 2016). Additional polybaric models were run in which the pressure was changed from 500 to 150 MPa at either 1,100 or 1,000 °C, which corresponds to hawaiitic or benmoreitic compositions, respectively. These polybaric models were intended to simulate a general transition from deep to shallow crustal conditions, corresponding to depths of ~ 15 km (lower crust beneath the Azores; cf. Beier *et al*, 2006) and 2 to 4 km, respectively. The following mineral phases, having been identified in the relevant lithologies of Terceira, were allowed to crystallise in the model: feldspar, clinopyroxene, olivine, biotite, quartz, apatite, Ti-magnetite, and ilmenite. Hornblende was also permitted to crystallise due to its potential importance during the earlier portion of the liquid line of descent (e.g. Mungall & Martin, 1995). Each model was evaluated based upon its capability to reproduce the major element compositions of the ignimbrite formations and the Terceira liquid line of descent.

Overall, the results of modelling indicate that the major element compositions of the Terceira ignimbrites can be best reproduced by a polybaric model in which the melt differentiates at 500 MPa until it has reached a hawaiitic composition (~ 1,100 °C), at which point the pressure is reduced to 150 MPa (Jeffery, 2016). Relatively reducing conditions (FMQ -1) and a hydrous parental basalt composition (1.5 wt % H_2O) produced the best fit with the observed major element trends (Fig. 7). For this model, olivine is the liquidus phase, and exhibits two crystallisation intervals (1,180 to 1,150 and 1,060 °C onwards), which may be an artefact of the MELTS software. This is followed by clinopyroxene (1,160 to 1,090 ºC), ilmenite (1,140 ºC onwards), apatite (1,140 to 1,100 and 1,040 °C onwards), Ti-magnetite (1,100 ºC onwards), and feldspar (1,050 ºC onwards). The total fractionation at 850 °C is 74 %, of a mineral

assemblage dominated by clinopyroxene (38 %), feldspar (37 %), olivine (11 %), Ti-magnetite (8 %), apatite (3 %), and ilmenite (3%). Predicted H_2O_{melt} values are compatible with the results of FTIR and alkali feldspar-melt hygrometry, ranging from 3.97 wt % to 5.94 wt % for modelled melts with peralkalinity indices of 0.97 and 1.43, respectively. Furthermore, predicted melt temperature values are broadly compatible with the results of both two-oxide and alkali feldspar-melt thermometry, ranging from ~ 870 to ~ 810 ˚C for the same range in peralkalinity indices. At temperatures below ~ 850 ˚C, the models were less successful and frequently failed to run to completion, suggesting that the final portions of the liquid line of descent, represented by the syenite nodules and their intercumulus assemblages, cannot be adequately modelled using Rhyolite-MELTS. It is noteworthy that feldspar compositions predicted by Rhyolite-MELTS for temperatures similar those predicted by themometric methods (~ 940 to 800 ˚C) were typically more calcic than those observed in the rocks, achieving compositions within the anorthoclase range only at the lowermost temperatures predicted by thermometric methods. However, it should be noted that at temperatures below 800 ˚C the model predicted two feldspars simultaneously. In contrast, predicted clinopyroxene compositions (occurring only at temperatures between 1,160 and 1,090 ˚C, and therefore in mafic liquids) fit well with the observed compositions, particularly with the more Mg-rich compositions observed within the PNI, LMI, and the syenite-hosted enclaves. Similarly, the predicted olivine compositions compare well with the observed compositions. Over the temperature range predicted by themormetric methods (~ 940 to 800 ˚C), Rhyolite-MELTS predicts olivine compositions with a range of Fa_{65-92}, compared to the observed range of Fa_{59-82}.

In addition to supporting fractional crystallisation as the dominant mechanism of differentiation within the Terceira suite, this model also provides further validation of the pre-eruptive P-T-fO_2 conditions determined via thermobarometry above. For example, isobaric models run at 500 MPa invariably fail to achieve the SiO_2 and total alkali contents that are observed in the ignimbrites, suggesting that a significant proportion of the liquid line of descent is representative of shallow crustal conditions. This is consistent with Mungall & Martin (1995), who suggested that the on-rift basalts evolved to more silicic compositions at relatively shallow depths. However, isobaric models run at 150 MPa fail to achieve the total alkali contents observed in the data. The inclusion of an initial, comparatively brief step at higher pressure conditions (for our purposes, 500 MPa was used to represent lower crustal conditions) negated these discrepancies. Utilising an initial step at conditions below 500 MPa (e.g. 250 MPa), failed to have the same effect. Altering the redox conditions to > FMQ leads to the development of peralkalinity at higher MgO contents than observed on Terceira, suggesting that the calculated values described above (FMQ -1 to -2) are feasible. Similarly, the highest and lowest initial water contents lead to the development of peralkalinity at lower or higher MgO contents, respectively, most likely due to the predicted control of water content upon the onset of plagioclase crystallisation.

To further investigate the role of fractional crystallisation, and to evaluate the applicability of partial melting of various crustal lithologies as a petrogenetic process, closed system Rayleigh fractional crystallisation (RalFC) and batch melting models for selected trace elements were produced using the Rayleigh fractionation equation and the batch melting equation. (Fig. 13). The final RalFC trends comprise three stages, each calculated using phase assemblages and proportions predicted by the most suitable Rhyolite-MELTS model (see above): 1) clinopyroxene + olivine +

ilmenite + Ti-magnetite + apatite; 2) plagioclase + olivine + Ti-magnetite + apatite; 3) alkali feldspar + olivine + Ti-magnetite + apatite. Partition coefficient values were taken from the GERM KD database (www.earthref.org/KDD; Nielsen, 2008) and are given in Table 3. These trends are most evident in Figs 13b, c, where the modelled trends for both Sr and Ba are characterised by an initial, steep positive slope (stage 1), followed by a steeply negative slope (stage 2). Finally, both trends become distinctly flat (stage 3). RalFC models for incompatible elements such as Zr and Nb provide a good fit to the trend observed for Terceira and indicate that the compositional range of the ignimbrites can be accounted for by between ~ 65 and 90 % fractionation of an alkali basalt parent. The RalFC models for compatible elements such as Sr and Ba (as well as for Cr and Ni; not shown) are less well defined due to the substantial scatter observed in the Terceira suite, particularly within the intermediate compositions. However, modelled trends adhere closely to the generally low concentrations of Sr, Cr, and Ni observed in the suite. The model fit to the Ba data is poor due to the substantial scatter in the data, with the majority of the data plotting above the RalFC trend. In this case, the observed scatter is interpreted to reflect the variable degrees of alkali feldspar accumulation and assimilation, as evidenced by the presence of resorbed feldspars throughout the suite. Overall, these models are in agreement with incompatible element models, suggesting that the compositions observed in the ignimbrites can be produced by between ~ 65 and ~ 90 % fractional crystallisation.

In contrast, batch melting models calculated for hypothetical gabbroic, syenodioritic, and syenitic crustal lithologies with variable mineral proportions are almost exclusively incompatible with the trends observed in the Terceira suite (Fig. 13). For example, partial melting of either gabbroic or syenodioritic rock compositions yield trends that deviate significantly from the Terceira suite (e.g. Zr vs.

Nb; Fig. 13a), and generally fail to achieve the high concentrations of incompatible elements and extremely low concentrations of compatible elements (e.g. Sr, Ba; Figs 13b, c). Partial melting of a syenitic crustal lithology provides a better fit, but requires degrees of melting in excess of 50 % and notably cannot generate the least evolved trachyte compositions of the ignimbrites (~ 400 to 800 ppm Zr).

In summary, the results presented here suggest that the ignimbrites of Terceira can be accounted for by extended fractional crystallisation of a basaltic parental magma. Although the role of partial melting of crustal lithologies such as alkali gabbro or syenodiorite cannot be ruled out entirely, model results indicate that any contribution from such processes is small and probably limited to assimilation of syenitic rocks. Various petrogenetic models are in broad agreement that the entire compositional range exhibited by the ignimbrites of Terceira can be accounted for by between ~ 65 and ~ 90 % fractionation. Overall, the ignimbrite-forming peralkaline trachytes of Terceira appear to have formed in a two stage fractionation process, with an initial higher pressure stage in the lower crust, and a later, more significant shallow crustal stage.

In-situ crystallisation

Syenite whole-rock major element compositions are similar to the trachytes (Fig. 6a), and the depletion of compatible trace elements such as Sr, Ba, and P (attributed here to fractional crystallisation; Figs 8c, d) are also present, and may be even more extreme. If the syenites represent cumulate material derived from the fractional crystallisation of trachytic magmas, then they would exhibit compositions that are uniformly less evolved than the ignimbrite-forming trachytes. Additionally, the syenites exhibit negative Eu anomalies which are comparable to the trachytes (Figs 8a, b). The ignimbrite-forming trachytes exhibit a negative correlation between

Eu/Eu* and differentiation indices such as Zr and Nb, suggesting that any accumulation of feldspar would buffer, or even counteract, the continued development of a negative anomaly. Based upon the petrographic and geochemical characteristics, it is therefore suggested that the syenitic autoliths do not represent fragments of the cumulate from which the trachytes were derived, but instead provide direct evidence for the role of *in situ* crystallisation of trachytic magma, most likely in the thermal boundary layer at the edge of a magma reservoir (cf. Tait *et al*., 1989; Turbeville, 1993; Widom *et al*., 1993).

Magma mingling and remobilisation of crystal mush

The rocks of Terceira provide abundant evidence for the role of open system processes such as magma mingling and magma interaction with partially or totally solidified crystal mushes. Mungall (1993) reports trachytic lavas containing mafic enclaves, as well as disaggregated and partially melted syenitic autoliths in basaltic lavas, providing evidence for physical interaction of mafic and silicic magmas. He cites reverse zonation of phenocryst phases to infer the mixing of intermediate magmas shortly before eruption. The syenite-hosted enclaves of this study provide direct evidence for the mingling of variably evolved silicic magmas and, or, crystal mushes. If the syenite autoliths are considered to represent randomly sampled portions of a crystal mush derived from *in situ* crystallisation in a thermal boundary zone, then it is suggested that the syenite-hosted enclaves must indicate the injection of the least evolved trachytes of this study into another trachytic reservoir, passing through the marginal crystal mush. Although it cannot be ruled out that the syenites may instead represent significantly older, crustal lithologies, the prevalence of fresh, unaltered textures does not support this interpretation. Furthermore, the intruding trachyte contains a mixed phase assemblage, in which a basaltic assemblage of diopside, Mg-

rich olivine, and bytownite is found alongside a more silicic assemblage of oligoclase, anorthoclase and augite, implying that the basaltic assemblage is antecrystic, derived from mixing of mafic magma with a trachytic magma (cf. Ferla & Meli, 2006). The described difficulty in establishing an equilibrium liquid composition for the clinopyroxenes of this study is likely to be a consequence of this mixing process.

In fact, the trachytic assemblage may also be, to some extent, antecrystic. The sieve-textures observed at the rims of the largest anorthoclase crystals may have resulted from the mingling between ascending hawaiites and trachytes stored in the shallow crust, causing reheating of the latter, implying that these crystals represent the true phenocryst assemblage of the trachyte. Alternatively, these textures may indicate disequilibrium between the least evolved trachyte and large anorthoclase crystals originating from the surrounding syenitic mush, introduced during trachyte-syenite interaction and subsequent disaggregation of the latter. Some evidence exists for the remobilisation and disaggregation of syenitic mush in the form of glomerocrystic fragments comprising large, cumulus (and often perthitic) alkali feldspar and intercumulus aegirine-augite or Na-amphibole, two phases that are not observed in any lithology other than the syenites. The presence of such glomerocrysts as well as individual feldspar crystals which do not exhibit a perthitic texture suggests that both processes occur.

Further evidence for mingling may be seen in the calculated RalFC models, where a number of compositions deviate from the modelled trend (Fig. 13b). In particular, the syenite-hosted enclaves, intermediates (mugearites and benmoreites) and a number of the ignimbrite-forming trachytes exhibit Sr concentrations which form a mixing trend in which the trachytes of the LMI, PNI and Ign-i are mixed with hawaiitic compositions (Fig. 13b). This is consistent with the observed petrographic

features for mingling in these lithologies (abundant resorbed crystals), mineral chemistry (rare Mg-rich olivine and plagioclase) and also, to some extent, thermometric and hygrometric evidence (higher temperatures and lower water contents predicted for the LMI; Fig. 10b). This mixing trend is also observed for other compatible elements such as Ba, Cr, and Ni (Cr and Ni not shown), but is less distinct due to the data scatter. In particular, Ba shows a potential (but highly scattered) mixing trend between hawaiites and trachytes. Furthermore, concentrations of Ba within the syenite-hosted enclaves reach concentrations in excess of both the maximum concentration predicted by closed system RalFC (~ 800 ppm), and the proposed mixing trend, up to values as high as ~ 1250 ppm. The enrichment of Ba in whole-rock analyses is a feature that is typical of peralkaline systems and is frequently attributed to the accumulation and resorption of alkali feldspars (e.g. Macdonald *et al*., 2008; Macdonald, 2012). The presence of feldspars with resorption textures throughout the ignimbrites provides evidence for mingling in the ignimbrite-forming trachytes of Terceira.

The magmatic plumbing system of the ignimbrite-forming eruptions

Implications of viscosity for differentiation

Viscosity is of first order importance for both the evolution and eruption of magmas, and is controlled by magma temperature, composition, abundance of volatile components, solid fraction and bubble content (e.g. Shaw, 1972; Lejeune & Richet, 1995; Dingwell *et al*., 1996; Dingwell & Hess, 1998; Manga *et al*., 1998; Llewellin *et al*., 2002b; Costa, 2005; Giordano *et al*., 2006). To estimate the pre-eruptive viscosity of the ignimbrite-forming trachytes, the model of Giordano *et al*. (2008) was used, as

this model has been calibrated for a wide range of magma compositions and has been shown by recent experimental work to be able to reproduce magma viscosity to within < 0.2 log units (Vona *et al*., 2011). The minimum and maximum temperature and H_2O_{melt} estimates and the average composition of each ignimbrite were used as input parameters. The total range of crystal-free viscosity estimates varies from $10^{3.1}$ to $10^{4.0}$ Pa s. These values were converted into magma viscosities using the method of Dingwell *et al*. (1993):

$$\eta_{magma} = \eta_{melt}(1 + 0.75((f/f_m)/(1-f/f_m)))^2$$

where η_{magma} and η_{melt} are the viscosities of magma and melt, respectively, f is the volume fraction of crystals, and f_m is the concentration of crystals required to achieve an infinite viscosity. The latter value was set to 0.6, following Andújar & Scaillet (2012), whilst the volume fraction of crystals was set to values between 0 and 0.2, in accordance with petrographic observations (cf. Self, 1971; Gertisser *et al*., 2010). Results exhibit a total range of viscosities extending from $10^{3.1}$ (aphyric, high water) to $10^{4.3}$ Pa s (20 % crystallinity, low water), and indicate that the pre-eruptive viscosities of the ignimbrite-forming trachytes were relatively low, extending to values more than 1 order of magnitude lower than is typical for metaluminous silicic melts (~ $10^{4.5}$ Pa s, Scaillet *et al*., 1998). This observation has significant implications not only for eruptive behaviour (cf. Andújar & Scaillet, 2012) but also for the dominant mechanism of differentiation within the trachytes. Due to the difficulties of two-phase flow (i.e. crystals settling or floating through a silicate melt) in relatively cool, high viscosity magmas, the generation of crystal-poor silicic magmas is

frequently attributed to the extraction of interstitial melt from a crystal mush via processes such as compaction, hindered settling, micro-settling, and gas-driven filter pressing (Sisson & Bacon, 1999; Bachmann & Bergantz, 2004; Hildreth, 2004; Pistone *et al.*, 2015). However, the application of such models to peralkaline magmatic systems is hindered by the reduced viscosities associated with peralkalinity, which may allow efficient crystal-melt segregation via crystal settling (Macdonald, 2012), as well as the apparent absence of erupted crystal-rich magmas typically termed "monotonous intermediates" in metaluminous systems (Hildreth, 1981). As such, the efficiency of two-phase flow in the pre-eruptive magma system of the Terceira ignimbrites was evaluated via the calculation of Stokes' settling velocities for alkali feldspar crystals, supplemented by the hindered settling equation, which allows the estimation of settling rates in polydispersed suspensions (Bachmann & Bergantz, 2004):

$$U_{hs} = U_{Stokes} \times f(c)$$

where U_{hs} is the hindered settling velocity, U_{Stokes} is Stokes settling velocity, and f(c) is a correction factor calculated as:

$$f(c) = \frac{(1 - c)^2}{(1 + c^{1/3})^{\left[\frac{5c}{3(1-c)}\right]}}$$

where c is equal to the crystal fraction. Crystal sizes were set to 2 mm, in accordance with petrographic observations. Melt densities were set to 2,250 kg/m^3, based upon the typical densities predicted by Rhyolite-MELTS. Results indicate that the alkali feldspars in the highest viscosity trachytes are capable of settling at rates of between 1.99 (unhindered) and 0.39 m/a^{-1} (hindered settling, 40 % crystallinity), whilst those of the lowest viscosity trachytes reach rates of between 19.00 (unhindered) and 3.78 m/a^{-1} (hindered settling, 40 % crystallinity). These estimates suggest that, unlike typical metaluminous rhyolites (where calculated settling rates are unlikely to exceed ~ 0.67 m/a^{-1}, assuming unhindered settling and melt viscosity of $10^{4.5}$ Pa s), the peralkaline ignimbrite-forming trachytes of Terceira may still be able to segregate melt from crystals efficiently via crystal settling despite their silicic compositions, as suggested at Furnas, São Miguel (Jeffery *et al*., 2016a), although a contribution from *in situ* crystallisation at the margins of a magma reservoir and associated migration of residual liquids is also feasible. Rapid crystal-melt segregation would not only account for the often crystal-poor nature of the erupted magma, but could also promote the formation of density stratification. The scatter observed for Ba concentrations throughout the suite, and at other peralkaline volcanic centres (e.g. Macdonald *et al*., 2008; Macdonald, 2012), likely indicates the ease with which peralkaline trachytes can, through rapid crystal settling, lose Ba to underlying melt, or gain Ba by receiving alkali feldspar from overlying melt.

Zoned magma bodies

Despite their major element homogeneity, the ignimbrites of Terceira exhibit substantial internal trace element variations (e.g. ~ 900 to ~ 1,350 ppm Zr in the CCI; Gertisser *et al*., 2010) which, based upon the often crystal-poor nature of the juvenile clasts (typically less than 10 % crystallinity on a vesicle free basis), are unlikely to

reflect a mineralogical influence. A minor basal pumice fall of the VFI exhibits an even more extreme compositional variation when compared to the overlying ignimbrite units (~ 2,250 ppm Zr compared to ~ 700 ppm, respectively), despite the similarly low crystal content of alkali feldspar. On the basis of the trace element RalFC models presented above, this reflects up to ~ 15 % fractionation. These phenomena are typically considered to originate from the eruption of a zoned magma body (e.g. Hildreth, 1981; Williams *et al*., 2013), assuming that the zoning patterns have not been altered by syn-eruptive conduit processes. Alternatively, the eruption of multiple discrete melt pockets within a crystal mush has also been invoked (e.g. Shane *et al*., 2008; Cooper *et al*., 2012; Ellis & Wolff, 2012; Zanon *et al*., 2013; Ellis *et al*., 2014; Pimentel *et al*., 2015). However, the data of this study indicate that the observed chemical zoning within the ignimbrites of Terceira is generally gradational rather than abrupt (one exception is discussed below). Although it cannot be ruled out that the observed zonation may be contributed to by processes such as remelting of cumulate material (in this case envisaged to be represented by the syenite nodules) (e.g. Wolff *et al*., 2015) or the presence and subsequent eruption of discrete magma pockets (e.g. Ellis *et al*., 2014), the strong evidence discussed above suggests that the pre-eruptive magma system which generated the ignimbrites of Terceira typically comprised a single, gradationally-zoned melt body, with the most evolved and most volatile-rich trachytes overlying progressively less evolved trachytes. The preservation of this zonation until eruption indicates that convection, which might be expected to be enhanced by low melt viscosities, was not sufficient to enable the reservoir to homogenise, possibly due to the formation of multiple, individually convecting layers (Huppert *et al*., 1986). One exception to this observation is the LMI, where available data indicate a more restricted range of incompatible trace elements

(~ 760 to ~ 910 ppm Zr). The LMI exhibits abundant evidence for having been mixed with a hotter, less differentiated magma prior to eruption (e.g. presence of resorbed antecrysts including plagioclase, high pre-eruptive temperatures, mixing trend with hawaiitic compositions). The rather limited chemical zonation of the LMI may therefore reflect a large-scale homogenisation event, in which an influx of hotter magma initiated convection within the reservoir, and triggered its eruption shortly afterwards.

Although the model applied in this study is based around a single, compositionally-zoned magma body, the CCI offers some further complexity which may provide some indication of a more complex pre-eruptive magmatic system. Juvenile pumice clasts from the basal pumice fall and dilute pyroclastic density current (surge) deposits of the CCI exhibit incompatible element enrichment compared to the overlying ignimbrite (e.g. ~ 1,000 vs. ~ 650 ppm Zr). However, a number of analyses from the overlying ignimbrite record incompatible enrichments that are even greater than the basal deposits (> 1,000 ppm), suggesting that more complex models for the geometry of the underlying magma system may yet have some role to fully account for the observed chemical variability.

A model for the magmatic system

Here we present a conceptual model for the magma plumbing system from which the ignimbrite-forming episodes of Terceira were fed (Fig. 14). Considering the results of thermodynamic modelling and water solubility, we infer the presence of a magma storage zone at shallow crustal depths (~ 2 to 4 km, assuming a crustal density of 2,800 kg/m^3). This is consistent with the low concentrations of S and CO_2 found in melt inclusions. At least the upper portion of this zone is considered to be exclusively

trachytic in composition, based upon the entirely trachytic compositions of alkali feldspar-hosted melt inclusions.

The most applicable Rhyolite-MELTS model included a polybaric regime in which basaltic magmas undergo an initial fractionation period, moving compositionally towards hawaiitic compositions at comparatively high pressures (~ 500 MPa), equivalent to the lower crust beneath the Azores (~ 15 km; cf. Beier *et al*., 2006). We therefore suggest that beneath Terceira ascending mantle-derived basalts are likely to stall in the lower crust and differentiate to hawaiitic compositions via fractional crystallisation of a clinopyroxene-dominated assemblage, before ascending further and stalling in the lower portion of the shallow crustal zone. The mixed crystal populations found in syenite-hosted trachytic enclaves, facilitate the inference that the hawaiites are introduced into the dominantly trachytic magmas of the shallow crustal system in a mixing zone in the lower regions of the shallow system. Here, they are envisaged to mingle and mix with trachytes, generating hybridised trachytes represented by the syenite-hosted enclaves, with multiple phase assemblages: (1) anorthoclase, (2) diopside + Mg-rich olivine + bytownite, and (3) oligoclase + augite (cf. Bacon & Metz, 1984; Bacon, 1986; Ferla & Meli, 2006). Considering the overwhelming dominance of anorthoclase in the ignimbrite-forming trachytes, the first assemblage is considered to be representative of the trachytes and is therefore the true phenocryst assemblage of the upper crustal system. The second is the phenocryst assemblage of the ascending hawaiites introduced during mixing. This is consistent with the high Al_2O_3 and TiO_2 contents of the diopside phenocrysts, which indicate crystallisation within a different magmatic environment (Fig. 12). Due to the adherence of augite phenocrysts to the felsic trend (described above; Fig. 12), the third assemblage cannot be associated with the ascending hawaiites, and therefore

must be attributed to the shallow magma storage zone. Oligoclase is found only in the LMI and is heavily resorbed. In addition, the augite population of the ignimbrite juvenile clasts is not in chemical equilibrium with the host trachyte. Furthermore Rhyolite-MELTS and mass balance models predict little to no clinopyroxene crystallisation in trachytic compositions. the more sodic clinopyroxene found in the syenitic autoliths and the groundmass of the syenite-hosted enclaves clearly indicates its formation at temperatures lower than those of the trachytes (< 800 °C). The oligoclase and augite observed in the enclave magmas are therefore considered to represent an assemblage derived from the benmoreitic or least evolved trachyte hybrid magmas which result from the mixing of relatively small proportions of hawaiite with trachyte.

The hybridised trachytes may then ascend further, out of a lower mixing zone and into the upper regions of the shallow magma storage zone, where the most differentiated magmas are inferred to be present. The mineral assemblages and calculated viscosities of these trachytic magmas suggest that differentiation is likely to be controlled by the crystallisation of anorthoclase, driving the melt towards the most evolved trachyte compositions. The compositional zonation of these magma bodies is likely to form as the lower density, more evolved liquids migrate upwards to form a lens of low viscosity, hydrous, crystal-poor highly evolved trachyte. Additional processes which may play a role in the construction of a zoned magma body include the ascent of bubbles through volatile-saturated magma which may lead to upward migration of alkalis, halogens, and other fluid-mobile elements (Hildreth & Wilson, 2007) and the generation of low density, hydrous melts via sidewall crystallisation (e.g. Huppert *et al*., 1986). The preservation of this zonation until eruption may be linked to the development of a system of multiple, individually convecting layers

(Huppert & Sparks, 1984), which would likely be enhanced by the low magma viscosities described above, or alternatively a strong density contrast associated with the range of water contents (cf. Hildreth & Wilson, 2007), as indicated by the water contents measured in alkali feldspar-hosted melt inclusions and calculated via alkali feldspar hygrometry (~ 2 to 6 wt %).

Due to the dominance of trachytic compositions at this uppermost level, individual magma reservoirs are likely to be surrounded by a marginal syenitic crystal mush developing via *in situ* crystallisation in the thermal boundary zone. This mush may then be sampled during eruption, providing the syenite autoliths observed in the CCI and, to some extent, in the LAI. The presence of hybridised trachytic enclaves within these syenitic autoliths is considered to record the injection of hybridised trachyte into an upper trachytic reservoir, through the marginal (basal) mush zone. The abundance of miarolitic cavities in both enclave and host syenite provide further evidence for the shallow depth of this magma storage zone. Subsequent mixing of these hybrids with the overlying trachytes may contribute to the development of zonation of the magma body and likely accounts for the occurrence of resorbed oligoclase, augite, and more rarely, calcic plagioclase, diopside, and Mg-rich olivine in the LMI and the PNI. Furthermore, the replenishment of the uppermost reservoir with hybridised trachyte may act as a trigger for eruption. The calculated rates of crystal settling imply that the antecrystic population introduced during mixing would settle rapidly, implying relatively rapid eruption following replenishment.

Finally, a note should be made concerning the GVI which, unusually for peralkaline silicic systems, contains abundant biotite phenocrysts. Based upon Scaillet & Macdonald (2001), this indicates pre-eruptive temperatures below 700 ˚C, at conditions close to water-saturation. This is consistent with the results of

thermometric and hygrometric modelling applied in this study, which predict cooler and wetter pre-eruptive conditions for the GVI than for any of the other ignimbrite formations of Terceira (Fig. 10). Furthermore, the thermodynamic models of Jeffery (2016) predict that, for the most suitable pre-eruptive conditions found in this study, biotite crystallisation occurs at redox conditions close to FMQ and FMQ +1. It is therefore suggested that the GVI represents a magma body which was cooler, closer to water-saturation, and somewhat more oxidised than those which fed the other ignimbrite-forming eruptions.

The ignimbrites in the context of the magmatic suite of Terceira

When considered in the context of the Terceira suite, the ignimbrites, syenites, and enclaves lie close to the end (< 2 wt % MgO) of a single liquid line of descent which characterises the volcanic products of the island (Figs 6, 7). Mungall & Martin (1995) further subdivided this trend, noting the presence of a more oxidising Santa Bárbara trend at low MgO contents (< 1 wt. %). The mafic to intermediate region of this trend comprises the various lava flows and scoria cones associated with the fissure zone (Self, 1974, 1976; Mungall & Martin, 1995; Madureira *et al*., 2011), whilst the silicic region is made up of the syenite enclaves, the ignimbrites (including whole-rock, melt inclusions and groundmass glass) and the syenites (Mungall, 1993; Gertisser *et al*., 2010; Tomlinson *et al*., 2014; this study), as well as the lava domes and coulées of Pico Alto, and residual glass in syenite xenoliths (labelled P. Alto xenolith glass; Mungall & Martin, 1995), listed in order of increasing differentiation and peralkalinity. The addition of a sixth step to the major element mass balance models discussed above, in which the most evolved trachyte composition is utilised as a parental magma composition and a pantellerite is used as a daughter, indicates that the

pantellerites, which are typical of Pico Alto, can be generated via 72 to 79 % fractionation (93 to 97 % total from basaltic parent) of an assemblage comprising predominantly alkali feldspar (92 %), clinopyroxene (3 %), olivine (2 %), Ti-magnetite (2 %), and apatite (< 1%) (average $\sum r^2 = 0.496$). The ignimbrite-forming magmas would therefore have evolved to pantelleritic compositions, had they been stored long enough to allow continued fractionation.

In the overall trend, Al_2O_3 contents show little variation until ~ 1 wt. % MgO, indicating only a minor role for plagioclase feldspar (Fig. 7). This point corresponds broadly to benmoreitic compositions, and is in agreement with the results of Rhyolite-MELTS modelling. At MgO contents of < 1 wt %, Al_2O_3 rapidly declines from ~ 16 to ~ 5 wt %, indicating significant fractionation of initially plagioclase and then alkali feldspar. A similar, kinked trend is observed in FeO_t and TiO_2, where concentrations show little change until ~ 4 wt % MgO, when they decline from ~ 12 to ~ 4 wt %, and ~ 3.5 to < 1 wt %, respectively. As is common in peralkaline systems, a late-stage (< 1 wt % MgO) FeO_t enrichment is present, leading to concentrations of up to ~ 15 wt % in the most evolved trachytic liquids. The P.I. of the system shows a gradual increase, becoming peralkaline close to the benmoreite-trachyte boundary, followed by a rapid increase during the final stages.

A compositional gap is observed in the suite at ~ 1.5 to 3.0 wt % MgO, which likely corresponds to the previously described Daly Gap for Terceira (Self & Gunn, 1976). Although Mungall & Martin (1995) used monzonitic autoliths to bridge this gap, no such autoliths are reported from Pico Alto. However, the benmoreitic lavas of Mungall (1993) and the syenite-hosted enclaves of this study begin to narrow this gap. At Pico Alto, this gap may reflect a genuine scarcity of intermediate compositions due to rapid melt evolution at intermediate compositions. Based upon the results of this

study, we also suggest that the Daly Gap is likely to reflect prevalent magma hybridisation in the shallow magma storage zone (e.g. Storey *et al*., 1989; Araña *et al*., 1994; Peccerillo *et al*., 2003; Sumner & Wolff, 2003; Avanzinelli *et al*., 2004; Ferla & Meli, 2006; Lowenstern *et al*., 2006; Romengo *et al*., 2012). In effect, the intermediate melt compositions are rarely seen because they are only likely to form during the mixing of ascending hawaiite and comparatively large volumes of trachyte in an established silicic magma storage zone. As such, they are rapidly lost, and are only recognised through the preservation of their relict phenocryst assemblages.

Overall, it should be noted that, despite its relatively low volume (typical eruptive volumes of ~ 1 to 2 km^3 DRE; Self, 1976; Gertisser *et al.*, 2010) and shallow crustal depth (~ 2 to 4 km), the ignimbrite-forming magma system of Terceira (i.e. the underlying magma system of Pico Alto and potentially Guilherme Moniz) appears to have remained relatively stable for up to ~ 60 kyr. At least seven ignimbrite-forming eruptions and many smaller scale eruptions have occurred within this time period, suggesting that the rates of magma supply to the shallow crustal system have remained relatively constant, allowing the system to remain thermally active in cold, upper lithosphere.

Control of magma viscosity on eruptive behaviour

Explosive activity derived from Pico Alto (and potentially Guilherme Moniz) is dominated by low pyroclastic fountaining eruptions with only briefly-sustained eruption columns. This eruptive behaviour is likely to be linked to the previously-described low pre-eruptive viscosities of the ignimbrite-forming magmas. To investigate the rheological changes induced by ascent-driven degassing, isothermal

magma viscosities were calculated for each of the ignimbrite-forming trachytes for water contents ranging from 0 to 6 wt %, assuming a crystal fraction of 0.2 in each instance. Magma compositions used were taken from each of the ignimbrite formations, as well as a typical Terceiran pantelleritic composition taken from Mungall & Martin, 1995. Results indicate that even total degassing of the ignimbrite-forming trachytes, which leads to an increase in viscosity of ~ 4 orders of magnitude (~ $10^{7.5}$ Pa s), is insufficient to achieve the threshold typically required for brittle fragmentation (10^{8} to 10^{9} Pa s; Papale, 1999; Giordano *et al.*, 2009) (Fig. 15a).

The viscosity of the ascending trachytes may be further influenced by degassing-induced microlite crystallisation (e.g. Sparks & Pinkerton, 1978). The rheological effects of such crystallisation are related to crystal abundance, size, shape, packing density, and the shear strain of the magma (e.g. Llewellin *et al.*, 2002; Caricchi *et al.*, 2008; Costa *et al.*, 2009; Di Genova *et al.*, 2013). To explore the effects of syn-eruptive microlite crystallisation upon the ignimbrite-forming trachytes, the viscosities of bubble-free, crystal-bearing magmas were calculated using the model of Vona *et al.* (2011), following Di Genova *et al.* (2013). Models were run for the minimum and maximum pre-eruptive melt viscosity estimates determined in this study ($10^{3.1}$ to $10^{4.3}$ Pa s, respectively). In each case, the strain rate was set to $\gamma = 1\ s^{-1}$, the crystal fraction was varied from 0.0 to 0.4, and the mean crystal aspect ratio was set to 7 (Hammer & Rutherford, 2002). Results indicate that during crystallisation, magma viscosity increases by 2.6 log units before approaching infinite values at a crystal fraction of ~ 0.36 (Fig. 15b). The rate of viscosity increase is non-linear and the greatest viscosity increase occurs above a crystal fraction of ~ 0.3 (cf. Di Genova *et al.*, 2013). Based upon the total crystal fraction of microlites in the samples of this study (< 0.1), this process is therefore unlikely to contribute more than a total increase

in viscosity of ~ 0.2 log units. As such, even when considered alongside the viscosity increase induced by degassing, the ascending trachytes are unlikely to reach the viscosities required for brittle fragmentation. Other processes not considered directly here must therefore be invoked, such as closed system degassing and the rheological effects of bubble formation.

This approach demonstrates how the peralkalinty-induced transposition of pre-eruptive magma viscosities to values lower than those typical of metaluminous magmas can have profound effects, not only upon pre-eruptive processes such as magmatic differentiation, but also upon eruptive behaviour. In this instance, pre-eruptive viscosity may have played a major role in the generation of the pyroclastic density current-producing eruptions of Terceira by inhibiting highly explosive convective volcanic activity, instead promoting low pyroclastic fountaining.

Implications for peralkaline magmatic systems

The magmatic plumbing system from which the rocks of this study were derived presents a variety of features which are characteristic of peralkaline silicic complexes (cf. Macdonald, 2012). For example, the erupted material is exclusively peralkaline and silicic in composition, suggesting that the uppermost part of the magmatic system has been stable for a sufficient period of time to allow the development of a shadow zone. In effect, ascending mafic magmas, which provide both the thermal energy and matter required to maintain the system in relatively cool, upper crustal conditions, are prevented from reaching the surface, instead being incorporated into the silicic magmas via mixing. In the case of Pico Alto, the only erupted evidence for the presence of basaltic magmas within the system is a relict phenocryst assemblage. It

therefore seems likely that this mixing process represents a primary contributor to the generation of the Daly Gap on Terceira.

Historically, the presence of a Daly Gap has been utilised as fundamental evidence for the primary role of partial melting as a petrogenetic process (e.g. Chayes, 1963; 1977). However, various studies have highlighted alternative processes which could lead to the generation of bimodal magmatism, such as density-based redirection of mafic magmas to the periphery of a volcanic centre (e.g. Peccerillo *et al*., 2003), rapid differentiation of intermediate compositions (e.g. White *et al*., 2009), high density and, or, crystal content of intermediate magmas preventing their eruption (e.g. Weaver, 1977). The evidence provided in this study suggests that magma mixing processes, invoked at many peralkaline volcanic centres (e.g. Gran Canaria, Canary Islands (Troll & Schmincke, 2002; Sumner & Wolff, 2003), Pantelleria, Italy (Ferla & Meli, 2006; Gioncada & Landi, 2010; Landi & Rotolo, 2015) represent an equally valid means of generating a Daly Gap (cf. Romengo *et al*., 2012). Overall, this suggests that peralkaline magmatic systems which are controlled primarily by fractional crystallisation are likely to undergo the following key evolutionary stages: 1) initiation of volcanic activity with mantle-derived mafic magmas ascending from the mantle and, or, lower crustal storage zones; 2) development of an upper crustal storage zone in which mafic magmas stall and differentiate towards peralkaline silicic compositions; 3) growth and stabilisation of the upper crustal magma storage zone, such that a relatively large volume of silicic magma is stored and maintained via periodic replenishment with comparatively small volumes of mafic magma. Within this scheme, there is a key transition between stages 2 and 3 in which the length of the fractional crystallisation-controlled liquid line of descent is split into two separate segments. In stage 2 the liquid line of descent extends from basalt to peralkaline

trachyte, whereas in stage 3, there are two separate liquid lines of descent; basalt to hawaiite, and metaluminous trachyte to peralkaline trachyte. In stage 2, intermediate magmas exist as the fractionation products of more mafic magmas, and will go on to fractionate further to produce trachytic compositions. At this point, their apparent absence is more likely to result from their density, crystal content, or their relatively brief existence (see above). In stage 3, intermediate magmas are instead formed only through the mixing of ascending hawaiites with trachyte, suggesting that they exist only briefly, until such time as they have been mixed in with the trachytes, thereby acting as a buffer to continued fractional crystallisation within the trachytes.

CONCLUSIONS

The ignimbrite-forming comenditic trachytes of Terceira can be generated by extended fractional crystallisation of hydrous (1.5 wt %), mantle-derived basaltic parental magmas at redox conditions around 1 log unit below the fayalite-magnetite-quartz buffer. Pre-eruptive water contents measured in melt inclusions and estimated via alkali feldspar hygrometry extend from 2.5 to 6.0 wt % and, based upon solubility models, indicate the presence of a prominent magma storage reservoir at shallow crustal depths (~ 2 to 4 km) in which silicic magmas are stored. Syenitic autoliths of similar whole-rock composition to the trachytes provide evidence for the *in situ* crystallisation of trachytic magmas in a thermal boundary layer in the upper crustal reservoir. The abundance of miarolitic cavities in these rocks also indicates shallow crustal conditions.

The results of thermodynamic modelling, as well as the minor presence of Al_2O_3- and TiO_2-rich clinopyroxenes, provides evidence for an initial high pressure

fractionation step in the lower crust, in which basalts differentiate via fractional crystallisation to hawaiitic compositions. Trachytic enclaves within syenite autoliths contain mixed crystal populations, indicating a two-stage mixing process in which ascending hawaiites are mixed with trachytic magmas in the base of the shallow crustal storage zone. This generates a hybridised trachyte, which then ascends further and is mixed with more evolved trachytes, passing first through a syenitic crystal mush at the margin of a magma reservoir.

Calculated magma viscosities for the ignimbrite-forming trachytes extend to values more than 1 order of magnitude lower than is typical for metaluminous silicic magmas. Estimated crystal settling rates suggest that fractional crystallisation is likely to remain a viable process in the trachytic magmas stored in the shallow crust, contributing to the substantial trace element compositional zonation observed in the ignimbrite formations. Major element mass balance modelling indicates that the most evolved, pantelleritic compositions of Terceira can be generated by continued fractionation of alkali feldspar from the ignimbrite-forming comenditic trachytes. The low pre-eruptive viscosities of the ignimbrite-forming magmas increases the overall difficulty of brittle fragmentation, which may reduce the likelihood of highly explosive (e.g. sustained eruption columns) eruptive behaviour and limit the majority of explosive activity to low pyroclastic fountaining. The sporadic mixing of comparatively low volumes of mafic magma into an established upper crustal silicic reservoir is envisaged to contribute to the generation of a Daly Gap on Terceira, with intermediate magmas existing only briefly before being mixed into trachytic magmas, effectively buffering fractional crystallisation in the silicic reservoir.

ACKNOWLEDGEMENTS

We gratefully acknowledge A. Tindle and A. Kronz for analytical support and access to electron microprobe facilities at the Open University, U.K., and the University of Göttingen, Germany, respectively. We are grateful to B. Leze and K. Preece for their support in the production of additional XRF analyses at the University of East Anglia, U.K. For diligent assistance in the field, K. Jeffery is also acknowledged. We are also grateful to P. Greatbatch and D. Wilde for the production of thin sections and invaluable assistance in the preparation of melt inclusions for analysis. An earlier form of this manuscript was greatly improved by the detailed and constructive comments of D. Neave, J. C. White, and G. Daly. We are also grateful to W. Bohrson for insightful comments which greatly improved the manuscript, and for editorial handling.

FUNDING

This work was supported by the Faculty of Natural Sciences Research Office, Keele University, who provided use of facilities and financial support. B. O'Driscoll acknowledges support from a Natural Environment Research Council (NERC) New Investigator Grant NE/J00457X/1 and a NERC Standard Grant NE/L004011/1. A. Pimentel was financially supported by CIVISA/CVARG.

REFERENCES

Andersen, D. J., Lindsley, D. H., Davidson, P. M. (1993) QUILF: A Pascal program to assess equilibria among Fe-Mg-Mn-Ti oxides, pyroxenes, olivine and quartz. *Computers and Geosciences* **19**, 1333-1350

Andújar, J., Scaillet, B. (2012) Relationships between pre-eruptive conditions and eruptive styles of phonolite-trachyte magmas. *Lithos* **152**, 122-131

Araña, V., Badiola, E. R., Hernán, F. (1973) Peralkaline acid tendencies in Gran Canaria (Canary Islands). *Contributions to Mineralogy and Petrology* **40**, 53-62

Araña, V., Marti, J., Aparicio, A., García-Cacho, L., García-García, R. (1994) Magma mixing in alkaline magmas: an example from Tenerife, Canary Islands. *Lithos* **32**, 1-19

Asimow, P. D., Ghiorso, M. S. (1998) Algorithmic modifications extending MELTS to calculate subsolidus phase relations. *American Mineralogist* **83**, 1127-1132

Avanzinelli, R., Bindi, L., Menchetti, S., Conticelli, S. (2004) Crystallisation and genesis of peralkaline magmas from Pantelleria Volcano, Italy: an integrated petrological and crystal-chemical study. *Lithos* **73**, 41-69

Bachmann, O., Bergantz, G. W. (2004) On the origin of crystal-poor rhyolites: Extracted from batholithic crystal mushes. *Journal of Petrology* **45**, 1565-1582

Bacon, C. R. (1986) Magmatic inclusions in silicic and intermediate volcanic rocks. *Journal of Geophysical Research* **91**, 6091-6112

Bacon, C. R., Hirschmann, M. M. (1988) Mg/Mn partitioning as a test for equilibrium between coexisting Fe-Ti oxides. *American Mineralogist* **73**, 57-61

Bacon, C. R., Metz, J. (1984) Magmatic inclusions in rhyolites, contaminated basalts, and compositional zonation beneath the Coso volcanic field, California. *Contributions to Mineralogy and Petrology* **85**, 346-365

Barberi, F., Ferrara, G., Santacroce, R., Treuil, M., Varet, J. (1974) A transitional basalt-pantellerite sequence of fractional crystallisation, the Boina Centre (Afar Rift, Ethiopia). *Journal of Petrology* **16**, 22-56

Beier, C., Haase, K. M., Hansteen, T. H. (2006) Magma evolution of the Sete Cidades volcano, São Miguel, Azores. *Journal of Petrology* **47**, 1375-1411

Beier, C., Haase, K. M., Turner, S. P. (2012) Conditions of melting beneath the Azores. *Lithos* **144-145**, 1-11

Black, S., Macdonald, R., Kelly, R. (1997) Crustal origin for peralkaline rhyolites from Kenya: evidence from U-series disequilibria and Th-isotopes. *Journal of Petrology* **38**, 277-297

Bohrson, W. A., Reid, M. R. (1997) Genesis of silicic peralkaline volcanic rocks in an ocean island setting by crustal melting and open-system processes: Socorro island, Mexico. *Journal of Petrology* **38**, 1137-1166

Bryan, W. B. (1966) History and mechanism of eruption of soda-rhyolite and alkali basalt, Socorro island, Mexico. *Bulletin of Volcanology* **67**, 42-56

Bryan, W. B., Finger, L. W., Chayes, F. (1969) Estimating proportions in petrographic mixing equations by least-squares approximation. *Science* **163**, 926-927

Calvert, A. T., Moore, R. B., McGeehin, J. P., Rodrigues da Silva, A. M. (2006) Volcanic history and $^{40}Ar/^{39}Ar$ and ^{14}C geochronology of Terceira Island, Azores, Portugal. *Journal of Volcanology and Geothermal Research* **156**, 103-115

Caricchi, L., Giordano, D., Burlini, L., Ulmer, P., Romano, C. (2008) Rheological properties of magma from the 1538 eruption of Monte Nuovo (Phlegre Fields, Italy): an experimental study. *Chemical Geology* **256**, 158-171

Carr, M. (1995) Program IgPet. Somerset, NJ: Terra Softa

Chayes, F. (1963) Reletive abundance of intermediate members of the oceanic basalt-trachyte association. *Journal of Geothermal Research* **68**, 1519-1534

Chayes, F. (1977) The oceanic basalt-trachyte relation in general and in the Canary Islands. *American Mineralogist* **62**, 666-671

Civetta, L., Antonio, M., Orsi, G., Tilton, G. R. (1998) The geochemistry of volcanic rocks from Pantelleria island, Siciliy Channel: Petrogenesis and characterisitics of the mantle source region. *Journal of Petrology* **39**, 1453-1491

Civetta, L., Cornette, Y., Crisci, G., Gillot, P. Y., Orsi, G., Requejo, C. S. (1984) Geology, geochronology and chemical evolution of the island of Pantelleria. *Geological Magazine* **121**, 541-668

Cooper, G. F., Wilson, C. J., Millet, M., Baker, J. A., Smith, E. G. (2012) Systematic tapping of independent magma chambers during the 1 Ma Kidnappers super eruption. *Earth and Planetary Science Letters* **313**, 23-33

Costa, A. (2005) Viscosity of high crystal content melts: Dependence on solid fraction. *Geophysical Research Letters* **32**, L22308

Costa, A., Carricchi, L., Bagdassarov, N. S. (2009) A model for the rheology of particle-bearing suspensions and partially molten rocks. *Geochemistry, Geophysics, Geosystems* **10**, 1-13

Courtillot, V., Davaille, A., Besse, J., Stock, J. (2003) Three distinct types of hotspots in the Earth's mantle. *Earth and Planetary Science Letters* **205**, 295-308

Daly, R. A. (1925) The geology of Ascension island. *Proceedings of the American Academy of Arts and Sciences* **60**, 1-80

Davies, G. R., Macdonald, R. (1987) Crustal influences in the petrogenesis of the Naivasha basalt-comendite complex: combined trace element and Sr-Nd-Pb isotope constraints. *Journal of Petrology* **28**, 1009-1031

Deer, W. A., Howie, R. A., Zussman, J. (1966) An introduction to the rock-forming minerals. *Longman Group Limited, London, U.K.*

Di Genova, D., Romano, C., Hess, K. –U., Vona, A., Poe, B. T., Giordano, D., Dingwell, D. B., Behrens, H. (2013) The rheology of peralkaline rhyolites from Pantelleria Island. *Journal of Volcanology and Geothermal Research* **249**, 201-216

Di Matteo, V., Carroll, M. R., Behrens, H., Vetere, F., Brooker, R. A. (2004) Water solubility in trachytic melts. *Chemical Geology* **213**, 187-196

Dingwell, D. B., Bagdassarov, N. S., Bussod, J., Webb, S. L. (1993) Magma rheology. In: Luth, R. W. (Ed.) Short handbook on experiments at high pressure and applications to the Earth's mantle. *Mineralogical Association of Canada, Ontario* **21**, 131-196

Dingwell, D. B., Hess, K. –U., Romano, C. (1998) Extremely fluid behaviour of hydrous peralkaline rhyolites. *Earth and Planetary Science Letters* **158**, 31-38

Dingwell, D. B., Romano, C., Hess, K. U. (1996) The effect of water on the viscosity of a haplogranitic melt under P-T-X conditions relevant to silicic volcanism. *Contributions to Mineralogy and Petrology* **124**, 19-28

Duncan, A. M., Queiroz, G., Guest, J. E., Cole, P. D., Wallenstein, N., Pacheco, J. M. (1999) The Povoação Ignimbrite, Furnas Volcano, São Miguel, Azores. *Journal of Volcanology and Geothermal Research* **92**, 55-65

Eggins, S. M., Woodhead, J. D., Kinsley, L. P. J., Mortimer, G. E., Sylvester, P., McCulloch, M. T., Hergt, J. M., Handler, M. R. (1997) A simple method for the precise determination of ≥ 40 trace elements in geological samples by ICPMS using enriched isotope internal standardisation. *Chemical Geology* **134**, 311-326

Ellis, B. S., Bachmann, O., Wolff, J. A. (2014) Cumulate fragments in silicic ignimbrites: the case of the Snake River Plain. *Geology* **42**, 431-434

Ellis, B. S., Wolff, J. A. (2012) Complex storage of rhyolite in the central Snake River Plain. *Journal of Volcanology and Geothermal Research* **211-212**, 1-11

Ewart, A., Griffin, W. L. (1994) Application of proton-microprobe data to trace element partitioning in volcanic rocks. *Chemical Geolgoy* **117**, 251-284

Ferla, P., Meli, C. (2006) Evidence of magma mixing in the 'Daly Gap' of alkaline suites: a case study from the enclaves of Pantelleria (Italy). *Journal of Petrology* **47**, 1467-1507

Fernandes, R. M. S., Bastos, L., Miranda, J. M., Lourenço, N., Ambrosius, B. A. C., Noomen, R., Simons, W. (2006) Defining the plate boundaries in the Azores region. *Journal of Volcanology and Geothermal Reearch* **156**, 1-9

Gardner, J. E., Rutherford, M., Carey, S., Sigurdsson, H. (1995) Experimental constraints on pre-eruptive water contents and changing magma storage prior to explosive eruptions of Mount St Helens volcano. *Bulletin of Volcanology* **57**, 1-17

Gaspar, J. L. (1996) Ilha Graciosa (Açores). História vulcanológica e avaliação do hazard. Unpublished PhD thesis, Universidade dos Açores

Gaspar, J. L., Guest, J. E., Duncan, A. M., Barriga, F. J. A. S., Chester, D. K. (2015) Volcanic Geology of São Miguel Island (Azores Archipelago). *Geological Society of London Memoirs* **44**, 309 pp

Gaspar, J. L., Queiroz, G., Pacheco, J. M., Ferreira, T., Wallenstein, N., Almeida, M. H., Coutinho, R. (2003) Serreta submarine ridge eruption (Azores). In: White, J. D. L., Smellie, J. L., Clague, D. A. (Eds) Explosive subaqueous volcanism. *American Geophysical Union Geophysical Monograph* **140**, 205-212

Gente, P., Dyment, J., Maia, M., Goslin, J. (2003) Interaction between the Mid-Atlantic Ridge and the Azores hot spot during the last 85 Myr: emplacement and rifting of the hotspot derived plateaus. *Geochemistry, Geophysics, Geosystems* **4**, 8514, doi: 10.1029/2003GC000527

Gertisser, R., Self, S., Gaspar, J. L., Kelley, S. P., Pimentel, A., Eikenberg, J., Barry, T. L., Pacheco, J. M., Queiroz, G., Vespa, M. (2010) Ignimbrite stratigraphy and chronology on Terceira island, Azores. *Geological Society of America Special Paper* **464**, 133-154

Gertisser, R., Self, S., Thomas, L. E., Handley, H. K., Van Calsteren, P., Wolff, J. A. (2012) Processes and timescales of magma genesis and differentiation leading to the Great Tambora eruption in 1815. *Journal of Petrology* **53**, 271-297

Ghiorso, M. S., Sack, R. O. (1995) Chemical mass transfer in magmatic processes IV. A revised and internally consistent thermodynamic model for the interpolation and extrapolation of liquid-solid equilibria in magmatic systems at elevated temperatures and pressures. *Contributions to Mineralogy and Petrology* **119**, 197-212

Gioncada, A., Landi, P. (2010) The pre-eruptive volatile contents of recent basaltic and pantelleritic magmas at Pantelleria (Italy). *Journal of Volcanology and Geothermal Research* **189**, 191-201

Giordano, D., Ardia, P., Romano, C., Dingwell, D. B., Di Muro, A., Schmidt, M W., Mangiacapra, A., Hess, K. U. (2009) The rheological evolution of alkaline Vesuvius magmas and comparison with alkaline series from the Phlegrean Fields, Etna, Stromboli and Teide. *Geochimica et Cosmochimica Acta* **73**, 6613-6630

Giordano, D., Mangiacapra A, Potuzak M, Russell JK, Romano C, Dingwell DB, Di Muro A (2006) An expanded non-Arrhenian model for silicate melt viscosity: A treatment for metaluminous, peraluminous and peralkaline liquids. *Chemical Geology* **229**, 42-56

Giordano, D., Russell, J. K., Dingwell, D. B. (2008) Viscosity of magmatic liquids: A model. *Earth and Planetary Science Letters* **271**, 123-134

Gonnermann, H. M., Manga, M. (2007) The fluid mechanics inside a volcano. *Annual Review of Fluid Mechanics* **39**, 321-356

Gottsmann, J., Dingwell, D. B. (2002) Thermal expansivities of supercooled haplobasaltic liquids. *Geochimica et Cosmochimica Acta* **66**, 2231-2238

Gualda, G. A., Ghiorso, M. S., Lemons, R. V., Carley, T. L. (2012) Rhyolite-MELTS: a modified calibration of MELTS optimized for silica-rich, fluid-bearing magmatic systems. *Journal of Petrology* **53**, 875-890

Hammer, J. E., Rutherford, M. J. (2002) An experimental study of the kinetics of decompression-induced crystallisation in silicic melt. *Journal of Geophysical Research, B: Solid Earth* **107**

Harris, C. (1983) The petrology of lavas and associated plutonic inclusions of Ascension island. *Journal of Petrology* **24**, 424-470

Hildenbrand, A., Weis, D., Madureira, P., Marques, F. O. (2014) Recent plate reorganization at the Azores Triple Junction: Evidence from combined geochemical and geochronological data on Faial, S. Jorge and Terceira volcanic islands. *Lithos* **210-211**, 27-39

Hildreth, W. (1981) Gradients in silicic magma chambers: Implications for lithospheric magmatism. *Journal of Geophysical Research* **86**, 10153-10192

Hildreth, W. (2004) Volcanological perspectives on Long Valley, Mammoth Mountain, and Mono Craters: several contiguous but discrete systems. *Journal of Volcanology and Geothermal Research* **136**, 169-198

Hildreth, W., Wilson, C. J. N. (2007) Compositional zoning of the Bishop Tuff. *Journal of Petrology* **48**, 951-999

Hong, W., Xu, X., Zou, H. (2013) Petrogenesis of coexisting high-silica aluminous and peralkaline rhyolite from Yunshan (Yongtai), southeastern China. *Journal of Asian Earth Science* **74**, 316-329

Huppert, H. E., Sparks, R. S. J. (1984) Double diffusive convection due to crystallisation in magmas. *Annual Review of Earth and Planetary Sciences* **12**, 11-37

Huppert, H. E., Sparks, R. S. J., Wilson, J. R., Hallworth, M. A. (1986) Cooling and crystallisation at an inclined plane. *Earth and Planetary Science Letters* **79**, 319-328

Jaupart, C., Allègre, C. J (1991) Gas content, eruption rate and instabilities of eruption regime in silicic volcanoes. *Earth and Planetary Science Letters* **102**, 413-429

Jeffery, A. J. (2016) Petrogenesis and contrasting eruption styles of peralkaline silicic magmas from Terceira and São Miguel, Azores. Unpublished Ph.D Thesis, Keele University, United Kingdom. Available at: http://eprints.keele.ac.uk/2477/

Jeffery, A. J., Gertisser, R., Jackson, R. A., O'Driscoll, B., Kronz, A. (2016b) On the compositional variability of dalyite, $K_2ZrSi_6O_{15}$: a new occurrence from Terceira, Azores. *Mineralogical Magazine* **80**, 547-565

Jeffery, A. J., Gertisser, R., Whitley, S., Pacheco, J. M., Pimentel, A., O'Driscoll, B., Self, S. (2016a) Temporal evolution of a post-caldera, mildly peralkaline magmatic system: Furnas volcano, São Miguel, Azores. *Contributions to Mineralogy and Petrology* **171**, 42

Kaula, W. M. (1970) Earth's gravity field: relation to global tectonics. *Science* **169**, 982-985

Klügel, A., Hoernle, K. A., Schmincke, H. –U., White, J. D. L. (2000) The chemically zoned 1949 eruption on La Palma (Canary Islands): Petrologic evolution and magma supply dynamics of a rift zone eruption. *Journal of Geophysical Research* **105**, 5997-6016

Kokelaar, B. P. (1986) Magma-water interactions in subaqueous and emergent basaltic volcanism. *Bulletin of Volcanology* **48**, 275-290

Krause, D. C., Watkins, N. D. (1970) North Atlantic crustal genesis in the vicinity of the Azores. *Geophysical Journal of the Royal Astronomical Society* **19**, 261-283

Larsen, L. M. (1979) Distribution of REE and other trace-elements between phenocrysts and peralkaline undersaturated magmas, exemplified by rocks from the Gardar Igneous Province, South Greenland. *Lithos* **12**, 303-315

Lepage, L. D. (2003) ILMAT: an excel worksheet for ilmenite-magnetite geothermometry and geobarometry. *Computers and Geosciences* **29**, 673-678

Lejeune, A., Richet, P. (1995) Rheology of crystal-bearing silicate melts: An experimental study at high viscosity. *Journal of Geophysical Research* **100**, 4215-4229

Llewellin, E. W., Mader, H. M., Wilson, S. D. R. (2002a) The constitutive equation and flow dynamics of bubbly magmas. *Geophysical Research Letters* **29**, 24

Llewellin, E. W., Mader, H. M., Wilson, S. D. R. (2002b) The rheology of a bubbly liquid. *Proceedings of the Royal Society of London A* **458**, 987-1016

Lemarchand, F., Villemant, B., Calas, G. (1987) Trace element distribution coefficients in alkaline series. *Geochimica et Cosmochimica Acta* **51**, 1071-1081

Lourenço, N., Miranda, J. M., Luís, J. F., Ribeiro, A., Victor, L. A. M., Madeira, J., Needham, H. D. (1998) Morpho-tectonic analysis of the Azores Volcanic Plateau from a new bathymetric compilation of the area. *Marine Geophysical Researches* **20**, 141-156

Lowenstern, J. B., Charlier, B. L. A., Clynne, M. A., Wooden, J. L. (2006) Extreme U-Th disequilibrium in rift-related basalts, rhyolites and granophyric granite and the timescales of rhyolite generation, intrusion and crystallization at Alid volcanic center, Eritrea. *Journal of Petrology* **47**, 2105-2122

Luhr, J. F., Carmichael, I. S. E., Varekamp, J. C. (1984) The 1982 eruptions of El Chichón volcano, Chiapas, Mexico: mineralogy and petrology of the anhydrite-bearing pumices. *Journal of Volcanology and Geothermal Research* **23**, 69-108

Luis, J. F., Miranda, J. M. (2008) Reevaluation of magnetic chrons in the North Atlantic between 35˚N and 47˚N: implications for the formation of the Azores Triple Junction and associated plateau. *Journal of Geophysical Research* **113**, B10105

Luis, J. F., Miranda, J. M., Galdeano, A., Patriat, P., Rossignol, J. C., Victor, L. A. M. (1994) The Azores triple junction evolution since 10-Ma from an aeromagnetic survey of the Mid-Atlantic Ridge. *Earth and Planetary Science Letters* **125**, 439-459

Macdonald, R. (1974) Nomenclature and Petrochemistry of the peralkaline oversaturated extrusive rocks. *Bulletin of Volcanology* **38**, 498-505

Macdonald, R. (1987) Quaternary peralkaline silicic rocks and caldera volcanoes of Kenya. In: Fitton, J. G., Upton, B. G. J. (Eds) Alkaline igneous rocks. *Geological Society Special Publication* **30**, 313-333

Macdonald, R. (2012) Evolution of peralkaline silicic complexes: Lessons from the extrusive rocks. *Lithos* **152**, 11-22

Macdonald, R., Belkin, H. E., Fitton, J. G., Rogers, N. W., Nejbert, K., Tindle, A. G., Marshall, A. S. (2008) The roles of fractional crystallisation, magma mixing, crystal mush remobilisation and volatile-melt interactions in the genesis of a young basalt-peralkaline rhyolite suite, the Greater Olkaria Volcanic Complex, Kenya Rift Valley. *Journal of Petrology* **49**, 1515-1547

Macdonald, R., Navarro, J. M., Upton, B. G. J., Davies, G. R. (1994) Strong compositional zonation in peralkaline magma: Menengai, Kenya Rift Valley. *Journal of Volcanology and Geothermal Research* **60**, 301-325

Macdonald, R., Scaillet, B. (2006) The central Kenya peralkaline province: insights into the evolution of peralkaline salic magmas. *Lithos* **91**, 59-73

Madeira, J., Brum da Silveira, A. (2003) Active tectonics and first paleoseismological results in Faial, Pico and S. Jorge islands (Azores, Portugal). *Annals of Geophysics* **46**, 733-761

Madeira, J., Brum da Silveira, A., Hipólito, A., Carmo, R. (2015) Active tectonics in the central and eastern Azores islands along the Eurasia–Nubia boundary: a review. In: Gaspar, J. L., Guest, J. E., Duncan, A. M., Barriga, F. J. A. S., Chester, D. K. (Eds) Volcanic Geology of São Miguel Island (Azores Archipelago). *Geological Society of London Memoirs* **44**, 15-32

Madureira, P., Mata, J., Mattielli, N., Queiroz, G., Silva, P. (2011) Mantle source heterogeneity, magma generation and magmatic evolution at Terceira Island (Azores archipelago): Constraints from elemental and isotopic (Sr, Nd, Hf, and Pb) data. *Lithos* **126**, 402-418

Mahood, G. A. (1984) Pyroclastic rocks and calderas associated with strongly peralkaline magmatism. *Journal of Geophysical Research* **89**, 8540-8552

Mahood, G. A., Hildreth, W. (1986) Geology of the peralkaline volcano at Pantelleria, Strait of Sicily. *Bulletin of Volcanology* **48**, 143-172

Mahood, G. A., Stimac, J. A. (1990) Trace-element partitioning in pantellerites and trachytes. *Geochimica et Cosmochimica Acta* **54**, 2257-2276

Mandeville, C. W., Webster, J. D., Rutherford, M. J., Taylor, B. E., Timbal, A., Faure, K. (2002) Determination of molar absorptivities for infrared absorption bands of H2O in andesitic glasses. *American Mineralogist* **87**, 813-821

Manga, M., Castro, J., Cashman, K. V., Loewenberg, M. (1998) Rheology of bubble-bearing magmas. *Journal of Volcanology and Geothermal Research* **87**, 15-28

Markl, G., Marks, M. A. W., Frost, B. R. (2010) On the controls of oxygen fugacity in the generation and crystallisation of peralkaline melts. *Journal of Petrology* **51**, 1831-1847

Marks, M. A. W., Hettmann, K., Schilling, J., Frost, B. R., Markl, G. (2011) The mineralogical diversity of alkaline igneous rocks: critical factors for the transition from miaskitic to agpaitic phase assemblages. *Journal of Petrology* **52**, 439-455

Marks, M. A. W., Schilling, J., Coulson, I. M., Wenzel, T., Markl, G. (2008) The alkaline-peralkaline Tamazeght complex, High Atlas Mountains, Morocco: mineral chemistry and petrological constraints for derivation from a compositionally heterogeneous mantle source. *Journal of Petrology* **49**, 1097-1131

McBirney, A. R. (1993) Differentiated rocks of the Galapagos hotspot. In: Prichard, H. M., Alabaster, T., Harris, N. B. W., Neary, C. R. (Eds) Magmatic processes and plate tectonics. *Geological Society Special Publication* **76**, 61-69

McKenzie, D., O'Nions, R. K. (1991) Partial melt distributions from inversion of rare earth element concentrations. *Journal of Petrology* **32**, 1021-1091

Métrich, N., Rutherford, M. J. (1992) Experimental study of chlorine behaviour in hydrous silicic melts. *Geochimica et Cosmochimica Acta* **56**, 607-616

Métrich, N., Zanon, V., Créon, L., Hildenbrand, A., Moreira, M., Marques, F. O. (2014) Is the 'Azores Hotspot' a wetspot? Insights from the geochemistry of fluid and melt inclusions in olivine of Pico basalts. *Journal of Petrology* **55**, 377-393

Morimoto, N., Fabries, J., Ferguson, A. K., Ginzburg, I. V., Ross, M., Seifert, F. A., Zussman, J., Aoki, K., Gottardi, G. (1988) Nomenclature of pyroxenes. *Mineralogical Magazine* **52**, 535-550

Mungall, J. E. (1993) Compositional effects of magma mixing and diffusive mass transport on a basalt-pantellerite suite, Terceira, Azores. Unpublished PhD thesis, McGill University, Montreal, Canada

Mungall, J. E., Martin, R. F. (1995) Petrogenesis of basalt-comendite and basalt-pantellerite suites, Terceira, Azores, and some implications for the origin of ocean-island rhyolites. *Contributions to Mineralogy and Petrology* **119**, 43-55

Neave, D. A., Fabbro, G., Herd, R. A., Petrone, C. M., Edmonds, E. (2012) Melting, differentiation and degassing at the Pantelleria volcano, Italy. *Journal of Petrology* **53**, 637-663

Nielsen, R. (1992) BIGD.FOR: A FORTRAN program to calculate trace-element partition coefficients for natural mafic and intermediate composition magmas. *Computers & Geosciences* **18**, 773-788

Nielsen, R. (2006) Geochemical Earth Reference Model (GERM) partition coefficient (Kd) database. Available at: www.earthref.org/KDD/

Pacheco, J. M. (2001) Processos associados ao desenvolvimento de erupções vulcânicas hidromagmáticas explosivas na ilha do Faial e sua interpretação numa perspectiva de avaliação do hazard e minimização do risco. Unpublished PhD thesis, Universidade dos Açores

Papale, P. (1999) Strain-induced magma fragmentation in explosive eruptions. *Nature* **397**, 425-428

Peccerillo, A., Barberio, M. R., Yirgu, G., Ayalew, D., Barbieri, M., Wu, T. W. (2003) Relationships between mafic and peralkaline silicic magmatism in continental rift settings: a petrological, geochemical, and isotopic study of the Gedemsa volcano, central Ethiopian Rift. *Journal of Petrology* **44**, 2002-2032

Peccerillo, A., Donati, C., Santo, A. P., Orlando, A., Yirgu, G., Ayalew, D. (2007) Petrogenesis of silicic peralkaline rocks in the Ethiopian rift: Geochemical evidence and volcanological implications. *Journal of African Earth Sciences* **48**, 161-173

Pimentel, A. (2006) Domos e coulées da ilha Terceira (Açores): contribuição para o estudo dos mecanismos de instalação. Unpublished MSc thesis, Universidade dos Açores

Pimentel, A., Pacheco, J., Self, S. (2015) The ~1000-years BP explosive eruption of Caldeira Volcano (Faial, Azores): the first stage of incremental caldera formation. *Bulletin of Volcanology* **77**, 42

Pimentel, A., Zanon, V., de Groot, L. V., Hipólito, A., Di Chiara, A., Self, S. (2016) Stress-induced comenditic trachyte effusion triggered by trachybasalt intrusion: multidisciplinary study of the AD 1761 eruption at Terceira Island (Azores). *Bulletin of Volcanology* **78**, 22

Pistone, M., Arzilli, F., Dobson, K. J., Cordonnier, B., Reusser, E., Ulmer, P., Marone, F., Whittington, A. G., Mancini, L., Fife, J. L., Blundy, J. D. (2015) Gas-driven filter pressing in magmas: Insights into *in-situ* melt segregation from crystal mushes. *Geology* **43**, 699-702

Putirka, K. D. (2008) Thermometers and barometers for volcanic systems. *Reviews in Mineralogy and Geochemistry* **69**, 61-120

Ren, M., Omenda, P. A., Anthony, E. Y., White, J. C., Macdonald, R., Baily, D. K. (2006) Application of the QUILF thermobarometer to the peralkaline trachytes and pantellerites of the Eburru volcanic complex, East African Rift, Kenya. *Lithos* **91**, 109-124

Ridley, W. I., Watkins, N. D., MacFarlane, D. J. (1974). Chapter 12: The Oceanic Islands: Azores. In: Nairn, A., E., M., Stehli, F., G., (ed.) The Ocean Basins and Margins, Volume 2: The North Atlantic. London: New-York/London: Plenum Press. 445-484

Romengo, N., Landi, P., Rotolo, S. G. (2012) Evidence of basaltic magma intrusions in a trachytic magma chamber at Pantelleria (Italy). *Periodico di Mineralogia* **81,** 1-16

Roux, J., Varet, J. (1975) Alkali feldspar liquid equilibrium relationships in peralkaline oversaturated systems and volcanic rocks. *Contributions to Mineralogy and Petrology* **49**, 67-81

Rubin, A., Cooper, K. M., Leever, M., Wimpenny, J., Deering, C., Rooney, T., Gravley, D., Yin, Q. (2016) Changes in magma storage conditions following caldera collapse at Okataina Volcanic Center, New Zealand. *Contributions to Mineralogy and Petrology* **171**, 4

Scaillet, B., Holtz, F., Pichavant, M. (1998) Phase equilibrium constraints on the viscosity of silicic magmas 1. Volcanic-plutonic comparison. *Journal of Geophysical Research* **103**, 27257-27266

Scaillet, B., Macdonald, R. (2001) Phase relations of peralkaline silicic magmas and petrogenetic implications. *Journal of Petrology* **42**, 825-845

Schilling, J. -G. (1991) Fluxes and excess temperatures of mantle plumes inferred from their interaction with migrating mid-ocean ridges. *Nature* **352**, 397-403

Schwarz, S., Klügel, A., Wohlgemuth, U. C. (2004) Melt extraction pathways and stagnation depths beneath the Madeira and Desertas rift zones (NE Atlantic) inferred from barometric studies. *Contributions to Mineralogy and Petrology* **147**, 228-240

Seaman, S., J., Dyar, M., D., Marinkovic, N. (2009) The effects of heterogeneity in magma water concentration on the development of flow banding and spherulites in rhyolitic lava. *Journal of Volcanology and Geothermal Research* **183**, 157-169

Searle, R. (1980) Tectonic pattern of the Azores spreading centre and triple junction. *Earth and Planetary Science Letters* **51**, 415-434

Self, S. (1971) The Lajes Ignimbrite, Ilha Terceira, Açores. *Comunicações dos Serviços Geólogicos de Portugal* **55**, 165-184

Self, S. (1974) Recent volcanism on Terceira, Azores. Unpublished PhD thesis, Imperial College London

Self, S. (1976) The recent volcanology of Terceira, Azores. *Journal of the Geological Society of London* **132**, 645-666

Self, S., Gunn, B. M. (1976) Petrology, volume and age relations of alkaline and saturated peralkaline volcanics from Terceira, Azores. *Contributions to Mineralogy and Petrology* **54**, 293-313

Shane, P., Nairn, I. A., Smith, V. C., Darragh, M., Beggs, K., Cole, J. W. (2008) Silicic recharge of multiple rhyolite magmas by basaltic intrusion during the 22.6 ka Okareka eruption episode, New Zealand. *Lithos* **103**, 527-549

Shaw, H. R. (1972) Viscosities of magmatic silicate liquids – empirical method of prediction. *American Journal of Science* **272**, 870

Shao, F., Niu, Y., Regelous, M., Zhu, D-C. (2015) Petrogenesis of peralkaline rhyolites in an intra-plate setting: Glass House Mountains, southeast Queensland, Australia. *Lithos* **216-217**, 196-210

Silveira, G., Stutzmann, E., Davaille, A., Montagner, J. -P., Mendes-Victor, L., Sebai, A. (2006) Azores hotspot signature in the upper mantle. *Journal of Volcanology and Geothermal Research* **156**, 23-34

Sisson, T. W., Bacon, C. R. (1999) Gas-driven filter pressing in magmas. *Geology* **27**, 613-616

Sparks, R. S. J. (1978) The dynamics of bubble formation and growth in magmas: a review and analysis. *Journal of Volcanology and Geothermal Research* **3**, 1-37

Sparks, R. S. J., Pinkerton, H. (1978) Effects of degassing on rheology of basaltic lava. *Nature* **276**, 385-386

Storey, M., Wolff, J. A., Norry, M. J., Marriner, G. F. (1989) Origin of hybrid lavas from Agua de Pau volcano, São Miguel, Azores. *Geological Society of London Special Publications* **42**, 161-180

Stormer Jr, J. C. (1983) The effects of recalculation on estimates and oxygen fugacity from analyses of multi-component iron-titanium oxides. *American Mineralogist* **68**, 586-594

Sumner, J. M., Wolff, J. (2003) Petrogenesis of mixed-magma, high-grade, peralkaline ignimbrite 'TL' (Gran Canaria): diverse styles of mixing in a replenished, zoned magma chamber. *Journal of Volcanology and Geothermal Research* **126**, 109-126

Tait, S. R., Wörner, G., Van Den Bogaard, P., Schmincke, H. –U. (1989) Cumulate nodules as evidence for convective fractionation in a phonolite magma chamber. *Journal of Volcanology and Geothermal Research* **37**, 21-37

Thompson, R. N. (1974) Some high-pressure clinopyroxenes. *Mineralogical Magazine* **39**, 768-787

Tolstoy, I. (1951) Submarine topography in the North Atlantic. *Bulletin of the Geological Society of America* **62**, 441-450

Tomlinson, E. L., Smith, V. C., Albert, P. G., Aydar, E., Civetta, L., Cioni, R., Çubukçu, E., Gertisser, R., Isaia, R., Menzies, M. A., Orsi, G., Rosi, M., Zanchetta, G. (2015) The major and trace element glass compositions of the productive Mediterranean volcanic sources: tools for correlating distal tephra layers in and around Europe. *Quaternary Science Reviews* **118**, 48-66

Troll, V. R., Schmincke, H. –U. (2002) Magma mixing and crustal recycling recorded in ternary feldspar from compositionally zoned peralkaline ignimbrite 'A', Gran Canaria, Canary Islands. *Journal of Petrology* **43**, 243-270

Trua, T., Deniel, C., Mazzuoli, R. (1999) Crustal control in the genesis of Plio-Quaternary bimodal magmatism of the Main Ethiopian Rift (MER): geochemical and isotopic (Sr, Nd, Pb) evidence. *Chemical Geology* **155**, 201-231

Turbeville, B. N. (1993) Sidewall differentiation in an alkalic magma chamber: evidence from syenite xenoliths in tuffs of the Latera caldera, Italy. *Geological Magazine* **130**, 453-470

Venezky, D. Y., Rutherford, M. J. (1999) Petrology and Fe-Ti oxide reequilibration of the 1991 Mount Unzen mixed magma. *Journal of Volcanology and Geothermal Research* **89**, 213-230

Villemant, B. (1988) Trace element evolution in the Phlegrean Fields (Central Italy): fractional crystallization and selective enrichment. *Contributions to Mineralogy and Petrology* **98**, 169-183

Villemant, B., Jaffrezic, H., Joron, J. –L., Treuil, M. (1981) Distribution coefficients of major and trace elements; fractional crystallization in the alkali basalt series of Chaîne des Puys (Massif Central, France). *Geochimica et Cosmochimica Acta* **45**, 1997-2016

Vona, A., Romano, C., Dingwell, D. B., Giordano, D. (2011) The rheology of crystal-bearing basaltic magmas from Stromboli and Etna. *Geochimica et Cosmochimica Acta* **75**, 3214-3236

Vogt, P. R., Jung, W. Y. (2004) The Terceira Rift as hyper-slow, hotspot-dominated oblique speeding axis: a comparison with other slow-spreading plate boundaries. *Earth and Planetary Science Letters* **218**, 77-90

Vona, A., Romano, C., Dingwell, D. B., Giordano, D. (2011) The rheology of crystal-bearing basaltic magmas from Stromboli and Etna. *Geochimica et Cosmochimica Acta* **75**, 3214-3236

Watson, E. B., Green, T. H. (1981) Apatite/liquid partition coefficients for the rare earth elements and strontium. *Earth and Planetary Science Letters* **56**, 405-421

Weaver, J. D. (1977) The Quaternary caldera volcano Emuruangogolak, Kenya Rift, and the petrology of a bimodal ferrobasalt-pantelleritic trachyte association. *Bulletin Volcanologique* **40**, 209-230

Widom, E., Gill, J. B., Schmincke, H. –U. (1993) Syenite nodules as a long-term record of magmatic activity in Agua de Pau Volcano, São Miguel, Azores. *Journal of Petrology* **34**, 929-953

Williams, R., Branney, M. J., Barry, T. L. (2013) Temporal and spatial evolution of a waxing then waning catastrophic density current revealed by chemical mapping. *Geology* **42**, 107-110

White, J. C., Benker, S. C., Ren, M., Urbanczyk, K. M., Corrick, D. W. (2006) Petrogenesis and tectonic setting of the peralkaline Pine Canyon caldera, Trans-Pecos Texas, USA. *Lithos* **91**, 74-94

White, J. C., Holt, G. S., Parker, D. F., Ren, M. (2003) Trace-element partitioning between alkali feldspar and peralkalic quartz trachyte to rhyolite magma. Part I: systematics of trace element partitioning. *American Mineralogist* **88**,316-329

White, J. C., Parker, D. F., Ren, M. (2009) The origin of trachyte and pantellerite from Pantelleria, Italy: Insights from major element, trace element, and thermodynamic modelling. *Journal of Volcanology and Geothermal Research* **179**, 33-55

White, W. M., Schilling, J. -G., Hart, S. R. (1976) Evidence for the Azores mantle plume from strontium isotope geochemistry of the central North Atlantic. *Nature* **263**, 659-663

White, W. M., Tapia, M. D. M., Schilling, J. –G. (1979) The petrology and geochemistry of the Azores islands. *Contributions to Mineralogy and Petrology* **69**, 201-213

Widom, E., Shirey, S. B. (1996) Os isotope systematics in the Azores: implications for mantle plume sources. *Earth and Planetary Science Letters* **142**, 451-465

Wood, B. J., Trigila, R. (2001) Experimental determination of aluminous clinopyroxene-melt partition coefficients for potassic liquids, with application to the evolution of the Roman province potassic magmas. *Chemical Geology* **172**, 213-223

Woods, A. W., Koyaguchi, T. (1994) Transitions between explosive and effusive eruptions of silicic magmas. *Nature* **370**, 641-644

Zack, T., Brumm, R. (1998) Ilmenite/liquid partition coefficients of 26 trace elements determined through ilmenite/clinopyroxene partitioning in garnet pyroxenites. *Seventh International Kimberlite Conference, Cape Town*

Zanon, V., Frezzotti, M. L. (2013) Magma storage and ascent conditions beneath Pico and Faial islands (Azores islands): a study on fluid inclusions. *Geochemistry, Geophysics, Geosystems* **14**, 3494-3514

Zanon, V., Keuppers, U., Pacheco, J. M., Cruz, I. (2013) Volcanism from fissure zones and central volcanoes: geochemical processes in multiple feeding systems. The case study of Faial Island- Azores archipelago. *Geological Magazine* **150**, 536-555

Zanon, V., Pimentel, A. (2015) Spatio-temporal constraints on magma storage and ascent conditions in a transtensional tectonic setting: the case of the Terceira island (Azores). *American Mineralogist* **100**, 795-805

Zbyszewski, G. (1966) As observações de F. Fouqué sobre o vulcanismo dos Açores. *Boletim do Núcleo Cultural da Horta* **4**, 17-95

FIGURE CAPTIONS

Figure 1 (a) Map showing the Central and Eastern Groups of the Azores archipelago in relation to key structural features. Inset: Map highlighting the location of the Azores archipelago in the central Atlantic Ocean **(b)** Map of Terceira island showing the volcanic centres and major infrastructure. Contours (20 m intervals) generated using GeoMapApp©. The fissure zone which bisects the island from NW to SE is shown as a dashed line.

Figure 2 Summarised ignimbrite stratigraphy and ignimbrite distribution maps for Terceira, after Gertisser *et al*. (2010). White diamond symbols indicate sampling locations for each ignimbrite formation. Full details on each location, including field photographs are given in

Jeffery (2016). Unnamed portions of the stratigraphy comprise various basaltic to trachytic or rhyolitic lava flows and pyroclastic deposits

Figure 3 Representative photomicrographs of mineral phases from ignimbrites of Terceira **(a)** Large, euhedral alkali feldspar crystal surrounded by vesicular glass (LAI) **(b)** Highly resorbed and embayed alkali feldspar crystal surrounded by vesicular glass (LMI) **(c)** Large euhedral diopside crystal surrounded by vesicular glass (PNI) **(d)** Small augite crystal with associated Fe-Ti oxide crystals (LAI) **(e)** Strongly resorbed and embayed olivine crystal (LAI) **(f)** Euhedral biotite crystal with small acicular apatite inclusions (GVI) **(g)** Small zoned Fe-Ti oxide crystals (Ign-i) **(h)** Alkali feldspar-dominated syenite bleb surrounded by vesicular glass (LAI). An alkali feldspar phenocryst is visible in the top left of the image

Figure 4 Representative hand specimen photographs of syenitic autoliths from CCI **(a)** Coarse- and medium-grained varieties of syenite **(b)** Schlieren structures, comprising abundant Na-clinopyroxene, Na-amphibole, and aenigmatite, within syenite autoliths. The surrounding syenite often exhibits contrasting grain sizes or model mineralogies on either side of the structure **(c)** Trachytic enclaves within a large block of syenite. Individual enclaves exhibit rounded, lobate boundaries, with distinctive chilled margins, and contain numerous miarolitic cavities

Figure 5 Representative photomicrographs of syenitic autoliths and syenite-hosted enclaves. Abbreviations used: Di = diopside; Aeg = aegirine, Agt = aegirine-augite; Na-Ca Amp = Na-Ca amphibole, Na-Amp = Na amphibole; Aen = aenigmatite, Afs = alkali feldspar, Mg-Ol =

Mg-rich olivine **(a)** Course-grained syenite comprising large interlocking alkali feldspar crystals. A small dalyite crystal and acicular aegirine crystals are visible, partially filling an interstitial void space in the lower right; **(b)** Medium-grained syenite comprising predominantly alkali feldspar laths with small intercumulus Na-amphiboles and aegirine; **(c)** Large irregularly zoned aegirine-augite crystal occupying an intercumulus void space, surrounded by alkali feldspar. A highly irregular core of Na-amphibole is visible within the aegirine-augite crystal; **(d)** An intercumulus amphibole crystal surrounded by alkali feldspar. The amphibole exhibits an optically distinguishable compositional transition from Na-Ca amphibole (centre), to Na- amphibole (darker rims), and finally aegirine (upper and lower margins); **(e)** Complex intercumulus void, sounded by alkali feldspar (lower right), filled with quartz (upper central image), aenigmatite and aegirine. The aegirine comprises a mush of acicular crystals which appear to be replace a large, irregular aenigmatite crystal; **(f)** Syenite-hosted enclave comprising large diopside and Na-Ca amphibole crystals set in a microcrystalline groundmass of alkali feldspar, aegirine-augite, Na-Ca amphibole, and Fe-Ti oxides; **(g)** Characteristically large alkali feldspar crystal from a syenite-hosted enclave. A pronounced, inclusion-rich rim is visible at its margins; **(h)** Mg-rich olivine double breakdown texture from a syenite-hosted enclave. The outer rim comprises a hydrous iddingsitic assemblage, whilst the interior represents an anhydrous breakdown assemblage which includes Fe-Ti oxides

Figure 6 Geochemical classification plots for Terceira. Data sourced from Self (1974), Mungall (1993), Gertisser *et al.* (2010), Madureira *et al.* (2011), Tomlinson *et al.* (2015), and Jeffery *et al.* (2016a). **(a)** Chemical compositions of various Terceira lithologies plotted on the total alkali-silica (TAS) diagram of Le Bas *et al.* (1986). Whole-rock, melt inclusion, and groundmass glass data are not distinguished. Errors (2σ) do not exceed symbol size; **(b)**

Enlargement of Fig. 6a, showing the compositions of the ignimbrite formations, Caldeira-Castelinho Ignimbrite Formation (CCI) syenite autoliths and CCI syenite autolith-hosted enclaves. Symbols are as in Fig. 6a. Whole-rock data are shown using the same colours and symbols as in Figure 6a. The lighter variants of the same colours depict groundmass glass analyses. The darker variants indicate melt inclusion analyses (e.g. the green triangles mark whole-rock analyses of the VFI, as in Fig. 6a, whilst the light green and dark green triangles reflect groundmass glass and melt inclusion analyses, respectively). The 2σ error for melt inclusion and groundmass glass data is shown in the top right. Errors for whole-rock do not exceed symbol size; **(c)** Peralkaline compositions for Terceira plotted on the FeO_t vs. Al_2O_3 classification scheme for oversaturated peralkaline rocks (Macdonald, 1974). Symbols are as in Fig. 6a. Errors (2σ) do not exceed symbol size

Figure 7 Major and trace element compositional data for Terceira plotted *versus* MgO. The grey dashed line represents the most successful Rhyolite-MELTS model (polybaric fractional crystallisation with a transition from 500 MPa to 150 MPa set to occur at 1,100 °C, fO_2 = FMQ -1, initial water content = 1.5 wt %). The transition from 500 to 150 MPa is marked with a vertical dashed black line at 2.76 wt % MgO on each plot. The crystallisation intervals for each of the predicted mineral phases are marked on the lower-right plot. For clarity, data for Cinco Picos and Santa Bárbara are not shown. All data sourced from Self (1974), Mungall (1993), Gertisser *et al.* (2010), Madureira *et al.* (2011), Tomlinson *et al.* (2015) and Jeffery *et al.* (2016a). All major element oxides reported in wt %, trace elements as ppm. Errors (2σ) do not exceed symbol size. Abbreviations used: Ol = olivine; Cpx = clinopyroxene; Fsp = feldspar; Ti-Mag = Ti-magnetite; Ilm = ilmenite; Ap = apatite

Figure 8 Trace element variation diagrams for Terceira lithologies. Chondritic and primitive mantle values taken from Sun & McDonough (1989). **(a)** Chondrite-normalised REE patterns for the ignimbrite formations. Grey field indicates the range of literature values for the four youngest ignimbrite formations (LAI, LMI, VFI, CCI) from Tomlinson *et al*. (2015). **(b)** Chondrite-normalised REE patterns for the CCI syenite autoliths. Data from Jeffery *et al*. (2016a). Grey field indicates the range of literature values for syenitic xenoliths taken from Mungall (1993). **(c)** Chondrite-normalised REE patterns for the CCI syenite-hosted enclaves. Grey field indicates range of literature values for the four youngest ignimbrite formations (LAI, LMI, VFI, CCI) from Tomlinson *et al*. (2015). **(d)** Multi-element trace element patterns for the ignimbrite formations. **(e)** Multi-element trace element patterns for the CCI syenite autoliths. Data from Jeffery *et al*. (2016a). **(f)** Multi-element trace element patterns for the CCI syenite-hosted enclaves

Figure 9 Mineral compositions of the ignimbrite formations, CCI syenite autoliths, and syenite-hosted enclaves. Analyses from the groundmass of the enclaves are labelled as 'Enclave gm', whereas the enclave phenocrysts are marked 'Enclave pheno'. **(a)** Alkali feldspar compositions plotted into the ternary An-Ab-Or system. (**b)** Clinopyroxene compositions plotted into the pyroxene quadrilateral and, where relevant, the ternary Qd-Jd-Aeg system (Morimoto *et al*., 1988) and the ternary Di-Hd-Aeg system. (**c)** Fe-Ti oxide compositions plotted into the TiO_2-FeO-Fe_2O_3 ternary system. (**d)** Biotite compositions of the GVI (Deer *et al*., 1966). (**e)** Ca-amphibole compositions for the syenite-hosted enclaves, plotted using the scheme of Leake *et al*. (1997). **(f)** Ca-Na-amphibole compositions for the CCI syenites and syenite-hosted enclaves, plotted using the scheme of Leake *et al*. (1997). **(g)** Na-amphibole compositions for the CCI syenites, plotted using the scheme of Leake *et al*. (1997).

Figure 10 Summarised results of thermometry and hygrometry using the ILMAT program of Lepage (2003) for two-oxide thermometry, the alkali feldspar-melt thermometer of Putirka (2008) and the feldspar-melt hygrometer of Mollo *et al*. (2015). A full discussion of each method is given in the text **(a)** T-fO_2 estimates for the LAI and the CCI syenite autoliths derived from two-oxide models. FMQ buffer reaction curve calculated for 100 MPa. **(b)** T-H_2O_{melt} estimates for the ignimbrite formations, the CCI syenite autoliths, and the syenite-hosted enclaves, derived from alkali feldspar-melt thermo-hygrometry. The standard error of the estimate for both temperature and water content is shown in the top right corner.

Figure 11 Halogen compositions of melt inclusions from each of the ignimbrite formations of Terceira plotted against Peralkalinity Index. Errors (2σ) do not exceed the symbol size

Figure 12 Variations in TiO_2 (a)and Al_2O_3 (b) contents of clinopyroxene *versus* En mol. % in relation to the depth of crystallisation (cf. Beier *et al.*, 2006; Jeffery *et al*., 2016a)

Figure 13 Results of Rayleigh fractionation and batch melting trace element modelling. The calculated Rayleigh fractionation curve is labelled RalFC. Batch melting models were calculated for hypothetical gabbroic, syenodioritic, and syenitic lithologies. Each field comprises the total area occupied by four individual batch melting curves, each curve generated by varying the original mineral proportions of the parental material. For example, the gabbro melting field indicates the area occupied by four separate batch melting curves, each produced by altering the relative proportions of plagioclase, clinopyroxene, and olivine.

Figure 14 Conceptual model for the magma plumbing system of Pico Alto volcano, comprising a prominent magma storage zone in the shallow crust. Abbreviations used: Byt = bytownite, Di = diopside, Mg-Ol = Mg-rich olivine, Anorth = anorthoclase, Olig = oligoclase, Aug = augite **(a)** Ascending hawaiites (phase assemblage = Byt + Di + Mg-Ol) are mixed with trachytes (phase assemblage = Anorth), forming hybridised intermediate to silicic magmas (phase assemblage = Olig + Aug + Anorth + Byt + Di + Mg-Ol). **(b)** Injection of hybridised trachyte into peralkaline trachyte in the uppermost portion of the shallow crustal storage zone, passing through a marginal syenitic crystal mush and forming enclaves therein. Replenishment initiates further mixing and introduces antecrysts to the eruptible portion of the reservoir. **(c)** Efficient crystal settling in the uppermost eruptible cap of peralkaline trachyte generates crystal poor magma and chemical zoning

Figure 15 Results of rheological modelling aiming to simulate the effects of degassing and microlite crystallisation upon the viscosity of the peralkaline trachytic magmas of this study during ascent. **(a)** Isothermal magma viscosities calculated for each of the ignimbrite-forming peralkaline trachytes using the model of Giordano *et al*. (2008) and the melt to magma viscosity conversion of Dingwell *et al*. (1993). Magma water contents were varied from 0 to 6 wt % and crystal fraction was set to 0.2 (see text for full details). Each of the curves was calculated using a composition from one of the peralkaline ignimbrite formations of this study **(b)** Bubble-free, crystal bearing magma viscosities for the peralkaline trachytes of this study, calculated using the model of Vona *et al.* (2011). Models were run for the minimum and maximum pre-eruptive melt viscosity estimates determined in this study ($10^{3.1}$ to $10^{4.3}$ Pa s,

respectively), using a variable crystal fraction (0.0 to 0.4) and a mean crystal aspect ratio of 7 (see text for details)

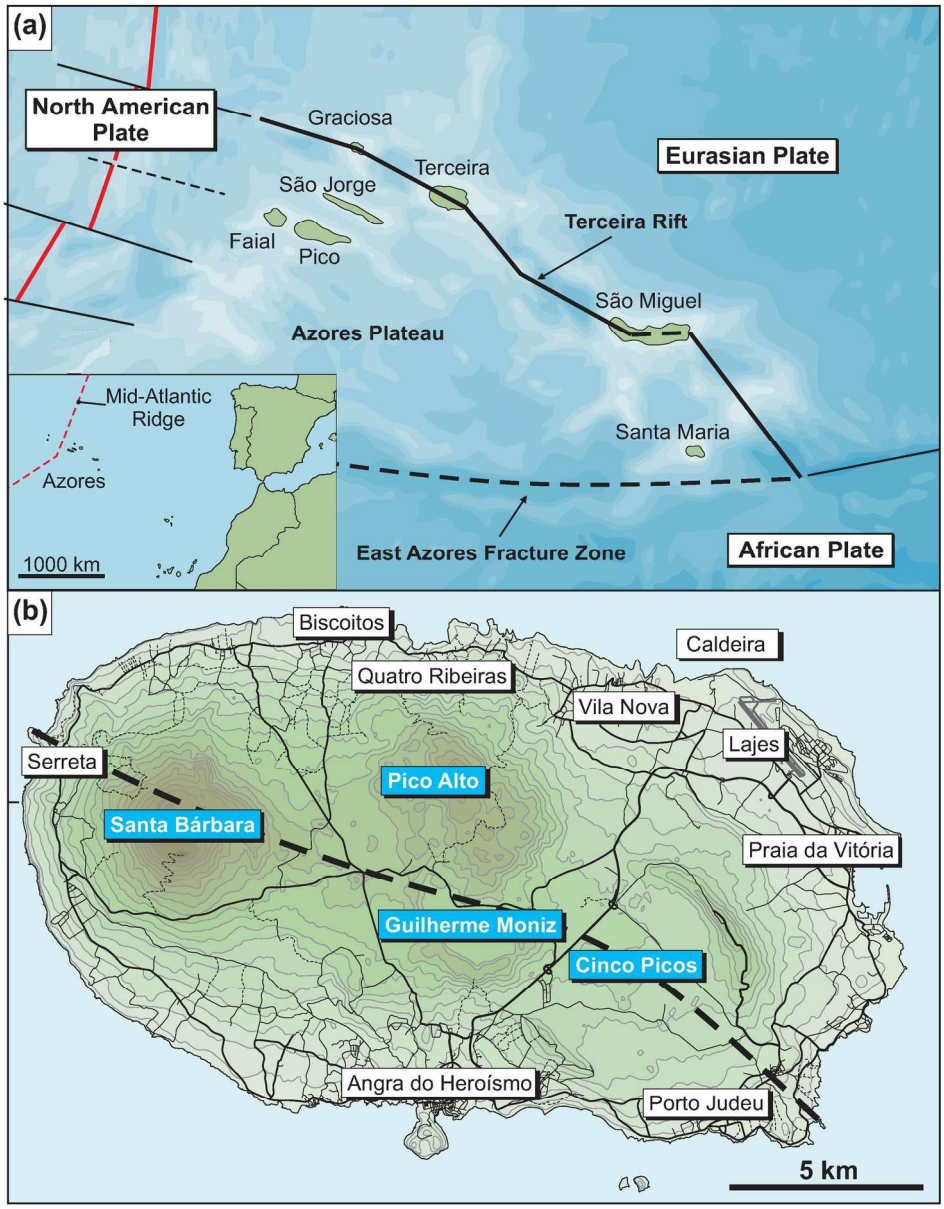

Figure 1 (a) Map showing the Central and Eastern Groups of the Azores archipelago in relation to key structural features. Inset: Map highlighting the location of the Azores archipelago in the central Atlantic Ocean (b) Map of Terceira island showing the volcanic centres and major infrastructure. Contours (20 m intervals) generated using GeoMapApp©. The fissure zone which bisects the island from NW to SE is shown as a dashed line.

159x203mm (300 x 300 DPI)

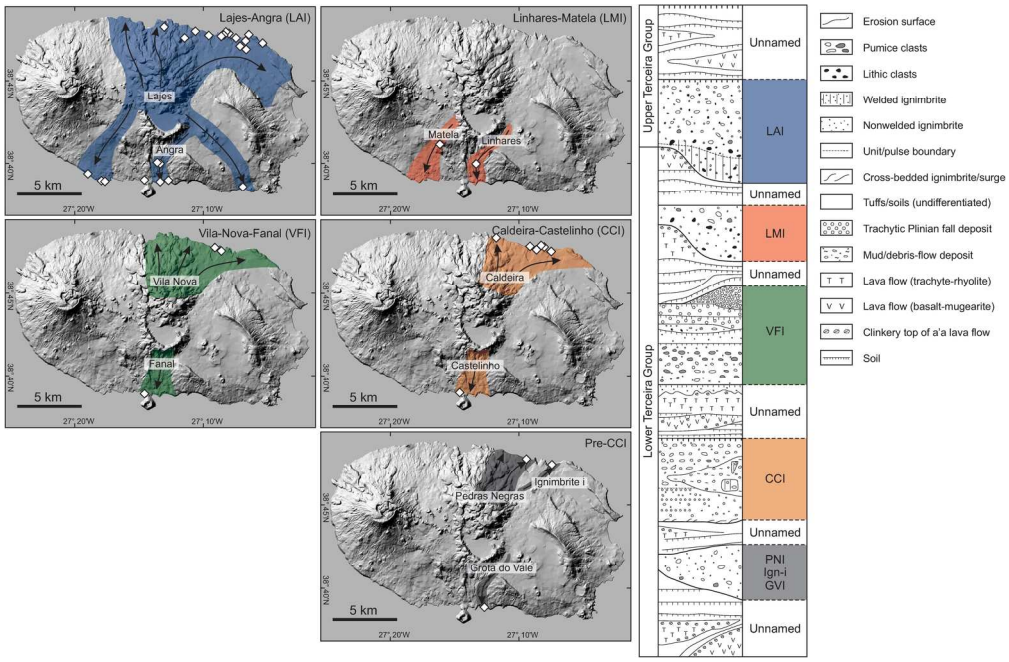

Figure 2 Summarised ignimbrite stratigraphy and ignimbrite distribution maps of Terceira, after Gertisser et al. (2010). White diamond symbols indicate sampling locations for each ignimbrite formation. Full details on each location, including field photographs are given in Jeffery (2016). Unnamed portions of the stratigraphy comprise various basaltic to trachytic/rhyolitic lava flows and pyroclastic deposits

179x117mm (300 x 300 DPI)

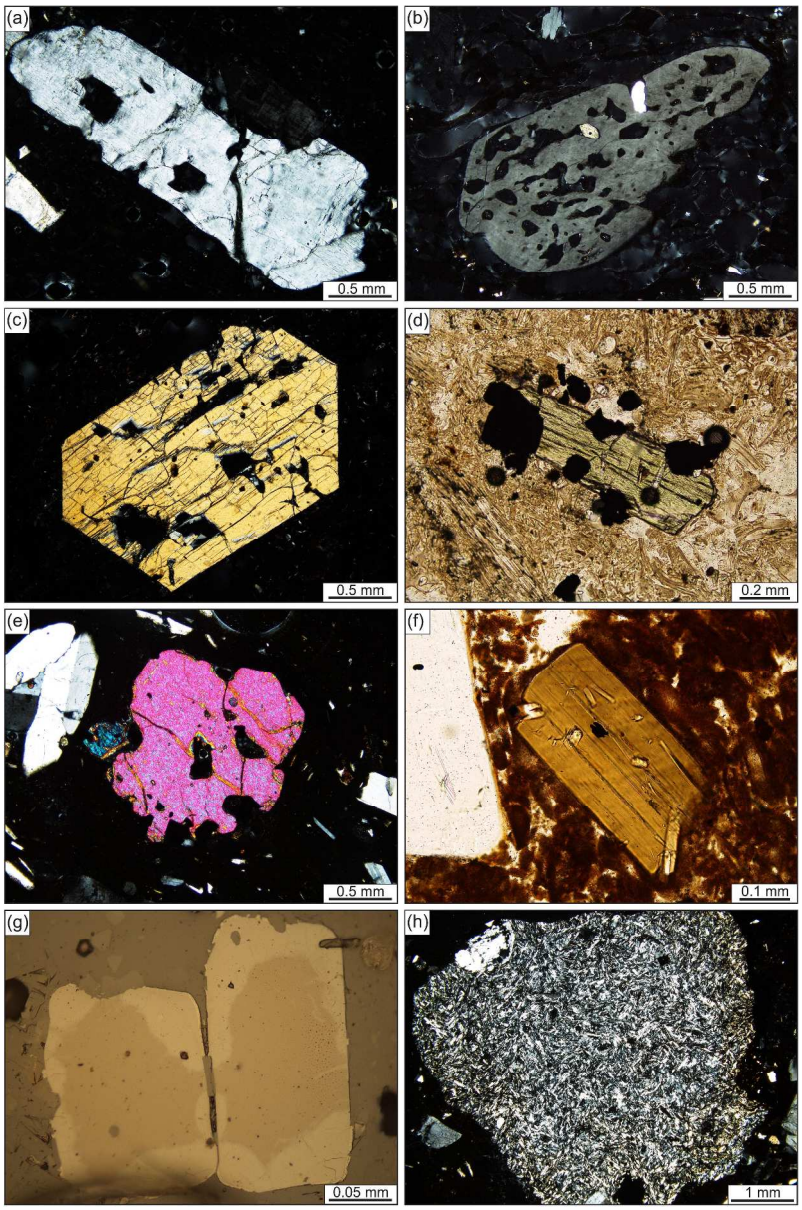

Figure 3 Representative photomicrographs of mineral phases from ignimbrites of Terceira (a) Large, euhedral alkali feldspar crystal surrounded by vesicular glass (LAI) (b) Highly resorbed and embayed alkali feldspar crystal surrounded by vesicular glass (LMI) (c) Large euhedral diopside crystal surrounded by vesicular glass (PNI) (d) Small augite crystal with associated Fe-Ti oxide crystals (LAI) (e) Strongly resorbed and embayed olivine crystal (LAI) (f) Euhedral biotite crystal with small acicular apatite inclusions (GVI) (g) Small zoned Fe-Ti oxide crystals (Ign-i) (h) Alkali feldspar-dominated syenite bleb surrounded by vesicular glass (LAI). An alkali feldspar phenocryst is visible in the top left of the image

263x398mm (300 x 300 DPI)

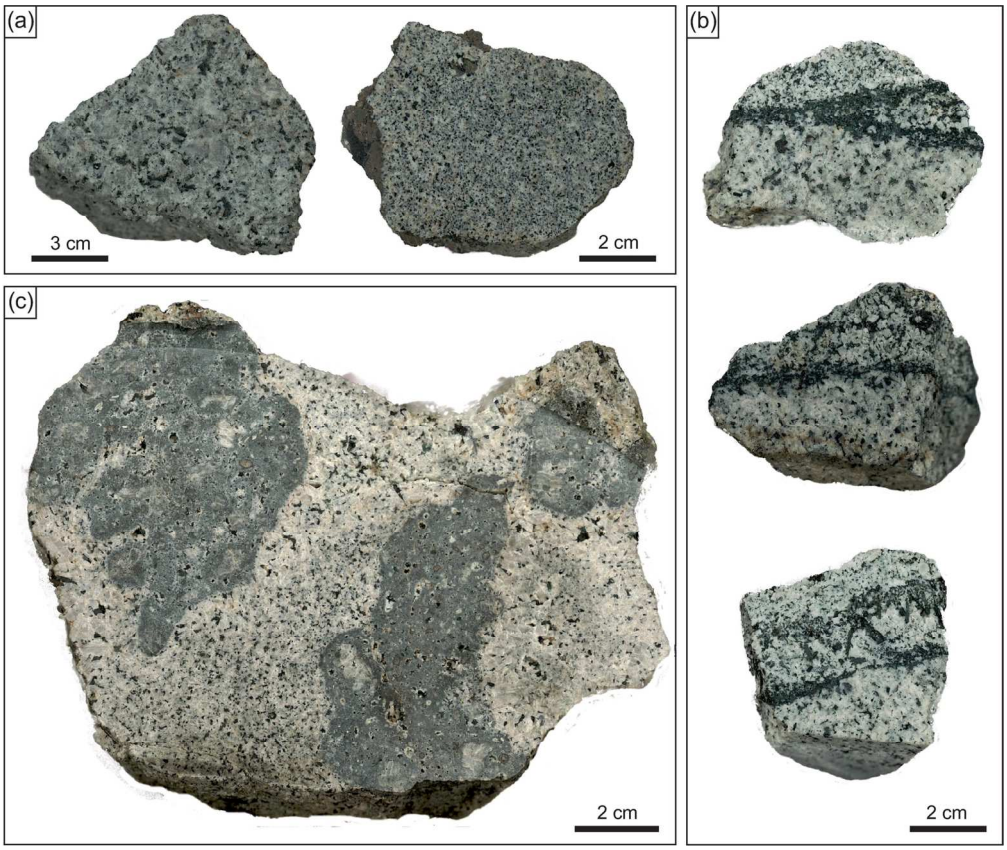

Figure 4 Representative hand specimen photographs of syenitic autoliths from CCI (a) Coarse- and medium-grained varieties of syenite (b) Schlieren structures, comprising abundant Na-clinopyroxene, Na-amphibole, and aenigmatite, within syenite autoliths. The surrounding syenite often exhibits contrasting grain sizes or model mineralogies on either side of the structure (c) Trachytic enclaves within a large block of syenite. Individual enclaves exhibit rounded, lobate boundaries, with distinctive chilled margins, and bear numerous miarolitic cavities

146x123mm (300 x 300 DPI)

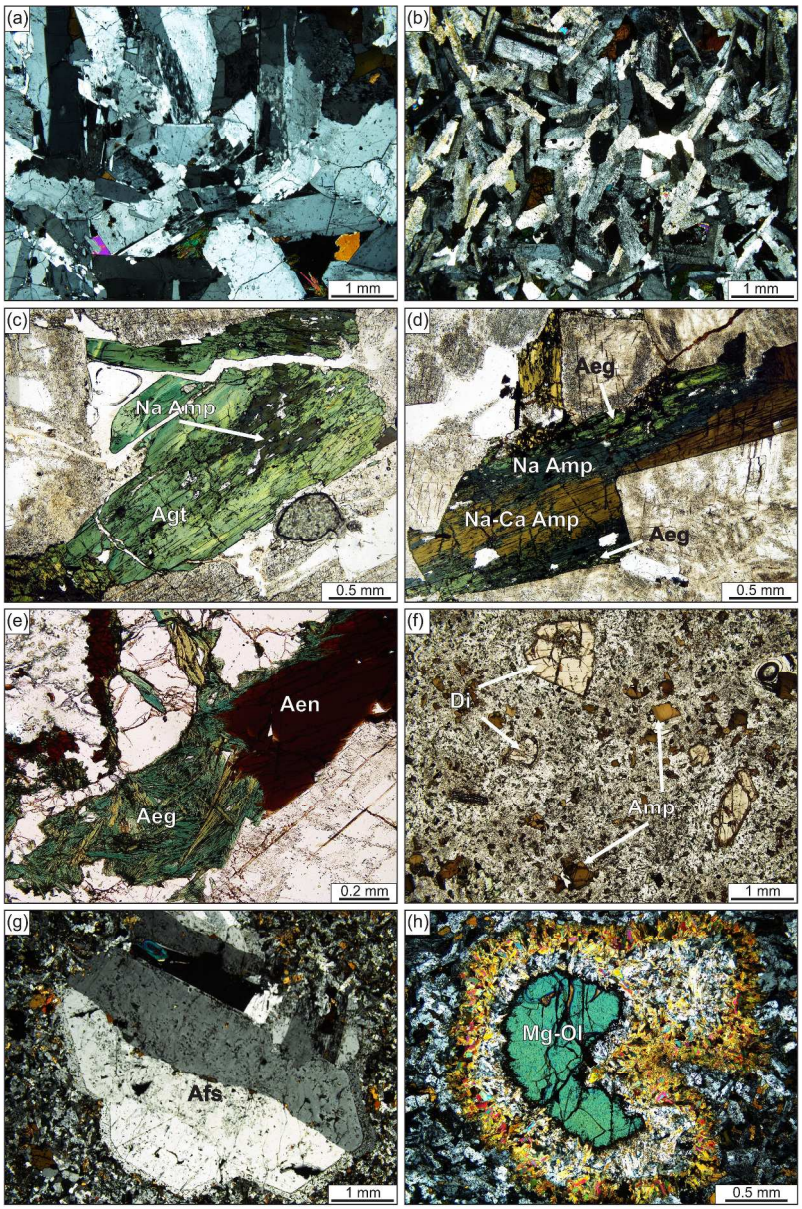

Figure 5 Representative photomicrographs of syenitic autoliths and syenite-hosted enclaves. Abbreviations used: Di = diopside; Aeg = aegirine, Agt = aegirine-augite; Na-Ca Amp = Na-Ca amphibole, Na-Amp = Na amphibole; Aen = aenigmatite, Afs = alkali feldspar, Mg-Ol = Mg-rich olivine (a) Course-grained syenite comprising large interlocking alkali feldspar crystals. A small dalyite crystal and acicular aegirine crystals are visible, partially filling an interstitial void space in the lower right (b) Medium-grained syenite comprising predominantly alkali feldspar laths with small intercumulus Na-amphiboles and aegirine (c) Large irregularly zoned aegirine-augite crystal occupying an intercumulus void space, surrounded by alkali feldspar. A highly irregular core of Na-amphibole is visible within the aegirine-augite crystal (d) An intercumulus amphibole crystal surrounded by alkali feldspar. The amphibole exhibits an optically distinguishable compositional transition from Na-Ca amphibole (central), to Na- amphibole (darker rims), and finally aegirine (upper and lower margins) (e) Complex intercumulus void, sounded by alkali feldspar (lower right image), filled with quartz (upper central image), aenigmatite and aegirine. The aegirine comprises a mush of acicular crystals which appear to be replace a large, irregular aenigmatite crystal (f) Syenite-hosted enclave comprising large

diopside and Na-Ca amphibole crystals set in a microcrystalline groundmass of alkali feldspar, aegirine-augite, Na-Ca amphibole, and Fe-Ti oxides (g) Characteristically large alkali feldspar crystal from the syenite-hosted enclaves. A pronounced, inclusion-rich rim is visible at its margins (h) Mg-rich olivine double breakdown texture from the syenite-hosted enclaves. The outer rim comprises a hydrous iddingsitic assemblage, whilst the interior represents an anhydrous breakdown assemblage which includes Fe-Ti oxides

263x398mm (300 x 300 DPI)

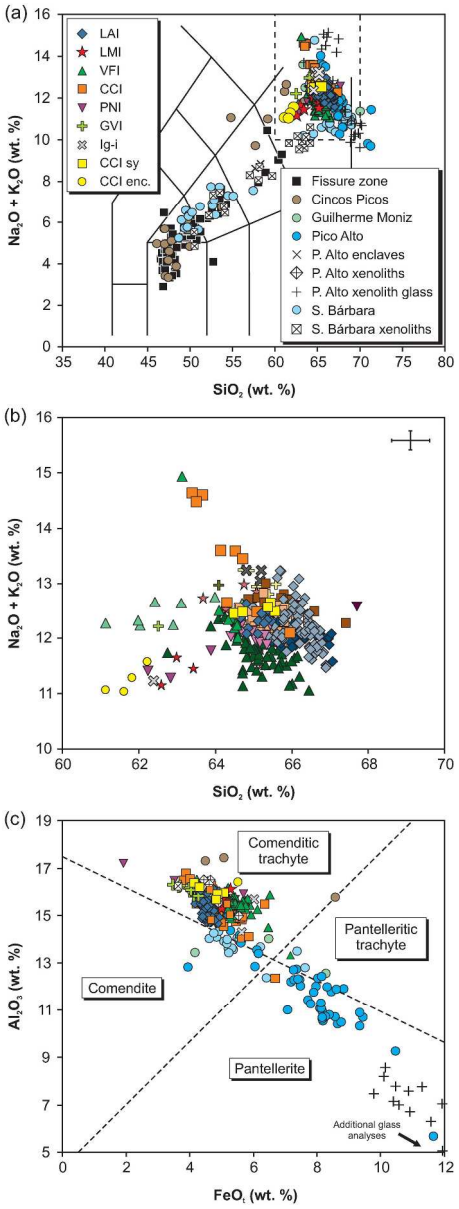

Figure 6 Geochemical classification plots for Terceira. Data sourced from Self (1974), Mungall (1993), Gertisser et al. (2010), Madureira et al. (2011), Tomlinson et al. (2015), and Jeffery et al. (2016a). (a) Chemical compositions of various Terceira lithologies plotted into the total alkali-silica (TAS) diagram of Le Bas et al. (1986). Whole-rock, melt inclusion, and groundmass glass data are not distinguished. Errors (2σ) do not exceed symbol size (b) Blow up of Figure 6a, showing the compositions of the ignimbrite formations, Caldeira-Castelinho Ignimbrite Formation (CCI) syenite autoliths, and CCI syenite autolith-hosted enclaves. Symbols are as in Figure 6a. Whole-rock data are shown using the same colours and symbols as in Figure 6a. The lighter variants of the same colours depict groundmass glass analyses. The darker variants indicate melt inclusion analyses (e.g. the green triangles mark whole rock analyses of the VFI, as in Figure 6a, whilst the light green and dark green triangles reflect groundmass glass and melt inclusion analyses, respectively). The 2σ error for melt inclusion and groundmass glass data is shown in the top right. Errors for whole-rock do not exceed symbol size (c) Peralkaline compositions of Terceira plotted into the FeOt vs. Al2O3 classification scheme for oversaturated peralkaline rocks (Macdonald, 1974). Symbols are as in Figure 6a.

Errors (2σ) do not exceed symbol size

224x594mm (300 x 300 DPI)

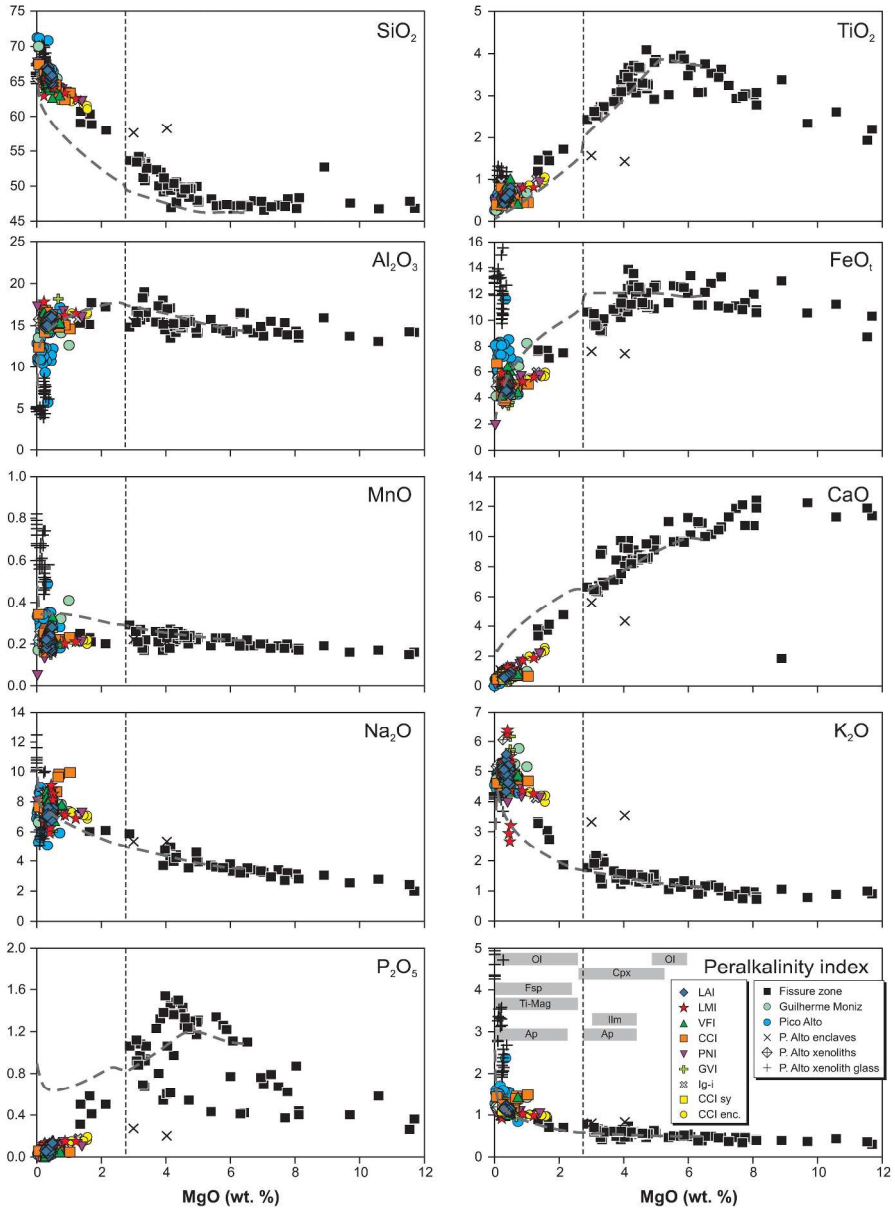

Figure 7 Major and trace element compositional data for Terceira plotted against MgO contents. The grey dashed line represents the most successful Rhyolite-MELTS model (Polybaric fractional crystallisation with a transition from 500 MPa to 150 MPa set to occur at 1,100 °C, fO2 = FMQ -1, initial water content = 1.5 wt. %). The transition from 500 to 150 MPa is marked with a vertical dashed black line at 2.76 wt. % MgO on each plot. The crystallisation intervals for each of the predicted mineral phases are marked on the lower-right plot. For clarity, data for Cinco Picos and Santa Bárbara are not shown. All data sourced from Self (1974), Mungall (1993), Gertisser et al. (2010), Madureira et al. (2011), Tomlinson et al. (2015), and Jeffery et al. (2016a). All major element oxides reported in wt. %, trace elements as ppm. Errors (2σ) do not exceed symbol size. Abbreviations used: Ol = olivine; Cpx = clinopyroxene; Fsp = feldspar; Ti-Mag = Ti-magnetite; Ilm = ilmenite; Ap = apatite

247x336mm (300 x 300 DPI)

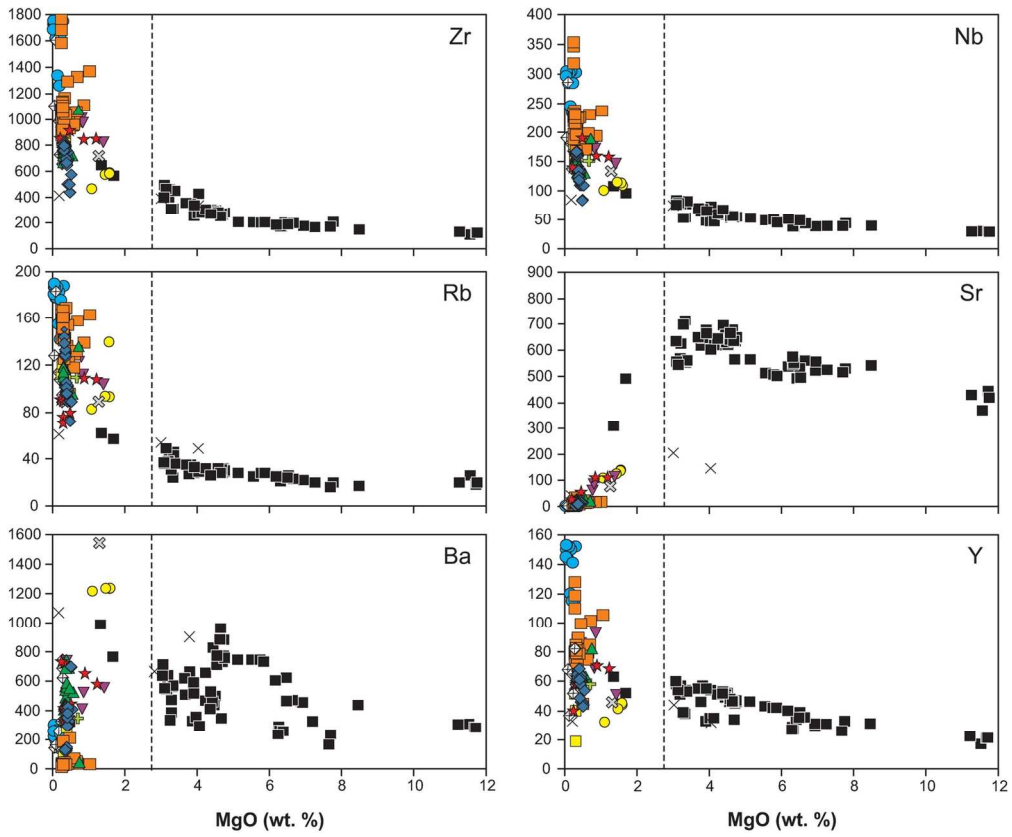

Figure 7 Major and trace element compositional data for Terceira plotted against MgO contents. The grey dashed line represents the most successful Rhyolite-MELTS model (Polybaric fractional crystallisation with a transition from 500 MPa to 150 MPa set to occur at 1,100 °C, fO2 = FMQ -1, initial water content = 1.5 wt. %). The transition from 500 to 150 MPa is marked with a vertical dashed black line at 2.76 wt. % MgO on each plot. The crystallisation intervals for each of the predicted mineral phases are marked on the lower-right plot. For clarity, data for Cinco Picos and Santa Bárbara are not shown. All data sourced from Self (1974), Mungall (1993), Gertisser et al. (2010), Madureira et al. (2011), Tomlinson et al. (2015), and Jeffery et al. (2016a). All major element oxides reported in wt. %, trace elements as ppm. Errors (2σ) do not exceed symbol size. Abbreviations used: Ol = olivine; Cpx = clinopyroxene; Fsp = feldspar; Ti-Mag = Ti-magnetite; Ilm = ilmenite; Ap = apatite

143x118mm (300 x 300 DPI)

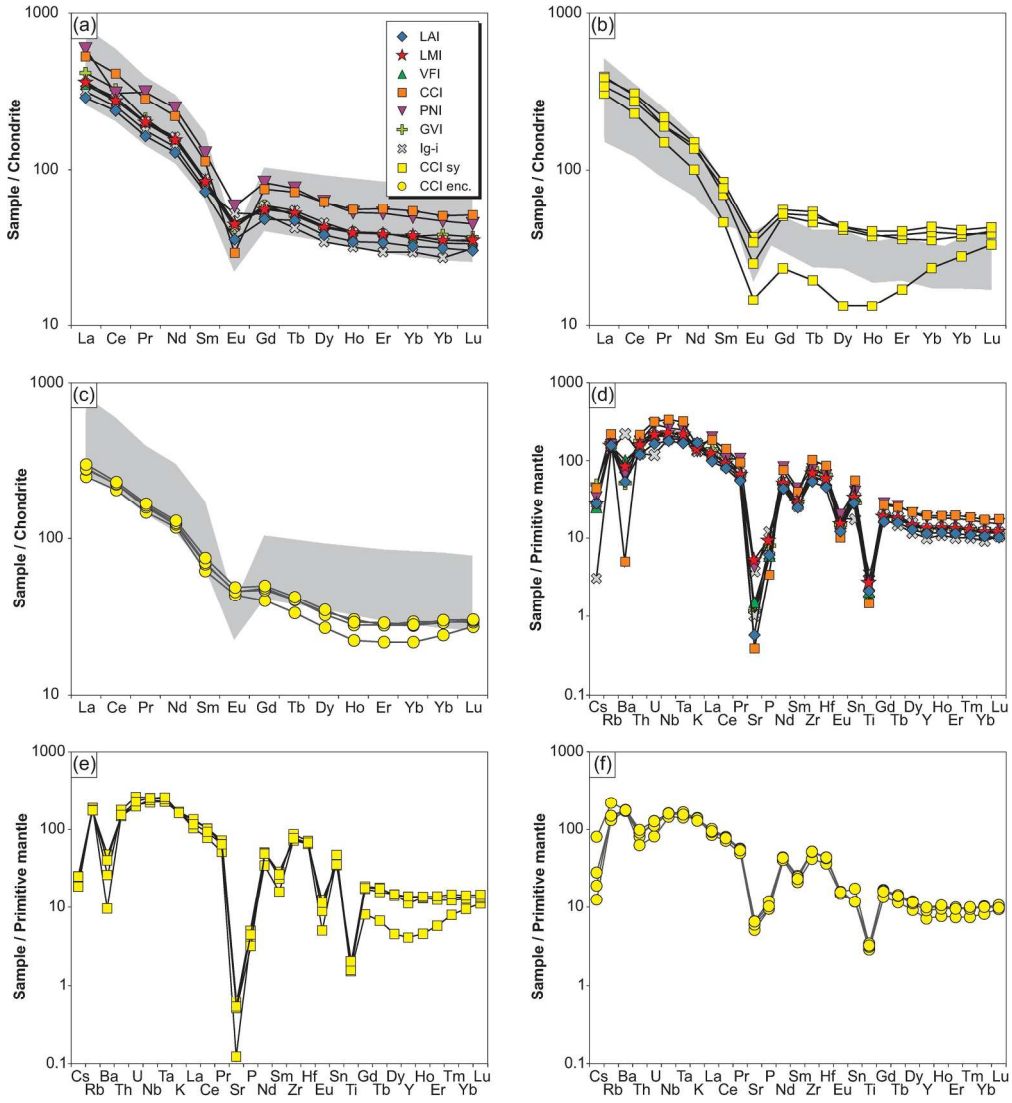

Figure 8 Trace element variation diagrams for Terceira lithologies. Chondritic and primitive mantle values taken from Sun and McDonough (1989). (a) Chondrite-normalised REE compositions of the ignimbrite formations. Grey field indicates range of literature values for the four youngest ignimbrite formations (LAI, LMI, VFI, CCI) taken from Tomlinson et al. (2015) (b) Chondrite-normalised REE compositions of the CCI syenite autoliths. Data sourced from Jeffery et al., 2016a. Grey field indicates range of literature values for syenitic xenoliths taken from Mungall (1993) (c) Chondrite-normalised REE compositions of the CCI syenite-hosted enclaves. Grey field indicates range of literature values for the four youngest ignimbrite formations (LAI, LMI, VFI, CCI) taken from Tomlinson et al. (2015) (d) Multi-element trace element variation diagram for the ignimbrite formations (e) Multi-element trace element variation diagram for the CCI syenite autoliths. Data taken from Jeffery et al., 2016a (f) Multi-element trace element variation diagram for the CCI syente-hosted enclaves

201x219mm (300 x 300 DPI)

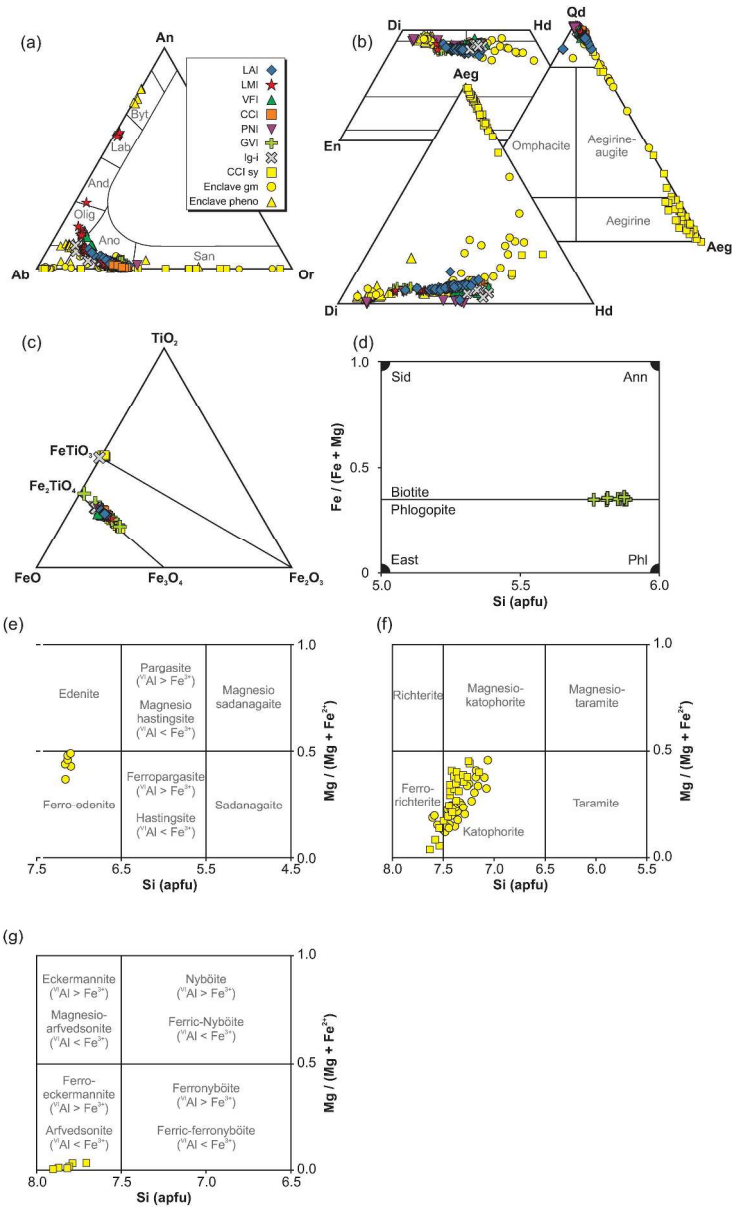

Figure 9 Mineral compositions of the ignimbrite formations, CCI syenite autoliths, and syenite-hosted enclaves. Analyses from the groundmass of the enclaves are labelled as 'Enclave gm', whilst the enclave phenocrysts are marked 'Enclave pheno' (a) Alkali feldspar compositions plotted into the ternary An-Ab-Or system (b) Clinopyroxene compositions plotted into the pyroxene quadrilateral and, where relevant, the ternary Qd-Jd-Aeg system (Morimoto et al., 1988) and the ternary Di-Hd-Aeg system (c) Fe-Ti oxide compositions plotted into the TiO2-FeO-Fe2O3 ternary system (d) Biotite compositions of the GVI (Deer et al., 1966) (e) Ca-amphibole compositions for the syenite-hosted enclaves, plotted in the scheme of Leake et al. (1997) (f) Ca-Na-amphibole compositions for the CCI syenites and syenite-hosted enclaves, plotted in the scheme of Leake et al. (1997) (g) Na-amphibole compositions for the CCI syenites, plotted in the scheme of Leake et al. (1997)

246x405mm (300 x 300 DPI)

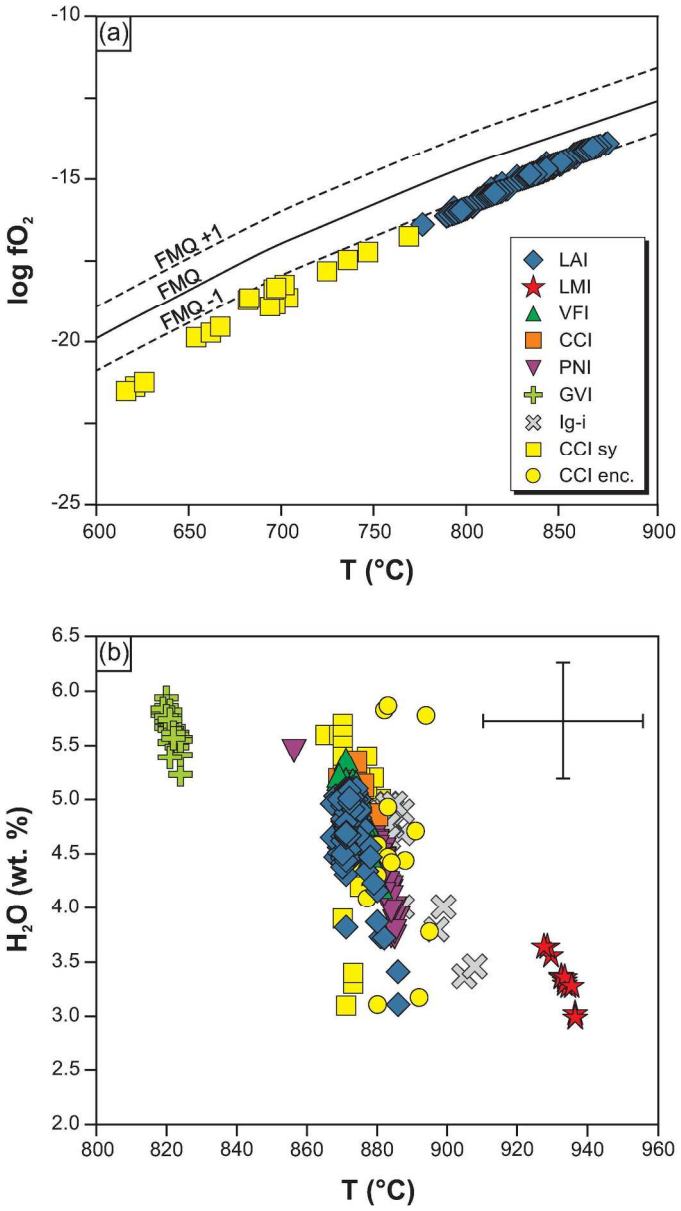

Figure 10 Summarised results of thermometry and hygrometry using the ILMAT program of Lepage (2003) for two-oxide thermometry, the alkali feldspar-melt thermometer of Putirka (2008), and the feldspar-melt hygrometer of (Mollo et al., 2015). A full discussion of each method is given in the text (a) T-fO2 estimates for the LAI and the CCI syenite autoliths derived from two-oxide models. FMQ buffer reaction curve calculated for 100 MPa (b) T-H2Omelt estimates for the ignimbrite formations, the CCI syenite autoliths, and the syenite-hosted enclaves, derived from alkali feldspar-melt thermohygrometry. The standard error of estimate for both temperature and water content is shown in the top right corner

152x272mm (300 x 300 DPI)

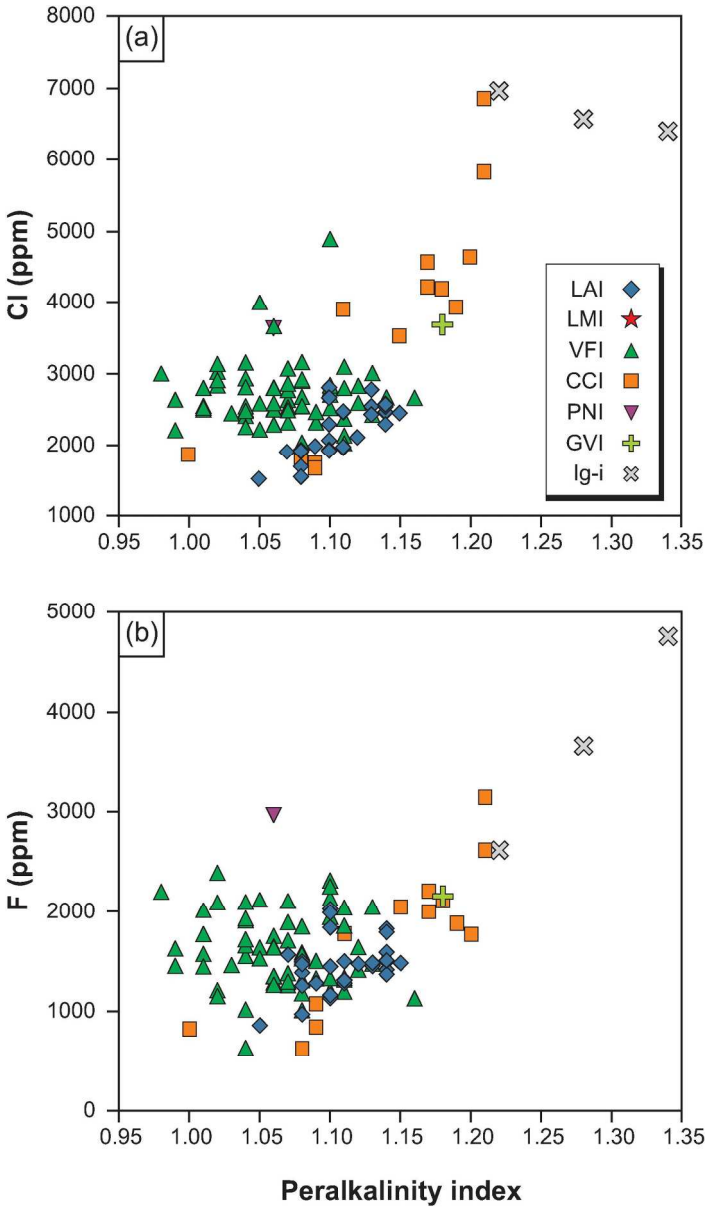

Figure 11 Halogen compositions of melt inclusions from each of the ignimbrite formations of Terceira plotted against Peralkalinity Index. Errors (2σ) do not exceed symbol size

144x248mm (300 x 300 DPI)

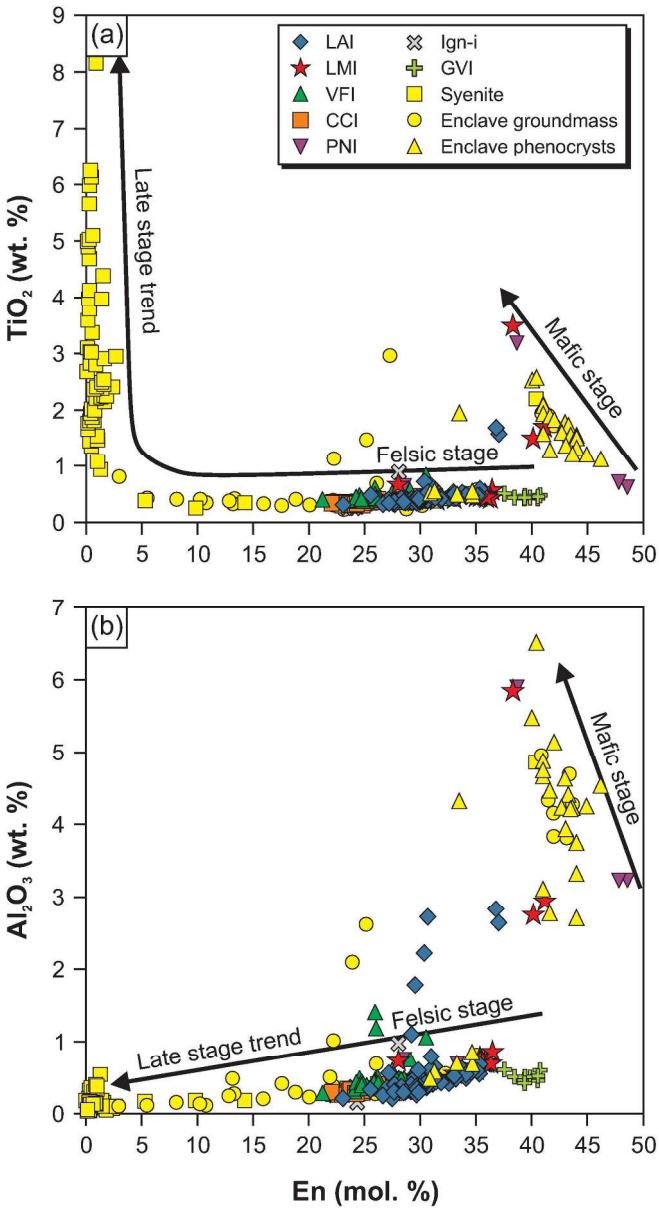

Figure 12 Variations in TiO2 and Al2O3 contents of clinopyroxene in relation to depth of crystallisation (cf. Beier et al., 2006; Jeffery et al., 2016a)

155x285mm (300 x 300 DPI)

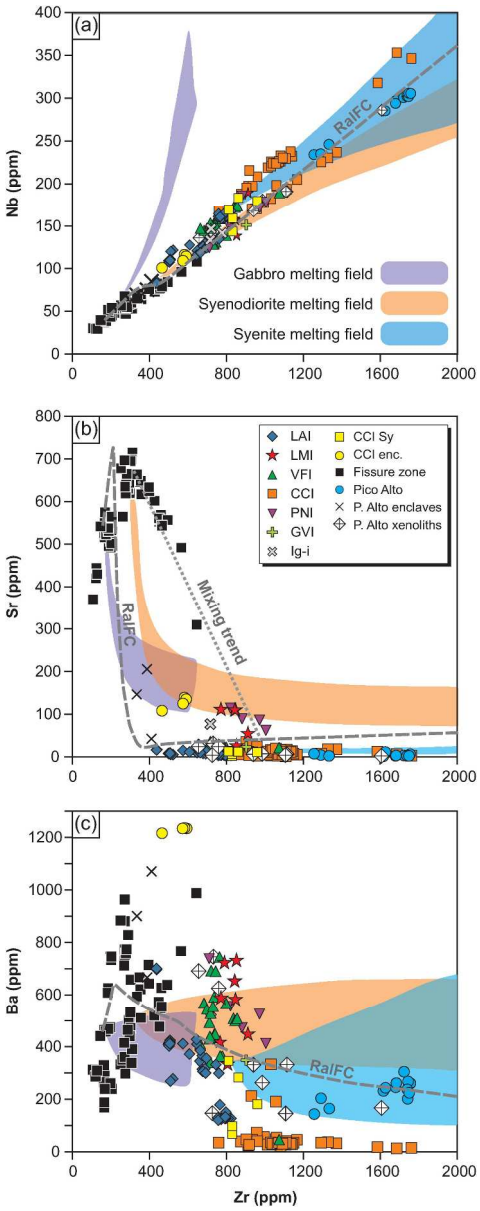

Figure 13 Results of Rayleigh fractionation and batch melting trace element modelling. The calculated Rayleigh fractionation curve is labelled RalFC. Batch melting models were calculated for hypothetical gabbroic, syenodioritic, and syenitic lithologies. Each field comprises the total area occupied by four individual batch melting curves, each curve generated by varying the original mineral proportions of the parental material. For example, the gabbro field indicates the area occupied by four separate batch melting curves, each produced by altering the relative proportions of plagioclase, clinopyroxene, and olivine.

215x548mm (300 x 300 DPI)

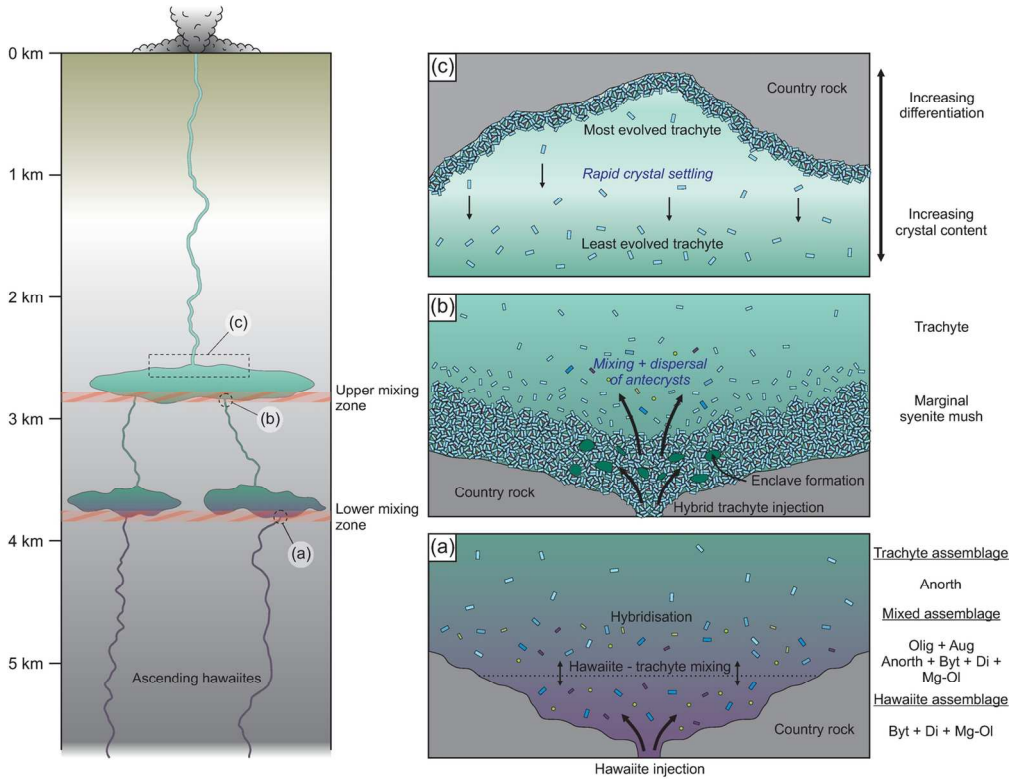

Figure 14 Conceptual model for themagma plumbing system of Pico Alto volcano, comprising a prominent magma storage zone in shallow crust. Abbreviations used: Byt = bytownite, Di = diopside, Mg-Ol = Mg-rich olivine, Anorth = anorthoclase, Olig = oligoclase, Aug = augite (a) Ascending hawaiites (phase assemblage = Byt + Di + Mg-Ol) are mixed with trachytes (phase assemblage = Anorth), forming hybridised intermediate to silicic magmas (phase assemblage = Olig + Aug + Anorth + Byt + Di + Mg-Ol) (b) Injection of hybridised trachyte into peralkaline trachyte in the uppermost portion of the shallow crustal storage zone, passing through a marginal syenitic crystal mush and forming enclaves therein. Replenishment initiates further mixing and introduces antecrysts to the eruptible portion of the reservoir (c) Efficient crystal settling in the uppermost eruptible cap of peralkaline trachyte generates crystal poor magma and chemical zoning

134x104mm (300 x 300 DPI)

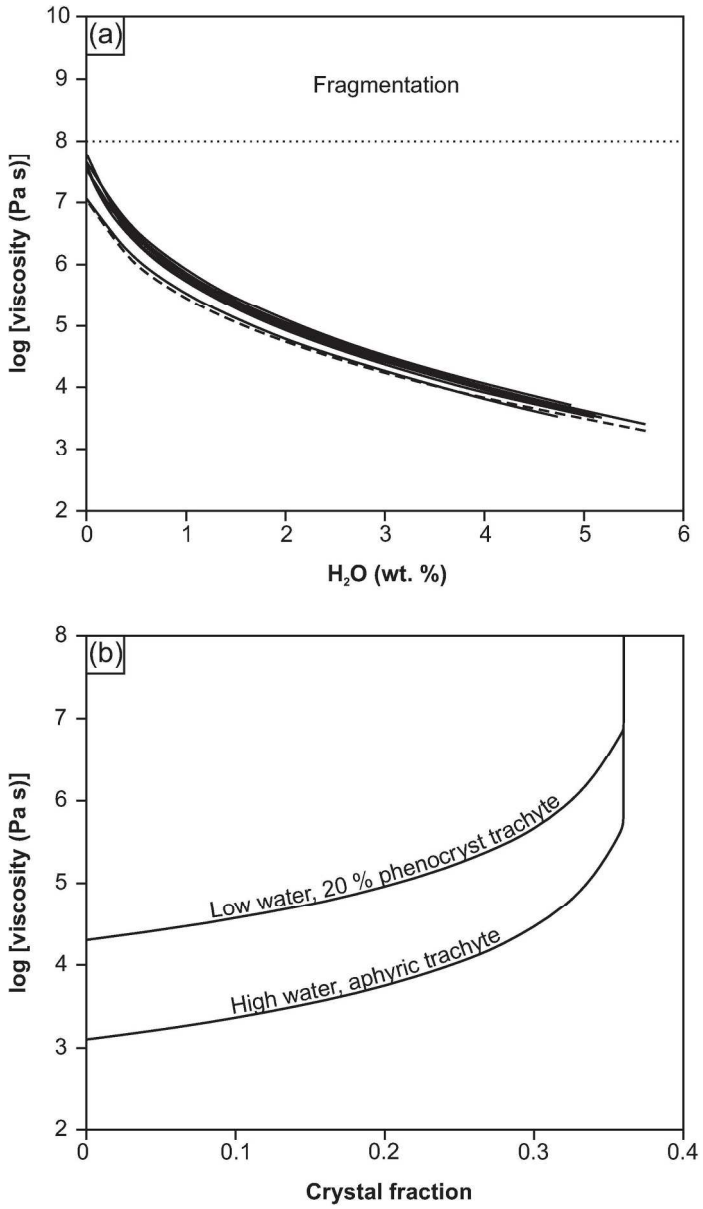

Figure 15 Results of rheological modelling aiming to simulate the effects of degassing and microlite crystallisation upon the viscosity of the peralkaline trachytic magmas of this study during ascent (a) Isothermal magma viscosities calculated for each of the ignimbrite-forming peralkaline trachytes using the model of Giordano et al. (2008) and the melt to magma viscosity conversion of Dingwell et al. (1993). Magma water contents were varied from 0 to 6 wt. %, and crystal fraction was set to 0.2 (see text for full details). Each of the curves was calculated using a composition from one of the peralkaline ignimbrite formations of this study (b) Bubble-free, crystal bearing magma viscosities for the peralkaline trachytes of this study, calculated using the model of Vona et al. (2011). Models were run for the minimum and maximum pre-eruptive melt viscosity estimates determined in this study (103.1 to 104.3 Pa s, respectively), using a variable crystal fraction (0.0 to 0.4) and a mean crystal aspect ratio of 7 (see text for details)

146x254mm (300 x 300 DPI)

Table 1: Summary table of the key petrographical and geochemical features of the different lithologies identified in this study

	Ignimbrite	**Syenitic autoliths**	**Autolith-hosted enclaves**
Texture	Porphyritic	Cumulate	Porphyritic
Bulk rock SiO_2	62.2 to 65.9 wt. %	64.4 to 65.6 wt. %	61.1 to 62.2 wt. %
Peralkalinity index	0.98 to 1.43	1.08 to 1.14	0.97 to 1.01
Mineralogy	Afs, Aug, Di, Ti-Mag, Ap ± Ol, Ilm, Bt, Pl	Afs, Agt, Aeg, Na-Amp, Na-Ca-Amp, Aen, Ti-Mag, Ilm, Qtz, Ol, Ap, Bt, Dal, Eud	Afs, Aug, Di, Agt, Ca-Amp, Na-Ca-Amp, Ti-Mag, Ol, Pl, Ap, Eud, Dal, Aen, Ttn
Feldspar compositions	Ph: Or_{1-39}, Ab_{36-81}, An_{0-62}	Or_{17-40}, Ab_{60-83}, An_{0-4}	Ph: Or_{4-63}, Ab_{36-89}, An_{0-12}
			Gm: Or_{2-35}, Ab_{65-97}, An_{0-6}
Clinopyroxene compositions	Ph: Wo_{39-46}, En_{21-41}, Fs_{16-36}	Qd_{0-96}, Aeg_{4-99}, Jd_{0-7}	Ph: Wo_{42-48}, En_{31-46}, Fs_{8-26}
			Gm: Qd_{43-97}, Aeg_{3-57}, Jd_{0-9}

Abbreviations used: Afs = alkali feldspar; Aug = augite; Di = diopside; Ti-Mag = Ti-magnetite; Ap = apatite; Ol = olivine; Ilm = ilmenite, Bt = biotite; Pl = plagioclase; Agt = aegirine-augite; Aeg = aegirine; Na-Amp = Na-amphibole; Na-Ca-Amp = Na-Ca amphibole; Aen = aenigmatite; Qtz = quartz; Dal = dalyite; Eud = eudialyte; Ca-Amp = Ca-amphibole; Ttn = titanite; Pheno = phenocrysts; Gm = groundmass; Or = orthoclase; Ab = albite; An = anorthite; Wo = wollastonite; En = enstatite; Fs = ferrosilite; Qd = quadrilateral components; Jd = jadeite; Ph = phenocrysts; Gm = groundmass

Table 2: Mineral compositions used for major element mass balance modelling

Composition	**Basalt**						**Hawaiite**					
Mineral	Pl	Ol	Cpx	Ti-mag	Ilm	Ap	Pl	Ol	Cpx	Ti-mag	Ilm	Ap
SiO_2	51.31	39.20	51.16				54.14	37.28	49.20			
TiO_2		0.04	1.09	21.50	48.80			0.06	2.40	21.50	48.80	
Al_2O_3	28.73	0.02	2.32	1.48	0.04		26.50	0.03	4.35	1.48	0.04	
Fe_2O_3												
FeO	0.70	18.94	6.07	68.53	45.37		0.73	30.02	8.40	68.53	45.37	
MnO		0.28	0.16	0.66	0.67			0.46	0.20	0.66	0.67	
MgO	0.17	41.58	16.71	1.74	1.73		0.11	33.38	13.79	1.74	1.73	
CaO	13.60	0.31	18.61	0.02	0.19	55.70	10.75	0.36	21.57	0.02	0.19	55.70
Na_2O	3.63	0.05	0.31				5.00	0.03	0.45			
K_2O	0.19						0.34					
P_2O_5						41.82						41.82
H_2O						0.59						0.59

Composition	**Mugearite**						**Benmoreite**					
Mineral	Pl	Ol	Cpx	Ti-mag	Ilm	Ap	Pl	Ol	Cpx	Ti-mag	Ilm	Ap
SiO_2	55.57	35.83	47.20				58.33	36.82	50.72			
TiO_2		0.05	2.33	16.50	35.80			0.02	1.13	16.50	35.80	
Al_2O_3	25.62	0.02	4.36	2.57	1.74		23.81	0.01	2.69	2.57	1.74	
Fe_2O_3												
FeO	0.64	35.66	9.53	73.42	51.29		0.71	32.66	8.41	73.42	51.29	
MnO		0.93	0.26	0.81	0.56			0.78	0.31	0.81	0.56	
MgO	0.08	28.41	13.27	1.77	3.00		0.07	30.56	13.96	1.77	3.00	
CaO	9.73	0.23	19.58	0.09	0.00	55.70	6.96	0.22	20.88	0.09	0.00	55.70
Na_2O	5.66	0.02	0.56				6.94	0.00	0.52			
K_2O	0.41						0.77					
P_2O_5						41.82						41.82
H_2O						0.59						0.59

Composition	**Trachytes**						**Pantellerite**					
Mineral	Afs	Ol	Cpx	Ti-mag	Ilm	Ap	Afs	Ol	Cpx	Ti-mag	Ilm	Ap
SiO_2	66.18	33.10	50.52				67.02	30.09	49.97			
TiO_2	0.06	0.04	0.39	22.56	51.10			0.04	0.51	22.56	50.40	
Al_2O_3	18.75	0.03	1.86	0.60	0.07		18.77	0.01	0.50	0.60	0.02	
Fe_2O_3												
FeO	0.49	50.39	15.94	71.77	45.00		0.34	56.85	16.81	71.77	45.78	
MnO		3.48	1.33	1.78	2.30			4.04	1.17	1.78	2.19	
MgO	0.01	14.28	10.05	1.12	1.68		0.00	7.93	9.15	1.12	0.19	
CaO	0.29	0.26	19.89			55.70	0.20	0.47	20.25		0.00	55.70
Na_2O	7.82		0.87				7.68	0.00	0.64			
K_2O	5.47		0.00				6.24					
P_2O_5						41.82						41.82
H_2O						0.59						0.59

Abbriviations used: Pl = plagioclase; Ol = olivine; Cpx = clinopyroxene; Ti-mag = Ti-magnetite; Ilm = ilmenite; Ap = apatite; Afs = alkali feldspar; LET = least evolved trachyte; MET = most evolved trachyte

Table 3: Partition coefficients selected for trace element modelling

Rayleigh fractionation - Step 1 and batch melting of gabbro

	Pl	Cpx	Ol	Ti-Mag	Ilm	Ap	Afs
Nb		0.1[2]	0.01[3]	0.9[4]	2[5]*		
Cr	0.08[1]	5.3[1]	2.8[1]	4.2[1]	4.2[1]		
Y							
Zr	0.13[1]	0.27[1]	0.06[1]	0.4[1]	0.4[1]		
Sr	2.7[1]	0.16[1]	0.02[1]	0.68[1]	0.68[1]	1.2[6]	
Ba	0.56[1]	0.04[1]	0.03[1]	0.4[1]	0.4[1]		
Rb	0.13[1]	0.04[1]	0.04[1]	0.47[1]	0.47[1]		
Ni	0.04[1]	2.5[1]	34[1]	3.5[1]	3.5[1]		

Rayleigh fractionation - Step 2 and batch melting of syenodiorite

	Pl	Cpx	Ol	Ti-Mag	Ilm	Ap	Afs
Nb	0.135[7]						
Cr							
Y							
Zr	0.04[8]	0.44[8]		0.94[8]	0.94[8]		
Sr	10.5[7]		0.01[9]	0.33[7]			
Ba	1.77[9]			0.07[10]			
Rb	0.03[8]	0.04[8]	0.02[8]	0.34[8]	0.34[8]		

Rayleigh fractionation - Step 3 and batch melting of syenite

	Pl	Cpx	Ol	Ti-Mag	Ilm	Ap	Afs
Nb			0.009[12]				0.051[13]*
Cr		6[11]	5[11]	8[11]	8[11]		
Y			0.138[12]				0.064[13]*
Zr	0.16[8]	0.5[11]	0.07[8]	0.25[11]	0.25[11]		0.056[13]*
Sr			0.053[12]			8[11]	1.76[13]*
Ba			0.023[12]			0.45[11]	5.27[13]*
Rb	0.07[8]	0.04[8]	0.08[8]	0.01[8]	0.01[8]		0.31[13]*

Abbreviations used: Pl = plagioclase; Cpx = clinopyroxene; Ol = olivine; Ti-Mag = Ti-magnetite; Ilm = ilmenite; Ap = apatite; Afs = alkali feldspar. References used: (1) Villemant *et al.* (1981); (2) Wood & Trigila (2001); (3) McKenzie & O'Nions (1991); (4) Nielsen (1992); (5) Zack & Brumm (1998); (6) Watson & Green (1981); (7) Ewart & Griffin (1994); (8) Lemarchand *et al.* (1987); (9) Villemant (1988); (10) Luhr *et al.* (1984); (11) Mahood & Stimac (1990); (12) Larsen (1979); (13) White *et al.* (2003). Average partition coefficients marked with *